This document is downloaded from DR-NTU (https://dr.ntu.edu.sg)
Nanyang Technological University, Singapore.

High power gallium nitride light-emitting diodes for efficient solid state lighting and displays

Ji, Yun

2014

Ji, Y. (2014). High power gallium nitride light-emitting diodes for efficient solid state lighting and displays. Doctoral thesis, Nanyang Technological University, Singapore.

https://hdl.handle.net/10356/61778

https://doi.org/10.32657/10356/61778

Downloaded on 13 Mar 2024 16:20:51 SGT

High Power Gallium Nitride Light-Emitting Diodes for Efficient Solid State Lighting and Displays

JI YUN

School of Electrical and Electronic Engineering

A thesis submitted to the Nanyang Technological University

In partial fulfillment of the requirement for the degree of

Doctor of Philosophy

2014

Acknowledgements

Numerous people have contributed to my research work, and made my four-year study a rewarding experience with fruitful harvest.

First and foremost, I would like to take this opportunity to express my appreciation and respect to my supervisor, Nanyang Associate Professor Hilmi Volkan Demir, for providing me this chance to pursuing the research study. His enthusiastic encouragement and patient guidance inspire my motivation and courage, and his professional knowledge and conscientious attitude lead me to realize my ideas step by step, making the graduate study a pleasurable and memorable experience to me.

I would also like to express my sincere gratitude to my co-supervisor, Professor Sun Xiao Wei, for his support and guidance throughout my study, for his continuous support and valuable suggestions and comments on my research work.

I would also like to thank all the research staffs and students from *Luminous!* research center, Dr. Tan Swee Tiam, Dr. Liu Wei, Dr. Ju Zhengang, Zhang Xue Liang, Zhang Zi Hui, Zabu Kyaw, Lu Shun Peng, Zhang Yi Ping, Zhu Bin Bin, Namig Hasanov, Dr. Evren Mutlugun, Liu Shu Wei, Leck Kheng Swee, and all others, although not named here, for their innovative inspiration, thorough discussions, insightful suggestions and comments, as well as their precious encouragement and friendship.

I would like to thank Dr. Soh Chew Beng, from Institute of Materiald Research and Engineering (IMRE), for his guidance and support in the course of my experiments.

In addition, I would also like to extend my special thanks to all the technical and administrative staffs in Division of Microelectronis: Ms Chia Hwee Keng Debbie and Ms Vino Prabakaran from *Luminous!* Center of Excellence; Mr. Mak Foo Wah, Mr. Mohamad Shamsul bin Mohamad, Mr. Soh Eng Hwa, Mr. Tan Ah Koon Clarence, and Ms. Chia Ai Lay Irene from Nanyang Nanofabrication Centre Clean Room II (N2FC-CR2), Ms. Low Poh Chee, Mr. Lim Teng Keng Desmond and Ms. Yee Yang Boey Yvonne from Photonics Laboratory. Their professional support and continuous assistance make my research work move forward smoothly.

Finally, I wish to convey my gratitude to my beloved family for their never-ending moral support and encouragement throughout my studies. Particularly, I am greatly indebted to my parents for their love and understanding.

Table of Contents

Acknowledgements ..... **I**

Table of Contents ..... **III**

Abstract……...**VI**

List of Figures ..... **X**

List of Tables ..... **XVI**

Abbreviations ..... **XVII**

Chapter 1. Introduction **1**

1.1. Background and Motivation 1

1.2. Objectives of the Thesis 9

1.3. Major Contributions of the Thesis 9

1.4. Organization of the Thesis 11

Chapter 2. Literature Review **13**

2.1. Group III-Nitride Compound Semiconductors 13

2.1.1. Basic Properties of III-Nitride Compound Semiconductors 13

2.1.2. Polarization Effects in III- Nitrides 15

2.2. LED Efficiency 17

2.3. Light Extraction Efficiency of Light-emitting Diodes 19

2.4. White Light Source for Lighting and Display Applications 23

Chapter 3. Epitaxial Growth and Device Fabrication of Gallium Nitride Light-emitting Diodes **28**

3.1. Epitaxial Growth of GaN LED Wafers 28

3.1.1. Metal-Organic Chemical Vapor Deposition (MOCVD) 28

3.1.2. Epitaxial Growth of High Quality GaN Films 31

3.1.3. Epitaxial Growth of GaN LED Wafers 33

3.2. Wafer-level Characterization 35

3.3. Fabrication of GaN LED Devices 38

3.4. Chip-level Characterization 42

3.5. Conclusion 44

Chapter 4. p-Type Doped Quantum Barriers for Enhanced Hole Transport...45

4.1. Introduction 46

4.2. Growth and Fabrication of LED Samples 46

4.3. Dual-wavelength Emission from Quantum Wells 48

4.4. Simulated Carrier Distributions 51

4.5. Comparison of Electrical and Optical Performance 53

4.6. Conclusion 54

Chapter 5. Influence of n-Type and p-Type Electron Blocking Layers.....56

5.1. Introduction 56

5.2. Epitaxial Growth and Device Fabrication 58

5.3. Comparison of Optical and Electrical Performance of LED Devices 58

5.4. Numerical Analyses of Devices with Different Electron Blocking Layer Structures 61

5.5. Conclusion 68

Chapter 6. Emission Kinetics in Polar vs. Semipolar GaN Light-Emitting Diodes……..69

6.1. Introduction 69

6.2. Growth and Fabrication of Polar/Semipolar GaN LEDs 70

6.3. Comparison of Device Performance 72

6.4. Conclusion.....80

Chapter 7. Application of GaN LEDs - Tunable White Light Emission 81

7.1. Introduction.....81

7.2. Fabrication of Tunable LEDs.....83

7.3. Tunable White Light Emission 86

7.4. Conclusion.....89

Chapter 8. Conclusions and Recommendations.....91

8.1. Conclusions.....91

8.2. Recommendations for Future Work.....93

Publication List 96

Bibliography.....101

Abstract

Nitride based light-emitting diodes (LEDs) are considered to be the next generation lighting source, owing to their superior advantages including high brightness, high energy conversion efficiency, long life span, compact size, fast response, and low maintenance cost. Tremendous work has been devoted to improving the performance of InGaN/GaN multiple quantum well LEDs in the past decades. The GaN based white LED has currently achieved reasonably high efficacy and displays a huge potential of replacing the incandescent and fluorescent lamps in the current market. However, the performance of InGaN/GaN LED light sources is still limited by some technical issues. One of the challenges is to reduce the efficiency droop, the phenomenon of reduction of external quantum efficiency at high current levels, such that the device could maintain high luminous efficacy for high brightness lighting applications. The root cause of the efficiency droop is still under debate, although there have been more convincing reports lately. Also, the lighting source should provide high chromaticity quality comparable to the conventional lighting sources to generate comfortable visual perception. Tremendous research work has been contributed to the improvement of InGaN/GaN LED lighting quality.

This thesis research work focuses on the design, growth and fabrication of InGaN/GaN LED structures for enhanced efficiency of light emission. InGaN/GaN multiple quantum wells LED wafers with high crystal quality and high uniformity were grown using metal-organic chemical vapor deposition technique. The fabrication processes of LED chips were developed, and characterization methods for both wafer-level and chip-level electrical and optical performance were employed. Based on

these standard growth and fabrication procedures, new device epi-structures have been designed for the performance improvement of InGaN/GaN LEDs.

Excess electron overflow and hole injection shortage into the quantum wells cause the non-uniform carrier distribution and carrier crowding within the MQWs. Hence, all the carriers are involved in the radiative recombination process to generate photons, suppressing the optical output power as well as the energy conversion efficiency of LED devices.

In this thesis, to enhance the hole transport depth, a partially p-type doped quantum barriers structure has been proposed. In order to investigate the carrier transport behavior within the active region, the quantum wells are intentionally grown at different temperatures, to incorporate different indium content. Through examining the emission intensity at different wavelengths, it is found that, in conventional LED structures, the holes could only be injected into shallow quantum wells close to the p-GaN layer. By inserting p-type doped GaN layer into the quantum barriers close to the p-GaN, the potential energy barriers for holes are reduced. Hence, the holes are able to reach deeper quantum wells close to the n-GaN side, as indicated by the increased light emission from deeper quantum wells. As a benefit, the hole distribution is more uniform within the MQWs, and more QWs are involved in the light emission.

The conventional LED employs a p-type doped AlGaN layer as the electron blocking layer (EBL) to confine electrons within the MQWs region and prevent them from overflowing into the p-GaN layer. However, the p-EBL, inserted between the MQWs and the p-GaN layer, also suppresses the hole injection from the p-GaN to the MQWs, since the large band gap AlGaN layer creates an energy barrier for both electrons and holes. In contrast, when an n-type AlGaN EBL is adopted instead, the EBL blocks excess electrons before they enter the MQWs region. Hence, the electron

crowding is avoided. Also, since the n-EBL is not on the path of hole transport into the active region, the amount of holes injected into the QWs is not suppressed. Simulation results suggest that the n-EBL structure results in more uniform electron and hole distributions, a higher hole concentration, and a higher radiative recombination rate in each individual QW, which agrees with the experimentally measured electroluminescence emission intensity and optical power output.

The study on the influence of polarization fields on the device efficiency has also been carried out. So far, most research on the improvement of GaN LED performance focus on the structures grown on (0001) *c*-plane sapphire substrates. Due to the strong polarization field caused by the spontaneous and piezoelectric polarizations, the electron and hole wave functions are spatially separated, hence reducing the radiative recombination rates within the QWs. LED structures grown on nonpolar and semipolar planes have been proposed to eliminate this problem. However, it is still unclear how the polarities of different growth planes affect the carrier recombination dynamics and device performance. In this thesis work, the MQW LED structures grown on (0001) polar and (11-22) semipolar planes are investigated for the comparative investigation of carrier dynamics, in collaboration with the University of California, Santa Barbara (UCSB). The underlying physics behind the performance difference is revealed through photoluminescence and electroabsorption measurements and energy band analysis.

Finally, a GaN based white light emitting source with tunable optical parameters is demonstrated for the extended application of GaN LED as lighting and display sources. The blue light emitting GaN LED chip has been designed to yield a current-dependent dual-wavelength emission centered at 425 and 460 nm. Nano-sized phosphor particles with photoluminescence emission peaks at 560 and 625 nm are

coated on the LED chip to convert the blue light into green and red color light. As the operating current of the device varies, the blue emission intensity of the two peaks from the GaN LED chip changes, leading to intensity change of the green and red light. Hence, the color temperature and color rendering index could be adjusted accordingly. The proposed device structure provides a new method for generating high quality tunable white light source for indoor lighting and display applications.

In summary, this dissertation includes the epitaxial growth, device fabrication, and theoretical studies of InGaN/GaN LEDs. Novel epitaxial structures have been proposed and realized in LED devices for performance enhancement, and the physics behind the performance improvement has been revealed for each proposed structure. The thesis work has provided insights important for design, growth and fabrication of high performance GaN LED based solid state lighting and display sources.

List of Figures

Figure 1.1 Energy consumption by lighting applications for residential and commercial sectors in U.S. for Year 2011. 2

Figure 1.2 Historical development of the efficiency of white light sources. 4

Figure 1.3 Different LED packages and LED lamp products for traffic lights, television, mobile device, automotive, and indoor and outdoor lighting applications. . 6

Figure 1.4 The YAS Hotel in Abu Dhabi with LED decoration lighting, capable of running color-changing light sequences and displaying low-resolution three-dimensional videos 6

Figure 1.5 London Bridge with LED lighting. Power consumption is reduced by 40 percent compared to the past lighting methods 7

Figure 1.6 Forecasted U.S. lighting energy consumption and savings, Year 2010 to 2030 8

Figure 2.1 Bandgap energy (and corresponding emission wavelength) versus lattice constant of III-V nitride compound semiconductors at room temperature 15

Figure 2.2 Surface charge and direction of electric field and polarization field for spontanesous and piezoelectric polarization in III-Nitrides for N and Ga face growth orientation 16

Figure 2.3 Schematic diagram for InGaN/GaN quantum well structure (a) without and (b) with polarization field. 17

Figure 2.4 Light trapping at the GaN/air interface by total internal reflection (TIR), due to the refractive index difference between GaN and air medium. 19

Figure 2.5 (a) Cross-sectional SEM image of graded-refractive-index (GRIN) anti-reflective (AR) coating ITO layers; and (b) comparison of calculated reflectivity of GaN surface with no coating, conventional ITO coating and the GRIN coating. 21
Figure 2.6 Schematic process flow for the fabrication of ITO photonic crystal: (a) the starting LED wafer; (b) silica spheres spin-coated onto the ITO layer; (c) ICP etching of ITO and sphere removal; (d) mesa definition via photolithography; (e) n-GaN exposure through dry etching; and (f) metal pad deposition. 22
Figure 2.7 Scanning electron microscopy images of n-face GaN etch morphology: after etching (a) 2 min and (b) 10 min in 2.2 M KOH solution; and after 10 min etch in (c) 1.25 M and (d) 8.8 M KOH solution. 23
Figure 2.8 Spectra of white light emitted from different lighting sources: natural daylight, incandescent lamp, fluorescent lamp, halogen lamp, and cool and warm white LEDs. 24
Figure 2.9 (a) Tissue box under illumination of light sources with different CRI; and (b) White light sources with CCT of 2700, 3500 and 5000 K. 25
Figure 2.10 White LED configurations: blue LED chip with yellow phosphors, ultraviolet LED chip with blue and yellow (and red) phosphors; and multi-chip device consists of blue, green and red LED chips. 26
Figure 3.1 Schematic diagram of a MOCVD system: gas delivery path and reactor. .29
Figure 3.2 MOCVD reactor: (a) showerhead for gas precursor delivery; (b) rotating susceptor holding wafer substrates during growth; (c) tungsten heater underneath the susceptor; and (d) schematic diagram showing circular heater zones. 30
Figure 3.3 Schematic diagram of MOCVD reaction mechanism. 31
Figure 3.4 Epitaxial growth process of GaN crystal film on a sapphire substrate: (a) bare sapphire substrate; (b) deposition of amorphous GaN film with thickness ≈ 25

nm at low temperature; (c) high temperature annealing to form crystalized GaN seeds; (d) - (e) formation of crystalized GaN islands; and (f)-(g) formation of bulk GaN film. 32

Figure 3.5 An exemplary structure diagram of a typical InGaN/GaN MQW LED wafer. 33

Figure 3.6 *In-situ* reflectance monitoring through interference between the reflected light beams. 34

Figure 3.7 *In-situ* temperature and reflectance monitoring of GaN LED growth stages: (a) temperature ramp-up; (b) high temperature bake; (c) nucleation; (d) u-GaN; (e) n-GaN; (f) quantum wells; (g) p-GaN; (h) *in-situ* p-GaN activation annealing; and (i) temperature ramp-down. 35

Figure 3.8 (a) A transparent GaN LED epitaxial wafer grown at *LUMINOUS!*; and (b) electroluminescence spectrum of our blue LED wafer as-grown (inset: LED epi-wafer lit under current injection). 36

Figure 3.9 HRXRD ω-2θ scan curve of our InGaN/GaN LED epi-wafer. 37

Figure 3.10 (a) Thickness mapping and (b) peak emission wavelength mapping of GaN LED epi-wafer of ours. 38

Figure 3.11 Fabrication process of LED device from (a) epitaxial LED wafer with the following process flow of (b) mesa etching; (c) deposition of transparent current spreading layer; and (d) deposition of metal contact pad. 39

Figure 3.12 Fabricated LED devices under current driving: (a) without a current spreading layer; and (b) with an annealed Ni/Au current spreading layer (device mesa area = 350 × 350 μm^2). 40

Figure 3.13 High power LED chips with a device area of 1 mm × 1mm: (a) chip-on-wafer without driving current (inset: optical microscopy image of a single LED die);

and (b) fabricated chip lit-up with driving current (inset: a lit-up chip in microscope view). 42

Figure 3.14 Measured I-V characteristics of a fabricated LED chip-on-wafer (Inset-up: LED chip driven at 20 mA; inset-down: optical microscopy image of the fabricated LED devices). 43

Figure 3.15 Current-dependent optical output power and external quantum efficiency (EQE) of a fabricated LED chip-on-wafer (device area = 350 μm × 350 μm).....43

Figure 4.1 Structure diagram of LED samples: (a) Sample I with undoped QBs; and (b) Sample II with three QBs close to p-GaN doped with Mg. 47

Figure 4.2 Photoluminescence (PL) spectra of LED samples emitting at two wavelength peaks: (a) Sample I with undoped QBs and (b) Sample II with three QBs doped with Mg. 49

Figure 4.3 Electroluminescence (EL) spectra of LED samples emitting at two wavelength peaks: (a) Sample I with undoped QBs (Inset: Intensity ratio of Peak II/Peak I with increasing current injection) and (b) Sample II with three QBs doped with Mg (Inset: Intensity ratio of Peak II/Peak I with increasing current injection and zoomed-in view of the emission peak at 422 nm). 50

Figure 4.4 (a) Simulated electron and hole distributions within the MQW active region and (b) simulated energy band diagram of LED Sample I and II within the MQW active region.....52

Figure 4.5 Experimentally measured (a) I-V characteristics and (b) external quantum efficiency (EQE) and number of emitted photons for LED Sample I and II. 54

Figure 5.1 Schematic diagram and electroluminescence (EL) spectra of GaN LED devices with (a) no AlGaN EBL; (b) p-AlGaN EBL; (c) n-AlGaN EBL; and (d) both n-AlGaN and p-AlGaN EBLs. 59

Figure 5.2 Optical power and external quantum efficiency (EQE) measured for LED samples with different electron blocking layer structures. 60

Figure 5.3 Experimentally measured I-V characteristics for LED devices with different EBL structures.....61

Figure 5.4 Simulated (a) electron concentration; (b) hole concentration; and (c) electron overflow into p-GaN region for the LED devices with different EBL structures under 120 A/cm^2 current injection. 63

Figure 5.5 Simulated energy band diagram for the LED devices with (a) p-AlGaN EBL; (b) n-AlGaN EBL; and (c) both n-AlGaN and p-AlGaN EBLs under 120 A/cm^2 current injection. 65

Figure 5.6 Simulated radiative recombination rate within MQWs active region for the LED devices with different EBL structures.....66

Figure 6.1 Current dependence of electroluminescence emission peak wavelength and full width half maximum (FWHM) for the polar and semipolar GaN LED devices...72

Figure 6.2 Filed-dependent photoluminescence spectra of (a) polar LED device and (b) semipolar LED device under external bias from -2 to +2 V.....73

Figure 6.3 Time-resolved photoluminescence (TRPL) spectra of (a) polar LED device and (b) semipolar LED device under external bias from -2 to +2 V. Inset shows the carrier lifetime (extracted using exponential fitting) for (a) polar LED device under external bias from -50 to +2 V and (b) semipolar LED device under external bias from -20 to +2 V. 75

Figure 6.4 Electroabsorption spectra of (a) the polar LED device and (b) the semipolar LED device under external voltage bias from -2.0 to +2.0 V. Inset: the absorption coefficient change compared to the zero bias condition. 77

Figure 6.5 Schematic energy band diagrams for polar and semipolar GaN LEDs with negative (V<0), zero and positive (V>0) external voltage bias. 79
Figure 7.1 Electroluminescence spectra of GaN LED chip emitting at 425 and 462 nm under current level from 70 to 120 mA. Inset shows the epitaxial structure of the dual-wavelength emitting InGaN/GaN LED chip.....85
Figure 7.2 Photoluminescence spectra and absorption spectra of (a) green and (b) red quantum dots films. Inset shows the corresponding quantum yields in solid film. 86
Figure 7.3 Electroluminescence spectra of dual-wavelength emitting GaN LED chip coated with green/red quantum dots film, under operating current from 70 to 120 mA. 87
Figure 7.4 (a) Current-dependent CRI and CCT and (b) chromaticity coordinate of the GaN/QD white LED. 88
Figure 8.1 Current flow path of (a) a conventional GaN LED on sapphire; (b) a GaN vertical LED on a metal substrate; and (c) comparison of thermal conductivity of different GaN LED substrates.....95

List of Tables

Table 1.1 Performance comparison of different lighting sources. 4

Table 2.1 Selected physical parameters of wurtzite lattice AlN, GaN and InN. 14

Table 3.1 Deposition and annealing conditions of Ni/Au current spreading layers. ... 41

Abbreviations

CCT	Correlated Color Temperature
Cp_2Mg	Bis(cyclopentadienyl)magnesium, $Mg(C_5H_5)_2$
CRI	Color Rendering Index
EBL	Electron Blocking Layer
EL	Electroluminescence
EQE	External Quantum Efficiency
FWHM	Full Width Half Maximum
LED	Light-Emitting Diode
LEE	Light Extraction Efficiency
MOCVD	Metal-Organic Chemical Vapor Deposition
MQW	Multiple Quantum Well
PL	Photoluminescence
QB	Quantum Barrier
QCSE	Quantum-confined Stark Effect
QW	Quantum Well
RIE	Reactive Ion Etching
TEGa	Triethylgallium, $Ga(CH_2CH_3)_3$
TMAl	Trimethylalumium, $Al(CH_3)_3$
TMGa	Trimethylgallium, $Ga(CH_3)_3$
TMIn	Trimethylindium, $In(CH_3)_3$
TRPL	Time-resolved Photoluminescence

Chapter 1. Introduction

1.1. Background and Motivation

The energy and environment crises have been among the most concerned global issues for the past decade. Terawatt-hours of energy being consumed daily for human life and industrial manufacturing require the usage of huge amount of nature resources, including petroleum, coal, nature gas and plant fuel. The supply of these energy sources is limited, since these nature sources are non-renewable. Also, the consumption of such combustible energy sources leads to the emission of million-tons of greenhouse gases, including carbon dioxide, sulfur dioxide, nitrous oxide and methane, which are believed to contribute to the global climate change and air pollution problems.

As part of the solution to the energy and environment issues, the scientific community and industry are exploring the possibilities of clean and renewable energy sources, including solar power, wind power, geothermal power, hydropower, and nuclear power. These energy sources exhibit remarkable merits thanks to their low pollution byproducts. However, the energy conversion efficiency, the cost or the safety issue generate barriers for these energy sources to completely replace the traditional combustion based energy supplies.

One approach to solve this situation is to reduce the energy consumption by maximizing the energy utilization efficiency, so that the wasted energy will be minimized. In this regard, lighting applications becomes critical, as they take up a huge amount of the overall energy consumption. Accordingly to the data from the U.S.

Energy Information Administration, lighting applications consumed about 461 billion kilowatt-hours (kWh) of electricity in Year 2011, which equals to about 17% of the total electricity consumption. Residential lighting consumption was about 186 billion kWh or 13% of all residential electricity consumption. While lighting in commercial sector consumed 275 billion kWh of electricity, or 21% of the total commercial power usage [1].

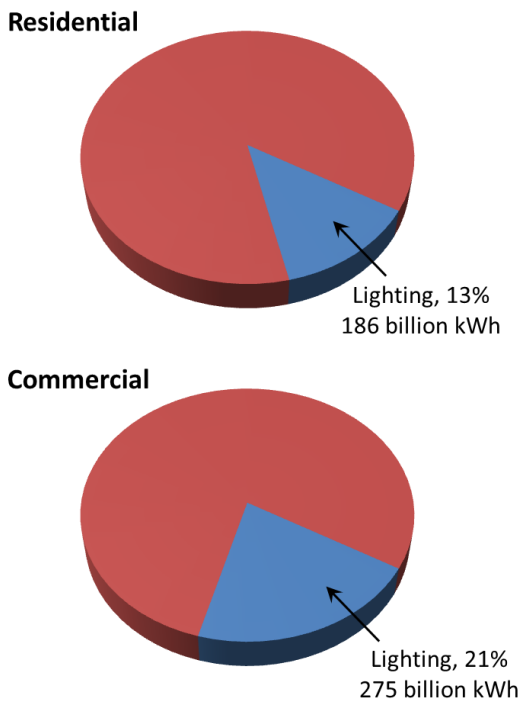

Figure 1.1 Energy consumption by lighting applications for residential and commercial sectors in U.S. for Year 2011 [1].

Hence, upgrading lighting infrastructure is one of the most cost-effective measures in energy-saving. Today, currently deployed lighting systems are mostly dominated by fluorescent lamps, generating white light through gas discharge and then down-converting the ultra-violet light to visible light using phosphor materials, and to a smaller extent, incandescent bulbs which emit visible light through thermal

irradiation. The efficiency of these lighting sources is low, since most of the power is consumed for the generation of non-visible light or heat. Hence a better artificial lighting source with higher energy utilization efficiency is needed.

Meanwhile, research and development for solid state lighting has achieved remarkable progress in the past decades. Since the electroluminescence from GaN was first announced by Pankove *et al*. in 1971, the good quality p-type GaN has been the technical limitation for the realization of p-n junctions [2-4]. Amano *et al.* demonstrated the first p-type GaN using low-energy electron beam irradiation on Mg doped GaN [5]. In 1994, Nakamura *et al.* demonstrated a more conveniently implemented method for Mg dopant activation in GaN through high-temperature post-growth annealing [6]. The first GaN based p-n homojunction LED grown on sapphire substrate, reported by Akasaki *et al*., emitted ultraviolet and blue light with an efficiency of approximately 1% [7, 8]. These works led to breakthroughs for the development of efficient p-n junction LEDs and laser diodes. In the past two decades, the efficiency of GaN-based white LEDs has been increased drastically. In May 2011, LED manufacturer Cree Inc. reported a R&D record for LED power efficacy of 231 lm/W [9], and in February 2013, the record has been updated to 276 lm/W in its R&D laboratory [10], much higher than that of the fluorescent and incandescent lamps.

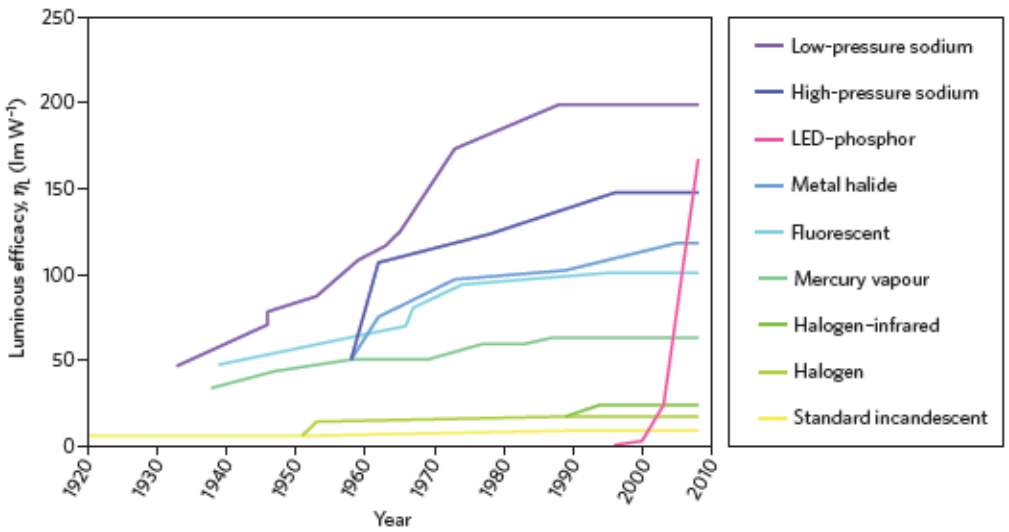

Figure 1.2 Historical development of the efficiency of white light sources [11-13].

Table 1.1 Performance comparison of different lighting sources [14].

	Efficacy	Lifetime	Correlated Color Temperature	Color Rendering Index
	Lumen/watt	Hours	Kelvin	-
Incandescent lamps	12 - 18	750 - 1,500	2400 - 2900	100
Halogen lamps	16 - 19	2,000 - 4,000	2850 - 3200	100
Compact fluorescent lamps	60 - 70	6,000 - 10,000	2700 - 6500	80 - 90
Fluorescent tubes	80 - 100	20,000	2700 - 6500	70 - 90
White LEDs	120 - 150	50,000 - 100,000	2700 - 6500	65 - 90

Compared to conventional incandescent and fluorescent lighting sources, the LED based lighting possesses several advantages:

- *High luminous efficacy*: The semiconductor device converts electrical energy to optical energy through direct recombination of carriers. Energy is released from energetic electrons in the form of photons, instead of thermal radiation. Hence, the energy conversion efficiency is much higher.

- *High reliability*: The materials used to make the lighting devices are robust and resistant to shock, vibration, external impacts, humidity and temperature change. Therefore, they can be used in different rough environment, including underwater, vacuum, cold and hot workplaces.
- *Long life span*: The semiconductor diodes can continuously operate for 50,000 to 100,000 hours, at least twice of that of the fluorescent lamps. Therefore, the maintenance and replacement costs for the LED lamp fixtures are lower.
- *Fast response*: These devices possess relative fast ON/OFF switching capability compared to the traditional lighting sources, meaning that they are more suitable for signal transmission and display applications. In contrast, traditional lighting may take several seconds to reach full brightness, and frequent on/off switching drastically reduce operational life expectancy.
- *Compact size*: The typical chip size of LED packages is in millimeter range, providing designers with flexibility to design lamp fixtures for both small and large scale applications.
- *Low voltage operation*: A low-voltage power supply is sufficient for LED illumination. This makes LED based luminaries portable with battery circuits. Also, they are compatible with solar-energy source, leading to a big advantage when used in outdoor or remote areas.

Owing to these superior merits, LEDs have been packaged into various products for a wide range of applications, including indoor and outdoor lighting, display backlighting, portable lighting, automotive lighting, and signal display boards as well as decorative lighting for architectures.

Figure 1.3 Different LED packages and LED lamp products for traffic lights, television, mobile device, automotive, and indoor and outdoor lighting applications [15, 16].

Figure 1.4 The YAS Hotel in Abu Dhabi with LED decoration lighting, capable of running color-changing light sequences and displaying low-resolution three-dimensional videos [17].

Figure 1.5 London Bridge with LED lighting. Power consumption is reduced by 40 percent compared to the past lighting methods [18].

With tremendous research work devoted to the development of high efficiency and high brightness white LEDs, the solid state lighting technology presents a promising potential to replace the conventional lighting infrastructure based on incandescent lamps and fluorescent tubes. It is predicted that the solid state lighting will bring about 19% of energy saving in 2020 and 46% saving in 2030 [19]. This corresponds to a substantial annual carbon emission reduction worth many hundreds of millions of tons per year.

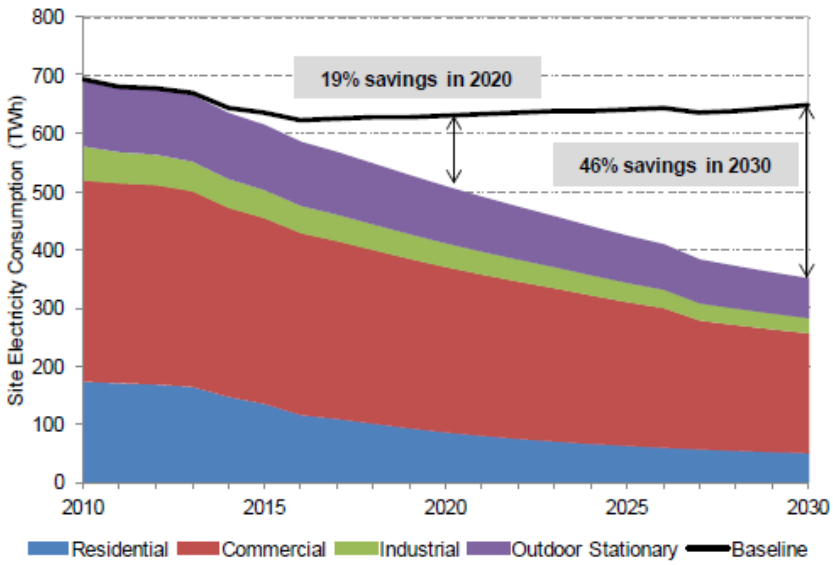

Figure 1.6 Forecasted U.S. lighting energy consumption and savings, Year 2010 to 2030 [19].

However, there are still technical issues that limit the performance of LED devices. To generate high luminous flux, the LED devices need to have large chip size to handle large driving current. The phenomenon of efficiency droop at high current level limits the performance for high power application. The root cause of the droop is being heavily investigated and various models have been applied to explain the efficiency degradation [20]. Commonly adopted white LEDs utilize blue light-emitting InGaN/GaN LED chips combined with yellow (or green and red) phosphor color convertors. The optical quality of the emitted white light still needs further optimization for general lighting purposes. The technical barriers have to be overcome before the solid state lighting sources could really merge into the consumer market and replace conventional lighting infrastructure at large scale.

1.2. Objectives of the Thesis

The scope of this thesis work includes design and growth of GaN based light-emitting diode structures, fabrication and characterization of LED devices, theoretical study of LED related physical models, and optimization and extension of LED chip applications. The objectives of this study are summarized as follows:

- To understand the structure and working principle of InGaN/GaN multiple quantum wells LEDs;
- To achieve high epitaxial crystal quality and uniformity for the epitaxial LED wafer;
- To fabricate LED devices with low forward voltage, uniform current spreading and high light extraction efficiency;
- To study the physics involved in the carrier transport, electron-hole recombination and photon generation process;
- To enhance the electrical and optical performance of LED devices through structure designs; and
- To optimize and extend the application of GaN-based white light emitting diodes.

1.3. Major Contributions of the Thesis

Throughout this thesis, the epitaxial LED wafers have been grown using the metal-organic chemical vapor (MOCVD) system. The growth conditions have been well optimized for precise control of growth rate, doping concentration, and interface formation. Blue light emitting epitaxial wafers with high crystal quality and uniform thickness and emission wavelength distribution across 2-inch wafers have been

successfully grown. Thereafter, LED wafers have been fabricated into chips using standard micro-fabrication process. The contact resistance between the metal electrode and GaN layer has been minimized to reduce the contact potential voltage. Also, a metal-based transparent current spreading layer has been developed to serve as both Ohmic contact to the GaN and current spreading layer. Standard LED characterizations have been carried out at both wafer-level and chip-level to evaluate the electrical and optical performance of the epitaxial wafers as well as the fabricated chips.

Based on the standard epitaxial growth, chip fabrication and characterization procedures, novel structures have been proposed to address the hole transporting difficulty and excess electron overflow issue. By inserting p-type doped GaN into the undoped GaN quantum barrier (QB) layers close to the p-GaN region, the potential energy barriers for holes are reduced, allowing holes to penetrate deeper into the MQWs. The device with the p-doped QB benefits from more uniform radiative recombination and less electron crowding within the MQWs. As a result, both enhanced electrical and optical performances have been observed. A dual-wavelength emission method has also been proposed as an effective way of monitoring the hole transport behavior within the multiple quantum wells region.

The commonly adopted solution for preventing excess electron overflow is to apply a p-type doped AlGaN electron blocking layer (EBL) between the MQW active region and the p-GaN region, such that the electrons will be confined within the MQWs instead of escaping into the p-GaN. However, the large band gap AlGaN also creates energy barrier for the hole transport into the MQWs active layer. An n-AlGaN EBL structure, located between the n-GaN and the MQW region, has been proposed to replace the p-EBL. Based on the experimental and numerical results, it has been

found that the n-EBL blocks excess electrons before they enter the MQWs. Therefore, the electron crowding in the QWs is avoided. Meanwhile, there is no blocking effect on the hole transport, since the large band gap AlGaN layer is not on the travelling path of holes.

The carrier dynamics within the MQWs for LED structures grown on the (0001) polar plane and the (11-22) semipolar plane have been comparatively investigated in collaboration with Professor Steven P. DenBaars from the University of California, Santa Barbara (UCSB). It has been found that the semipolar LED exhibits more stable electroluminescence and photoluminescence emission performance. Also, the semipolar LED shows a much faster carrier decay time, indicating that the radiative recombination rate within the quantum wells is higher than that of the polar LED. This study reveals the influence of the internal polarization induced field on the performance and efficiency of the LED devices.

Finally, a GaN-based white light source with tunable light quality has been designed and realized using semiconductor nanocrystal quantum dot materials. The white light source utilizes the tunability of dual-wavelength blue light emission of the GaN LED chip, together with the red/green quantum dot films, to generate high quality white light emission with current-dependent color operating point. The design provides a significant insight for the designing of white light sources with high color quality.

1.4. Organization of the Thesis

The dissertation starts with the description of the motivation, objective and major contribution of this research work in Chapter 1. The second chapter presents a detailed literature review on the historical development of GaN LEDs, physical

principles involved in the operation of GaN LEDs, and the factors limiting the LED performance. Chapter 3 describes the epitaxial growth GaN LED wafers and device fabrication process of LED chips. The characterization results at wafer-level and chip-level for a typical LED device are also shown. Chapter 4 explains the idea of enhancing hole transport into the multiple quantum well active region by using a p-type doped QB structure. Here a dual-wavelength emission from the MQW region is adopted to monitor the carrier injection depth change within the device. After that, a comparison study on the influence of n-type versus p-type electron blocking layer on the device performance is discussed in Chapter 5. Chapter 6 presents the comparative study on carrier dynamics of multiple quantum well LED grown on (0001) polar plane and (11-22) semipolar plane. Chapter 7 demonstrates a novel tunable lighting application of GaN based LEDs. Here through combining the dual-wavelength emitting InGaN/GaN LED chip and phosphor nanocrystals, a tunable white light source is introduced. Finally, Chapter 8 summarizes the work completed in this thesis and concludes with recommendations for future studies.

Chapter 2. Literature Review

In this chapter, the properties of group III-nitride compound semiconductors and concepts related to the InGaN/GaN LEDs are explained. Factors that limit the external quantum efficiency and light extraction efficiency are analyzed based on literature reports. The parameters to evaluate the quality of a white light source are introduced as well.

2.1. Group III-Nitride Compound Semiconductors

2.1.1. Basic Properties of III-Nitride Compound Semiconductors

The commonly used Group III-Nitride compound semiconductors include aluminum nitride (AlN), gallium nitride (GaN), indium nitride (InN) and their ternary and quaternary alloys. The basic physical properties of wurtzite crystal structured AlN, GaN and InN are summarized in Table 2.1. These materials commonly exhibit strong hardness, low sensitivity to ionizing radiation, high resistance to corrosion, and good electrical and optical performance. They have been widely used in high-power, high-frequency devices. Because of their large and direct energy band gaps, they are also widely used in the fabrication of optoelectronic devices including light-emitting diodes and laser diodes.

Table 2.1 Selected physical parameters of wurtzite lattice AlN, GaN and InN [21-29].

	AlN	GaN	InN
Lattice constant	a = 3.112 Å c = 4.982 Å	a = 3.189 Å c = 5.185 Å	a = 3.545 Å c = 5.703 Å
Energy bandgap	6.23 eV	3.44 eV	0.78 eV
Melting point	2200 ℃	> 2500 ℃	1100 ℃
Refractive index	1.9 - 2.2	2.43	2.9
Dielectric constant	8.5	8.9 - 9.5	15 - 15.3
Breakdown field	$(1.2\text{-}1.8)\times10^6$ V/cm	$\sim 5\times10^6$ V/cm	-
Mobility			
Electrons	135 $cm^2/(V\ s)$	~1000 $cm^2/(V\ s)$	1000 - 1900 $cm^2/(V\ s)$
Holes	14 $cm^2/(V\ s)$	< 200 $cm^2/(V\ s)$	-
Thermal conductivity	2.85 W/(cm·K)	2.3 W/(cm·K)	0.45 W/(cm·K)

The bandgap energy versus lattice constant of the III-Nitride material system is shown in Figure 2.1. The material system spans a wide coverage of spectrum from the deep UV, the near UV, to the visible and even to the near infrared. Furthermore, the energy band gap could be tailored precisely by controlling the alloy content of AlN, GaN and InN, allowing to adjust the emission wavelength from the device.

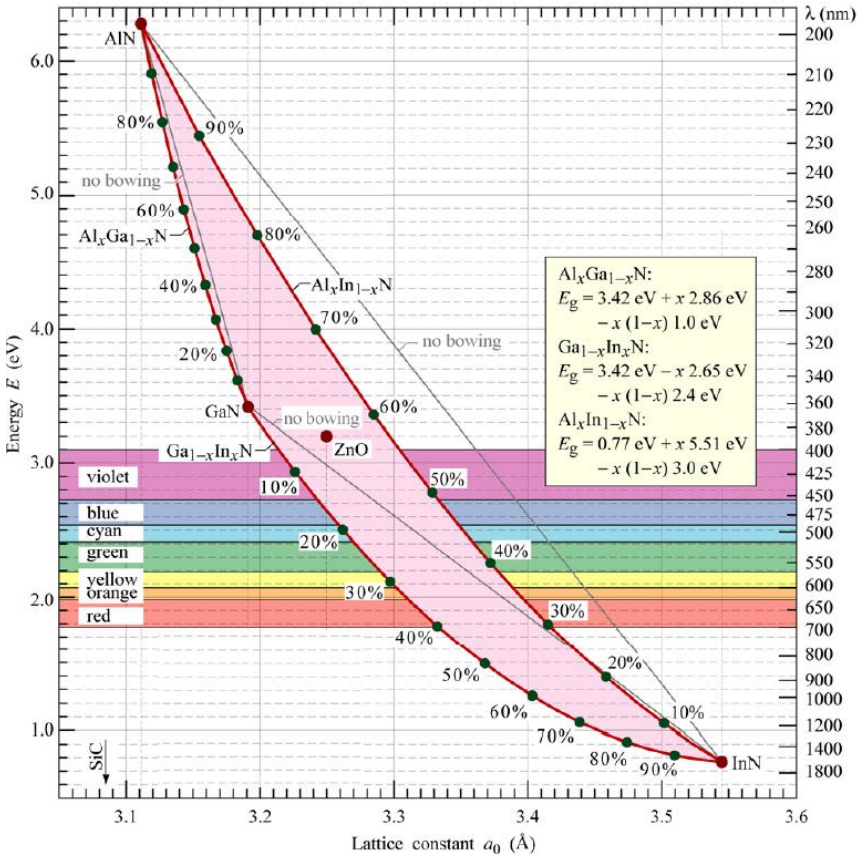

Figure 2.1 Bandgap energy (and corresponding emission wavelength) versus lattice constant of III-V nitride compound semiconductors at room temperature [30].

2.1.2. Polarization Effects in III- Nitrides

Most of the epitaxial growth of the III-Nitrides takes the [0001] growth orientation of the hexagonal wurtzite structure, leading to accumulation of polarization charges located at the surfaces of a layer. Consequently, the charges may induce internal electric fields in the thin film structure and significantly influence the optical and electrical properties of the devices.

These charges could be classified as the spontaneous polarization charges and the strain-induced or piezoelectric polarization charges [31-33]. The direction of the internal electric field depends on the strain and the growth orientation (Ga face or N face), as shown in Figure 2.2. The epitaxial nitride layer may experience compressive

or tensile strain when deposited on another epitaxial film with slightly different lattice constant. For the compressive strain case, the epitaxial layer is compressed laterally in the growth plane. For example, as InGaN is deposited on a thick relaxed GaN layer, the InGaN layer is compressed since the lattice constant of InN is larger than that of GaN. While in the tensile strain case, e.g. AlGaN deposited on relaxed GaN, the epitaxial layer tends to be expanded along the lateral direction.

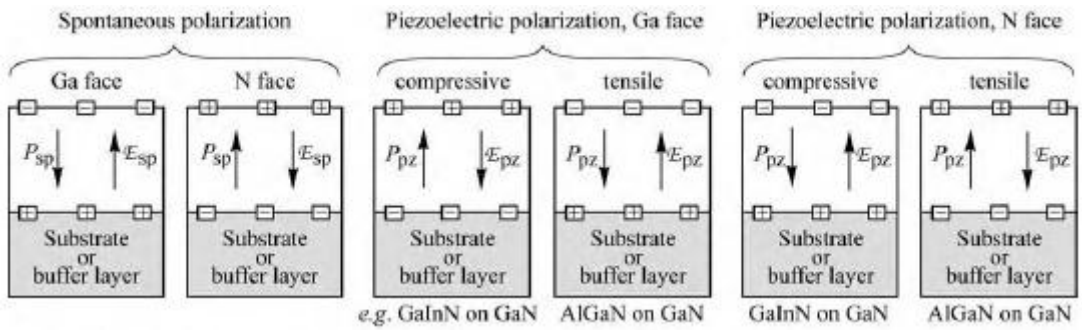

Figure 2.2 Surface charge and direction of electric field and polarization field for spontanesous and piezoelectric polarization in III-Nitrides for N and Ga face growth orientation [30].

The internal polarization field modifies the energy band structure, leading to spatial separation of electrons and holes, thereby suppressing the efficiency of radiative recombination within the quantum well structure. Meanwhile, the energy band tilting reduces the effective band gap, resulting in the red shift of the emission wavelength. The effect is known as quantum-confined Stark effect (QCSE).

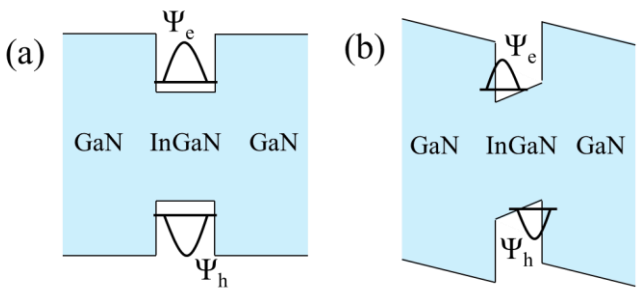

Figure 2.3 Schematic diagram for InGaN/GaN quantum well structure (a) without and (b) with polarization field.

2.2. LED Efficiency

The ideal LED device emits one photon for each electron injected into the active region, and hence can reach the maximum internal quantum efficiency (IQE, η_{IQE}) of unity. Here the IQE is defined as the ratio between the number of photons emitted by the active region and the number of electrons injected into the device, or

$$\eta_{IQE} = \frac{P_{\text{int}}/(h\nu)}{I/e}$$

where P_{int} is the optical power emitted from the active region, ν is the frequency of the photon, and I is the injection current.

However, all of the light emitted by the active region is not able to escape from the high refractive index medium of the LED device into the air with low refractive index and be received by eyes or detectors. A certain portion of light is lost within the device due to the total internal reflection (TIR) or reabsorption. The ratio between the photons extracted from the device and the number of photons generated by the active region is defined as the light extraction efficiency (η_{LEE}). Hence, the external quantum efficiency (EQE), referring to ratio of the number of detectable photons and the number of injected electrical charges, could be obtained from:

$$\eta_{EQE} = \frac{P_{LOP}/(h\nu)}{I/e} = \eta_{IQE} \times \eta_{LEE}$$

where P_{LOP} is the optical output power emitted by the LED into the ambient space.

Ideally, the LED device should have constant quantum efficiency at different current injection levels, so that the LED chip is able to generate high lumen flux at higher working current. However, in reality, a reduction of EQE at increased injection current density is observed, which is well known as efficiency droop. The root cause for the efficiency droop is being heavily investigated, and various physical models have been proposed to explain the phenomenon, including carrier electron leakage [34, 35], electron overflow [35, 36], Auger recombination [37-39], thermal heating [40, 41] and reduced radiative recombination caused by carrier-carrier and carrier-photon collisions [42].

Correspondingly, various structure designs have been proposed to overcome the droop issue. To suppress the electron overflow, different electron blocking layer structures have been studied and designed to confine the electrons within the MQW active region, instead of overflowing into the p-GaN layer [43-47]. MQW structures with varied well/barrier thickness, AlInN quantum barriers, and graded material composition [48-52], have also been reported to homogenize the hole distribution. Therefore, the radiative recombination of electrons and holes within the MQWs is more uniform, suppressing the chances for carrier overflow. Besides, the improved hole distribution within the MQWs helps to avoid the carrier overcrowding, reducing the non-radiative Auger recombination of the electrons and holes.

2.3. Light Extraction Efficiency of Light-emitting Diodes

The intensity of optical emission from the LED chip is determined by both the internal quantum efficiency and light extraction efficiency (LEE). While the IQE of the InGaN/GaN LED could be achieved as high as about 80% [53, 54], the challenging issue is the capability of extracting the generated photons out from the device material. Due to the large refractive index contrast between the GaN layer (n_{GaN} = 2.52) and the air medium (n_{air} = 1), the light emitted from the active region tends to be trapped within the GaN layer by the total internal reflection (TIR) at the GaN/air interface [55]. A portion of the photons emitted within the critical angle ($\theta = \arcsin(n_{air}/n_{GaN})$) are able to escape into the air. However, other photons with an incident angle larger than the critical angle are fully "repelled" back. As a result, most photons will be lost within the GaN layer, bringing down the energy conversion efficiency of the LED device significantly. According to one-dimensional calculations, the extraction efficiency from GaN LED device to air is limited to ~ 30% [56, 57].

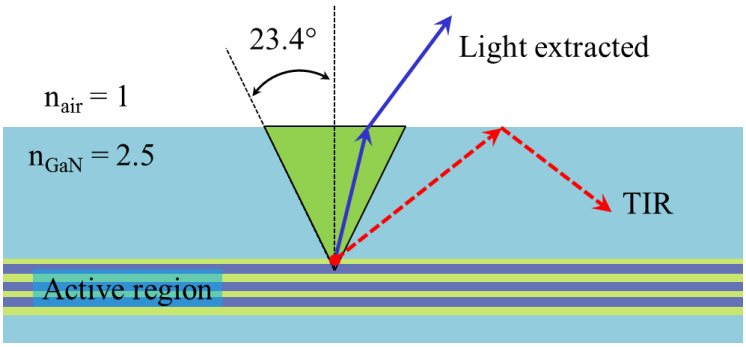

Figure 2.4 Light trapping at the GaN/air interface by total internal reflection (TIR), due to the refractive index difference between GaN and air medium.

To avoid the adverse effect of the TIR phenomenon on LEE, tremendous efforts have been contributed to improve the LEE of GaN LED devices, including patterned sapphire substrates [58, 59], anti-reflection coatings [60, 61], surface roughening [62-

65], photonic crystals [57, 66, 67], nanowire-based LEDs [68, 69] and adoption of surface plasma resonance [70].

The anti-reflective coatings are normally achieved through deposition of multiple layers of materials with graded refractive indices (GRIN), for example, as shown in Figure 2.5(a). The six ITO layers were deposited with different incident ITO vapor flux angles, resulting in oriented rod-like ITO layers with different porosity levels. As the refractive index reduces from 2.19 near the p-GaN interface to 1.17 near the air interface, the thickness of the dense ITO is kept quarter wavelength thick. Therefore, the GRIN AR coating is able to fully eliminate the Fresnel reflection, given that the refractive index is continuously varied from the substrate's index (n_{GaN}) to the ambient index. The calculated reflectivity at normal incidence shows that the GRIN ITO AR coating exhibited a much lower reflectivity than the GaN surface with no AR coating and that with conventional ITO AR coating, as shown in Figure 2.5(b). As a result, the devices with GRIN ITO AR coating show 24.3% higher light output than LEDs with dense ITO coating at the injection current of 20 mA [60].

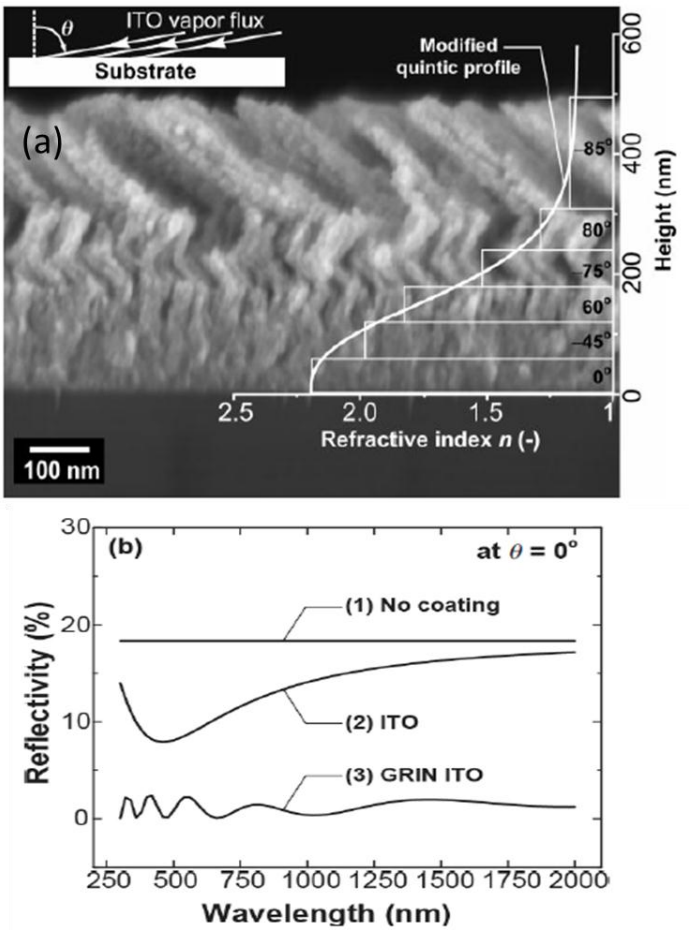

Figure 2.5 (a) Cross-sectional SEM image of graded-refractive-index (GRIN) anti-reflective (AR) coating ITO layers; and (b) comparison of calculated reflectivity of GaN surface with no coating, conventional ITO coating and the GRIN coating [60].

Another solution for the light extraction problem is to apply photonic crystals (PhCs). The PhC structures, which are periodic patterns of alternating refractive indices with dimensions comparable to the wavelength of photons, could be formed directly on the GaN surface [71] or on an intermediate layer between the GaN and the ambient [72, 73]. With the PhC structures, the light extraction efficiency could be enhanced by over 2.5 times [74]. Through nano-fabrication technology, different PhC structures with various of material composition, lattice periodicity, symmetry and topology can be designed and realized [74, 75].

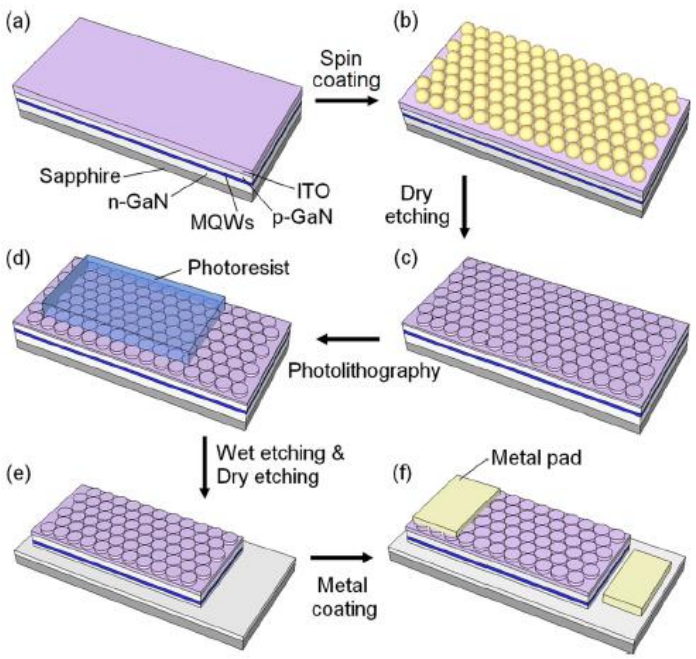

Figure 2.6 Schematic process flow for the fabrication of ITO photonic crystal: (a) the starting LED wafer; (b) silica spheres spin-coated onto the ITO layer; (c) ICP etching of ITO and sphere removal; (d) mesa definition via photolithography; (e) n-GaN exposure through dry etching; and (f) metal pad deposition [73].

Surface roughening is another simple but effective approach to improve the light extraction efficiency. The light extraction efficiency can be enhanced by up to 2.3 times after the surface roughening process [63, 65]. Random texture could be realized through chemical wet etching. By controlling the etching time and the concentration of the etchant solution, the surface roughness could be adjusted, which will in turn influence the enhancement factor of the light extraction efficiency through increased scattering.

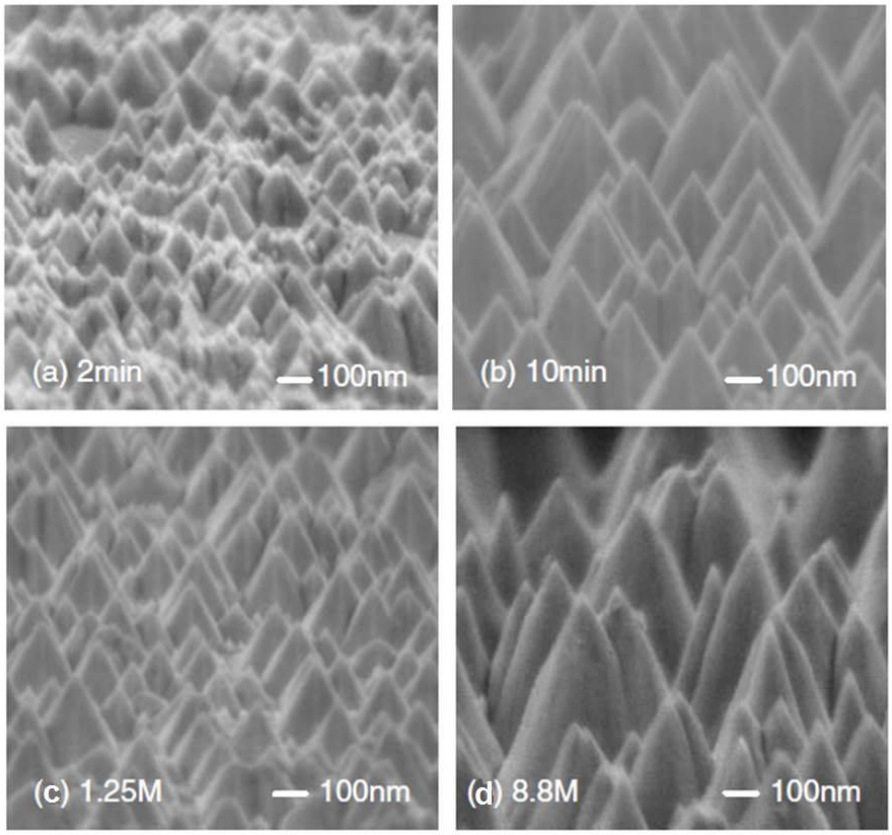

Figure 2.7 Scanning electron microscopy images of n-face GaN etch morphology: after etching (a) 2 min and (b) 10 min in 2.2 M KOH solution; and after 10 min etch in (c) 1.25 M and (d) 8.8 M KOH solution [76].

2.4. White Light Source for Lighting and Display Applications

Besides the brightness and energy conversion efficiency, the photometric quality a white light source is also of great importance for lighting and display applications. A black-body white light source, take the sunlight for an example, consists of all color components within the visible spectrum range (380 - 700 nm). However, it may also contain photons at wavelengths extended into the invisible ultraviolet and ultra-red region, which is unnecessary for lighting [77]. The incandescent and halogen lamps are able to generate similar light spectrum as the sunlight, possessing higher color rendering quality as compared to the fluorescent lamp, which covers only a few

narrow spectrum bands in the visible light region. The LED based lamps, as shown in Figure 2.8, are in principle able to cover most of the visible spectrum region depending on the design. Furthermore, it is flexible to adjust the spectrum combination to achieve white light with ultra-high photometric qualities [78].

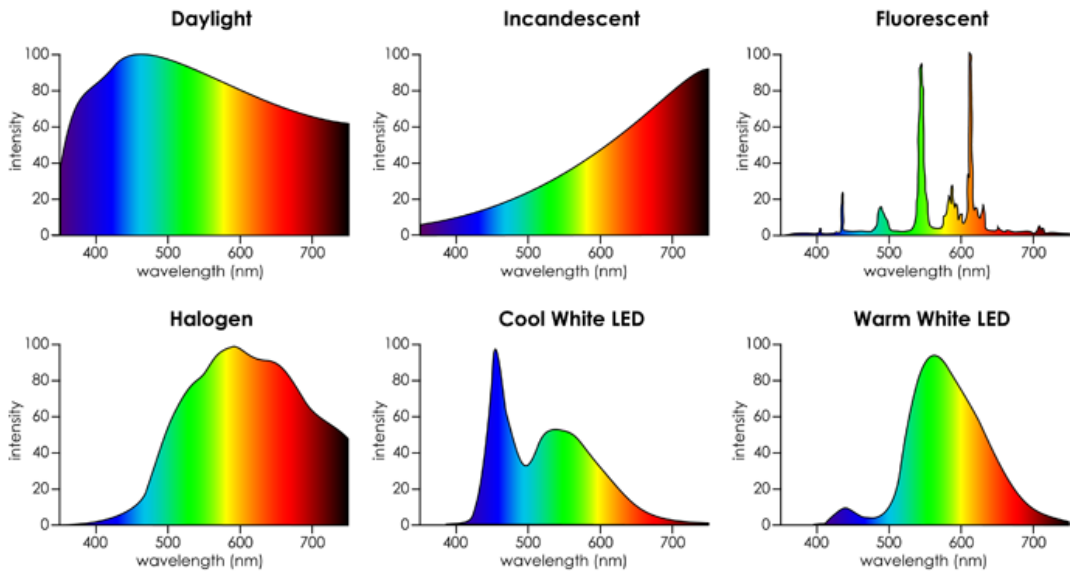

Figure 2.8 Spectra of white light emitted from different lighting sources: natural daylight, incandescent lamp, fluorescent lamp, halogen lamp, and cool and warm white LEDs [77].

Two figure-of merits are commonly adopted to evaluate and compare the quality of different white light sources, namely, the color rendering index (CRI) and the correlated color temperature (CCT). The CRI is a quantitative metric of the ability of a particular light source to reflect the original colors of various objects in comparison with a natural light source. The CCT, in the unit of Kelvin (K), refers to the visual temperature of an ideal black body radiator that emits light with comparable hue to that of a light source. The value of CRI plays an important role in the application of photography and display backlight. As the temperature of a light source increases

from 2,500 to 10,000 K, the visual temperature goes from reddish (or “warm”) to bluish (or “cold”).

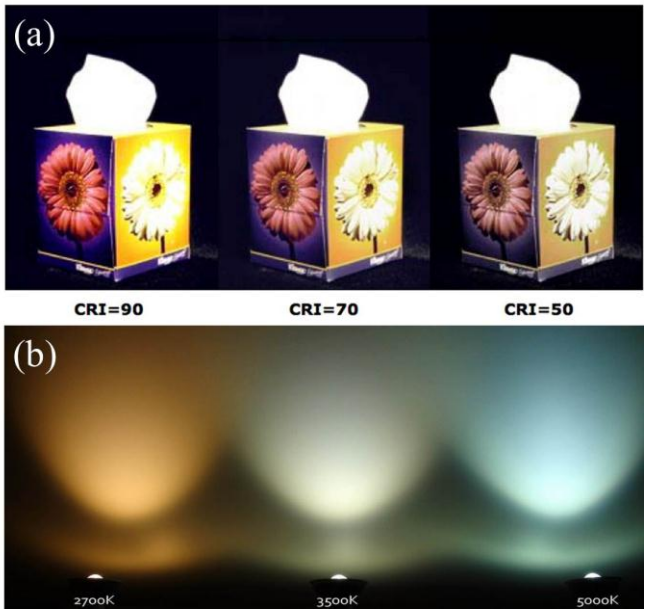

Figure 2.9 (a) Tissue box under illumination of light sources with different CRI; and (b) White light sources with CCT of 2700, 3500 and 5000 K [79, 80].

The three basic approaches to achieve white light generation are presented in Figure 2.10 [81]. The first approach is to combine the blue LED chip with yellow phosphor material, like the cerium (III)-doped yttrium aluminum garnet (Ce:YAG) [82]. These LED chips show high brightness, high efficiency and low cost, but poor performance of CRI and CCT. A modified version of this approach is to use red and green emitting phosphors together with blue LEDs, which provides a good compromise between the color quality and the overall efficiency. The second approach is to convert the ultraviolet light to blue/yellow lights through phosphor mixtures. The device design based on this design is able to provide better CRI and CCT values. However, the overall chip efficacy is lower, due to the low energy

conversion efficiency of the UV LED chip. The most promising way to hold both the high optical quality and high efficacy is to integrate three (or more) single color LED chips into one device. However, the high cost is still a barrier for this scheme to be widely used. Another modification is to use blue LEDs in conjunction with red LEDs together with green phosphors. This is a hybrid version of color conversion and multi-chip approaches. Currently, the blue LED chip/yellow phosphor (or green/red phosphors) combination dominates the overall white LED sources, and continues to attract more research focus for its performance optimization.

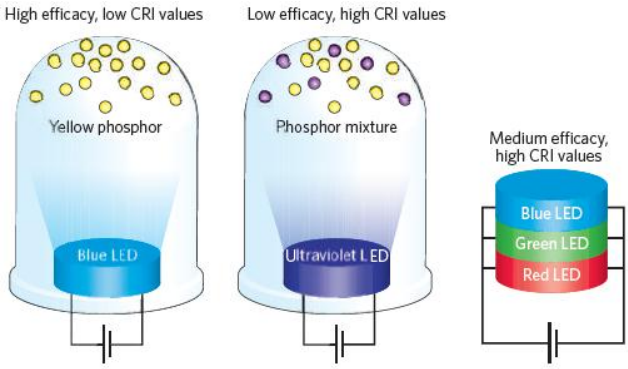

Figure 2.10 White LED configurations: blue LED chip with yellow phosphors, ultraviolet LED chip with blue and yellow (and red) phosphors; and multi-chip device consists of blue, green and red LED chips [81].

Besides the conventional rare-earth based phosphor materials, nano-sized semiconductors, also known as colloidal quantum dots, have also been applied for the fabrication of white light LED chips [83, 84]. These color convertors enable rich color component coverage over the visible spectrum range, and freedom of color adjustment through particle size control. By integrating the CdSe/ZnS core-shell nanoparticle QDs of different sizes, corresponding to green, yellow and red wavelengths, with a blue light emitting InGaN/GaN LED chip, a white light source

with remarkable photometric performance parameters (CRI of 89.2, and CCT of 2.982K, luminous efficiency of optical radiation equal to 357 lm/W_{opt}) has been achieved [78, 85].

Chapter 3. Epitaxial Growth and Device Fabrication of Gallium Nitride Light-emitting Diodes

In this chapter, the epitaxial growth process of InGaN/GaN MQW LED wafers using metal-organic chemical vapor deposition (MOCVD) technique is explained in detail. Subsequently, the fabrication process for LED chips in different chip sizes (350 μm × 350 μm and 1 mm × 1mm) is demonstrated. Characterization methods and results at wafer-level and chip-level are discussed.

3.1. Epitaxial Growth of GaN LED Wafers

3.1.1. Metal-Organic Chemical Vapor Deposition (MOCVD)

In this thesis, the GaN LED epitaxial wafers are all grown using the metal-organic chemical vapor deposition (MOCVD) system from AIXTRON®, with a production capability of 3 substrates of 2-inch wafer. The schematic drawing of the system is illustrated in Figure 3.1. The source of group-III metals (aluminum, gallium and indium) are prepared as metal-organic (MO) compounds, stored in bubbler containers, and transferred into the reactor by a carrier gas (hydrogen or nitrogen), while group-V element, nitrogen, is delivered into reactor in the format of gaseous ammonia through the hydride line. Silane (SiH_4) gas and Bis(cyclopentadienyl)magnesium (Cp_2Mg) are used to provide the n-type and p-type dopants in the III-Nitride, respectively. The content of each material source is precisely adjusted by a series of mass flow

controllers (MFC) and pressure controllers (PC), so that the growth rate and doping concentration of the GaN layer can be controlled.

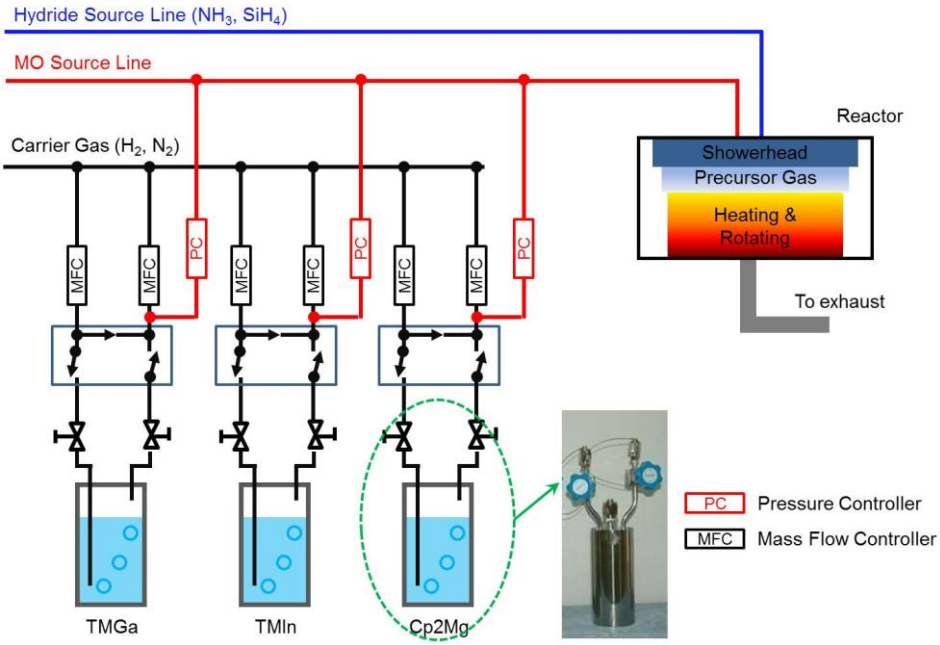

Figure 3.1 Schematic diagram of a MOCVD system: gas delivery path and reactor.

The reactor adopts a close coupled showerhead (CCS) configuration, which delivers the gas phase precursors through small pin holes on a planer showerhead, as shown in Figure 3.2(a). The substrate wafers are placed in the pockets of a graphite susceptor, underneath which the tungsten heaters are located (Figure 3.2 (b)). To ensure uniform heating across the whole wafer region, the susceptor rotates throughout the whole growth process. Besides, the heaters are typically divided into three separated heater zones, to provide balanced thermal heating through related settings, as is the case in our reactor illustrated in Figures 3.2(c) and 3.2(d).

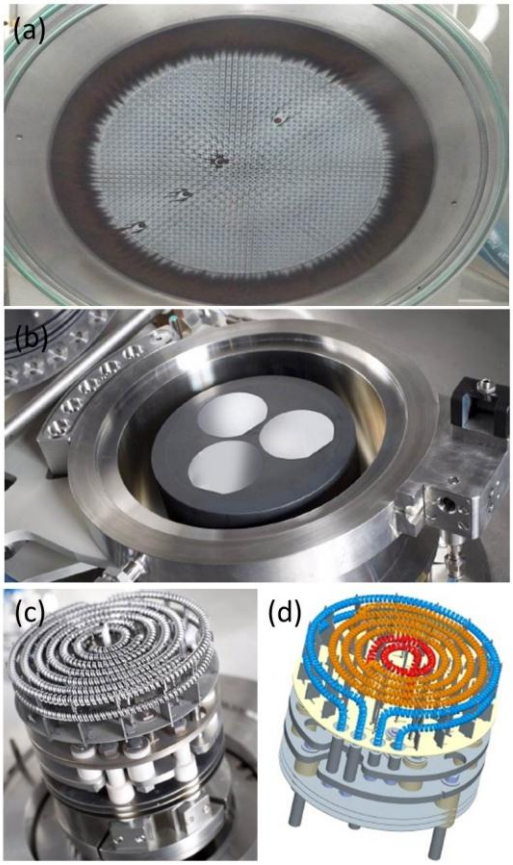

Figure 3.2 MOCVD reactor: (a) showerhead for gas precursor delivery; (b) rotating susceptor holding wafer substrates during growth; (c) tungsten heater underneath the susceptor; and (d) schematic diagram showing circular heater zones.

Inside the reactor, the following chemical reaction takes place for the formation of GaN compounds:

$$M(CH_3)_3 + NH_3 \xrightarrow{Heat} MN + 3CH_4$$

where M = Ga, Al, or In. As illustrated in Figure 3.3, after reaching the surface of the reaction site, i.e., the substrate surface, the MO sources (TMGa, TMAl, TMIn, TEGa) and hydrides are first decomposed into single atoms of gallium (or aluminum/indium) and nitrogen under high temperature heating. The atomic Ga and N adhere to the substrate surface and form GaN compound. Meanwhile, the unreacted materials and

byproducts are desorbed. The dopant precursors (Cp_2Mg and SiH_4) take part in the same reaction, forming doping atoms within the bulk GaN film.

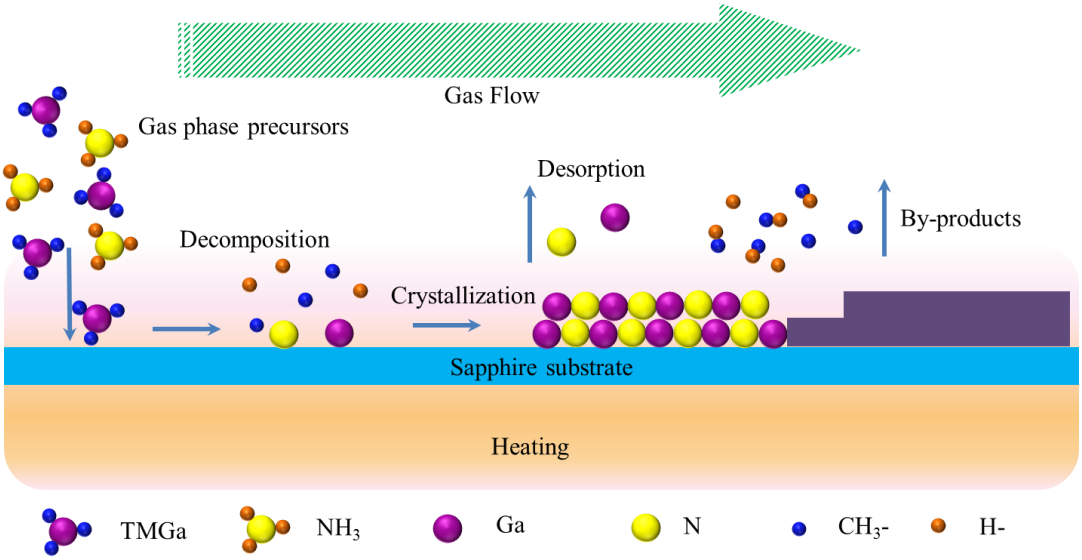

Figure 3.3 Schematic diagram of MOCVD reaction mechanism.

3.1.2. Epitaxial Growth of High Quality GaN Films

The growth process of high crystal quality GaN film is demonstrated in Figure 3.4. Due to the lattice mismatch between the GaN lattice and the sapphire (Al_2O_3) crystal substrate, a low temperature buffer layer is first grown on the non-native bare sapphire substrate, followed by a high temperature annealing, which turns the amorphous GaN layer into crystallized GaN seed layer. Those crystal seeds serve as growth center for the following GaN deposition. Therefore, the crystal seeds grow into discrete islands as the growth continues. After further deposition, the islands coalesce to the bulk GaN film, and the defect edges of the crystal seeds are greatly cured.

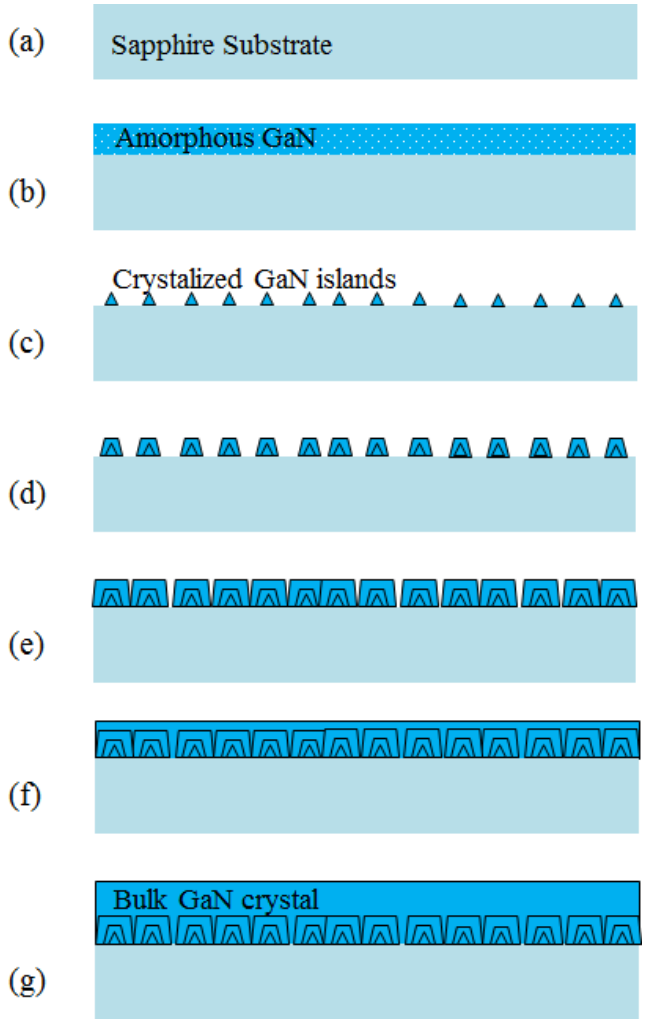

Figure 3.4 Epitaxial growth process of GaN crystal film on a sapphire substrate: (a) bare sapphire substrate; (b) deposition of amorphous GaN film with thickness ≈ 25 nm at low temperature; (c) high temperature annealing to form crystalized GaN seeds; (d) - (e) formation of crystalized GaN islands; and (f)-(g) formation of bulk GaN film.

Based on this growth scheme, epitaxial GaN LED wafers with high crystal quality were grown on (0001) *c*-plane sapphire. The LED wafers were scanned using high resolution X-ray diffraction system (HRXRD, Philips PW3040). The omega scan results show that the epitaxial films have a diffraction peak with a full width at half maximum (FWHM) of 221.8 arcsecond on [002] orientation, and 208.4 arcsecond on [102] orientation, indicating excellent crystal quality.

3.1.3. Epitaxial Growth of GaN LED Wafers

The epitaxial structure of a typical InGaN/GaN LED, as illustrated in Figure 3.5, consists of a 4 μm thick unintentionally doped GaN (u-GaN), a 4 μm thick n-type doped GaN (n-GaN:Si), a number of pairs of quantum wells/quantum barriers (with thickness of 3 nm /12 nm), and finally a 200 nm thick p-type doped GaN (p-GaN:Mg) layer. The n-GaN and p-GaN layers allow for current injection to the MQW active region, and serve as the contacts with metal electrodes deposited in the device fabrication process.

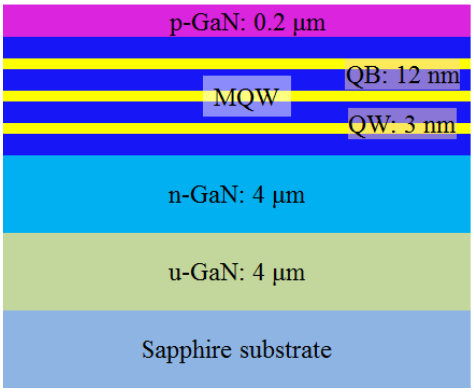

Figure 3.5 An exemplary structure diagram of a typical InGaN/GaN MQW LED wafer.

Throughout the epitaxial growth, the surface smoothness and growth rate are monitored through in-situ optical probing. A laser beam (at a wavelength λ = 630 nm) is reflected back at near-normal incidence to the interfaces - interface between air and the GaN film, and that between the GaN film and the sapphire substrate. The reflected beams form constructive/destructive interference with varying GaN film thickness during the growth. The thickness of GaN film (*d*) can be calculated through

$$d = \frac{\lambda}{2 \cdot n_{GaN}}$$

where n_{GaN} is the refractive index of GaN film. Therefore, the film thickness, as well as the growth rate, of the GaN epitaxial layer can be obtained.

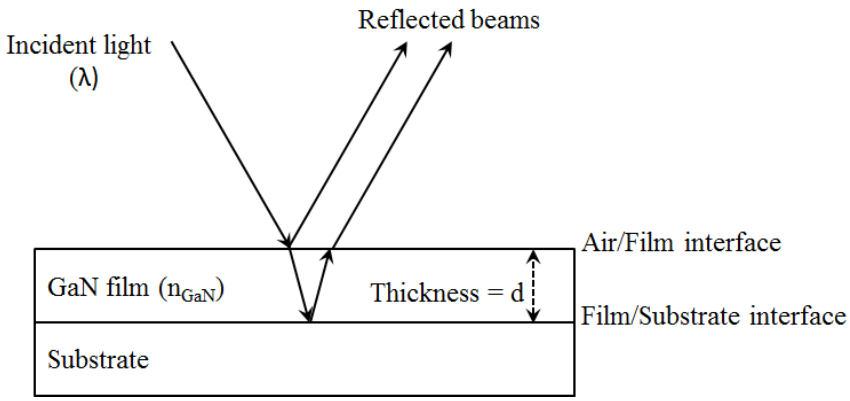

Figure 3.6 *In-situ* reflectance monitoring through interference between the reflected light beams.

The temperature and *in-situ* reflectance profile are shown in Figure 3.7, for various exemplary complete growth runs of LED epitaxial structures illustrated in Figure 3.5. The growth typically starts with a high temperature baking in hydrogen ambient to clean the surface of the sapphire substrates (Stages (a) and (b)). Following that, a low temperature amorphous GaN layer is grown. The smooth GaN surface leads to more reflection of probing laser light, hence the reflectance is increased. The following high temperature baking transfers the amorphous GaN film into crystallized GaN seeds, resulting in a roughened surface. Besides, since most of the GaN material is decomposed by the high temperature baking, the surface of the sapphire substrate is exposed. Hence, the reflectance is decreased back to the level close to the sapphire substrate surface (Stage (c)). The reflectance curve further drops down as the growth continues (Stage (d)), since the formation of larger crystal islands makes the surface even rougher, and the incident light beam is highly scattered away from the reflection direction. However, after the coalescence of the crystal islands, a continuous GaN

film with a smooth surface is formed. Consequently, a periodic oscillation of reflectance curve is observed for the u-GaN and n-GaN growth (Stages (d) and (e)). During the growth of multiple quantum wells, the growth rate is slowed down, and the thickness of the quantum well is in the scale of nanometers, such that the reflectance cannot make up full oscillations (Stage (f)). Finally, the p-GaN growth and dopant activation by *in-situ* thermal annealing was followed to finish the complete LED structure (Stages (g) and (h)).

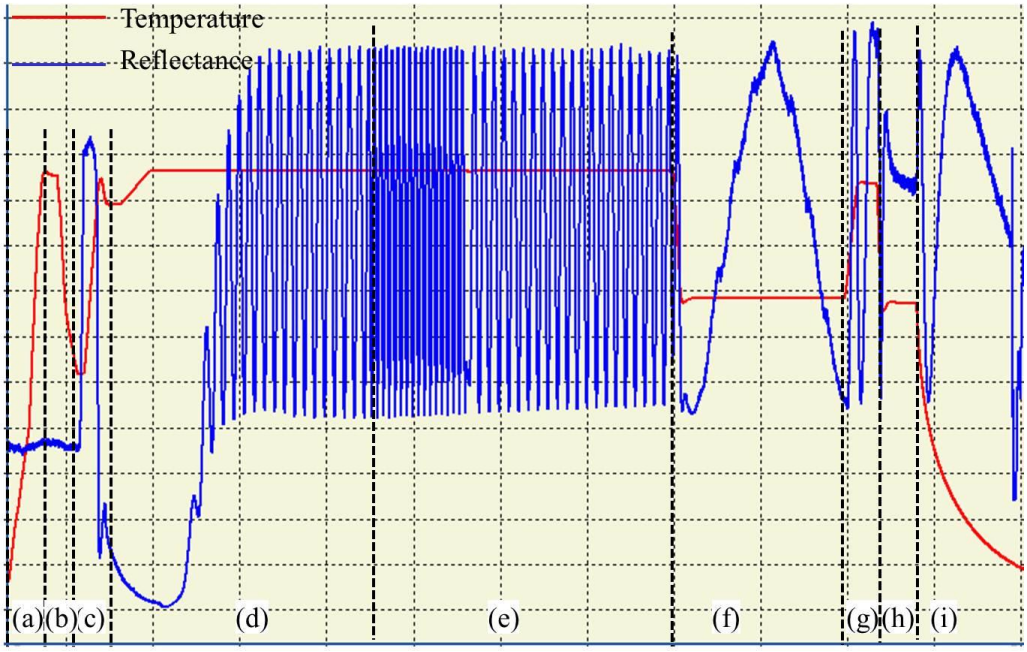

Figure 3.7 *In-situ* temperature and reflectance monitoring of GaN LED growth stages: (a) temperature ramp-up; (b) high temperature bake; (c) nucleation; (d) u-GaN; (e) n-GaN; (f) quantum wells; (g) p-GaN; (h) *in-situ* p-GaN activation annealing; and (i) temperature ramp-down.

3.2. Wafer-level Characterization

The as-grown epitaxial LED wafer presents highly transparent appearance with a smooth surface, and can be lit at any point across the whole epi-wafer area, as shown

in Figure 3.8(a). When driven by a current source, the epi-wafer is able to generate a typical blue light emission, e.g., with a peak emission wavelength of 452 nm and s FWHM of 20.4 nm, as shown in the electroluminescence (EL) spectrum in Figure 3.8(b).

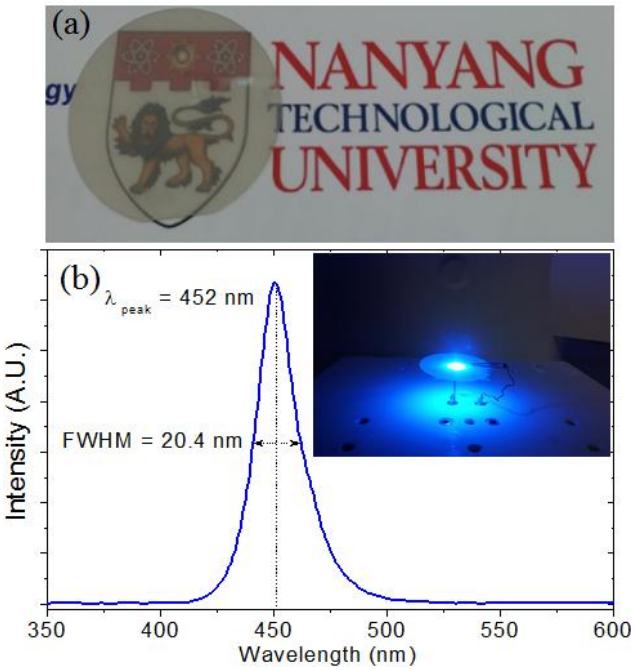

Figure 3.8 (a) A transparent GaN LED epitaxial wafer grown at *LUMINOUS!*; and (b) electroluminescence spectrum of our blue LED wafer as-grown (inset: LED epi-wafer lit under current injection).

The high-resolution X-ray diffraction (HRXRD) is performed using Philips PW3040 system, with Cu Kα (λ = 1.5406 Å) X-ray source. The epitaxial sample is scanned for the (002) plane using the 2θ-ω scan method. The scan range is from 30° to 40° with a scan rate of 2°/min. The diffraction intensity versus the 2θ spectrum is shown in Figure 3.9. The highest peak centered at 34.57° is corresponding to the bulk GaN (002) plane. Satellite peaks corresponding to InGaN quantum wells can be clearly identified from the spectrum, indicating well defined boundaries between the quantum wells and quantum barriers. A simple simulation is carried out based on the

position of the InGaN satellite peaks, assuming 100% strain within the MQW active region. And the results turns out that the epitaxial wafer has a quantum well thickness of 3.0 nm and quantum barrier thickness of 12.1 nm, being consistent with the designed thickness.

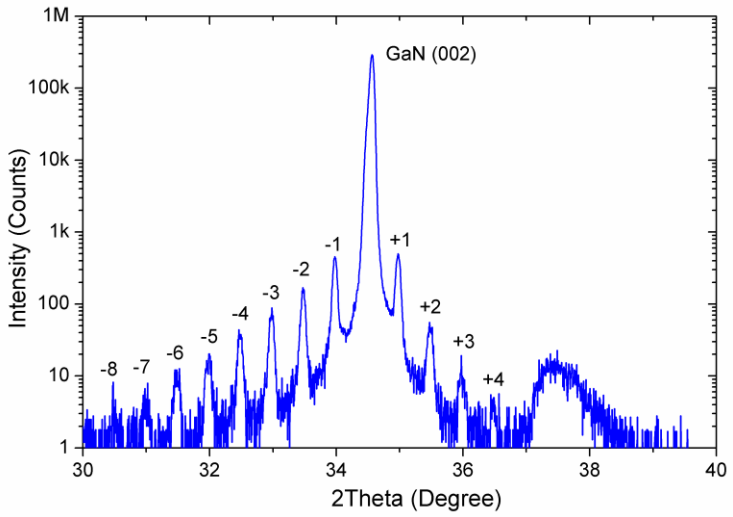

Figure 3.9 HRXRD ω-2θ scan curve of our InGaN/GaN LED epi-wafer.

To examine the uniformity of the epitaxial growth, the thickness and peak emission wavelength at different locations of the epi-wafer are recorded using a mapping system (Nanometrics ® RPM-2000), as shown in Figures 3.10(a) and 3.10(b). This exemplary epi-wafer has an average thickness of 8.75 μm with a standard deviation of 1.42%, and the average PL emission peak wavelength is at 456.4 ± 1.5 nm, indicating an excellent uniformity across the wafer region.

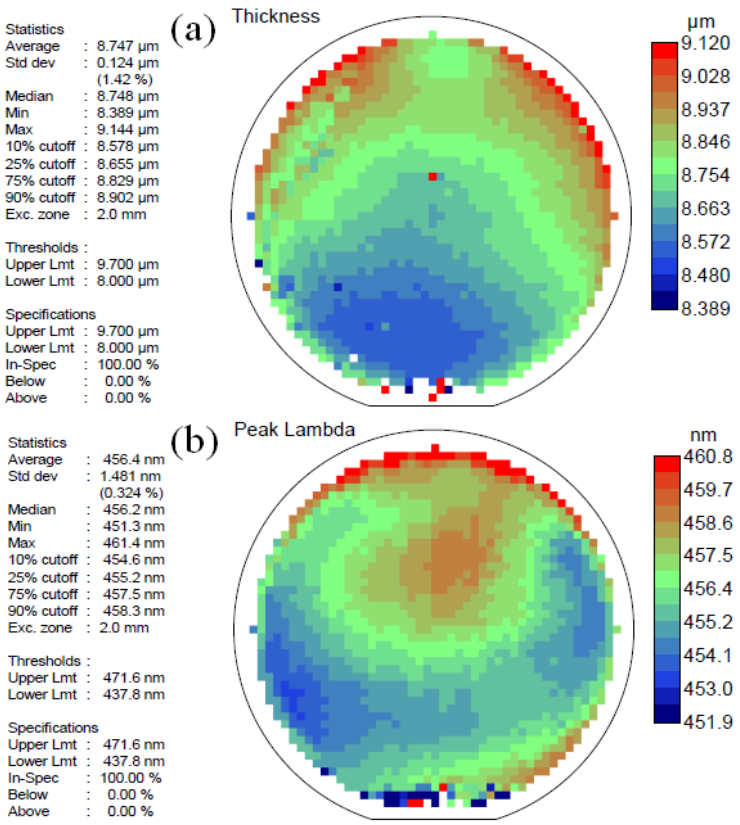

Figure 3.10 (a) Thickness mapping and (b) peak emission wavelength mapping of GaN LED epi-wafer of ours.

3.3. Fabrication of GaN LED Devices

After the growth, the epitaxial wafer is further fabricated into separated chips for accurate electrical and optical measurements. The fabrication of top-up structure device starts with mesa etching on the bare LED epi-wafer. The mesa etching is performed using reactive ion etching (RIE) and removes the p-GaN, MQWs and part of GaN, such that the n-GaN is exposed for electrode contact. Before the etching, the mesa is patterned using photolithography, and hence the emitting area of the LED chip is defined, as shown in Figures 3.11(a) and 3.11(b). After that, a current spreading layer is deposited on top of the p-GaN, serving as the current spreading and ohmic contact layer with p-GaN (Figure 3.11(c)). Finally, Ti/Au bilayer with a typical

film thickness of 30 nm/150 nm is deposited as contact pads for both the n- and p-electrodes (Figure 3.11(d)).

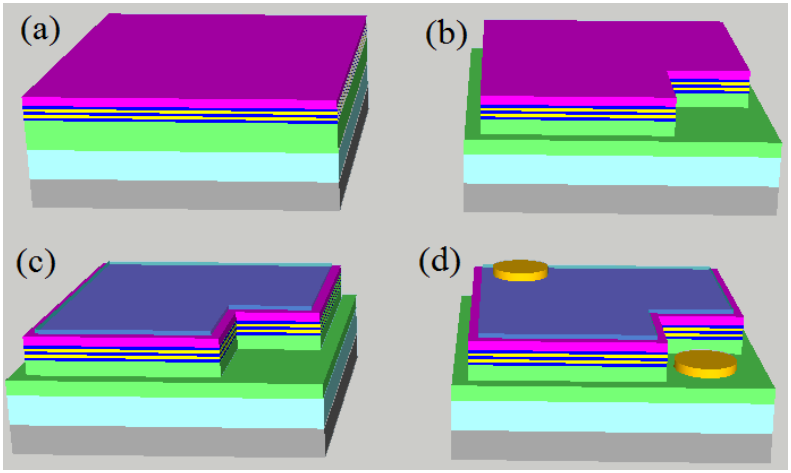

Figure 3.11 Fabrication process of LED device from (a) epitaxial LED wafer with the following process flow of (b) mesa etching; (c) deposition of transparent current spreading layer; and (d) deposition of metal contact pad.

Due to the difficulty of p-dopant activation and the large effective mass of holes, the p-GaN layer has a high resistance and lower carrier mobility. Hence, the current spreading within the p-GaN layer is limited, and it is also difficult to achieve ohmic contact between the p-GaN layer and metal contact, leading to a current crowding near the metal electrode. As a result, non-uniform light emission from the device area can be observed, as shown in Figure 3.12(a). Also, the device can present a high forward voltage due to the potential barrier at the interface. Therefore, a current spreading layer is necessary to spread the current out horizontally, so that the whole device region could be utilized for uniform light emission, as shown in Figure 3.12(b). Meanwhile, the current spreading layer should be as transparent as possible so that more light will be transmitted.

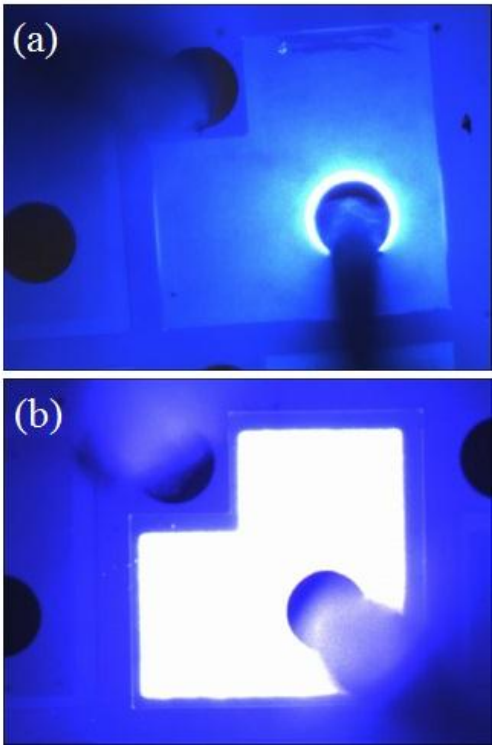

Figure 3.12 Fabricated LED devices under current driving: (a) without a current spreading layer; and (b) with an annealed Ni/Au current spreading layer (device mesa area = 350 × 350 μm^2).

In this study, a thin layer of Ni/Au was deposited and annealed to function as the transparent current spreading layer. To maximize the light transmission, the thickness of Ni/Au layer was designed to be 2.5 nm/2.5 nm and 5 nm/5 nm for comparison. Additionally, rapid thermally annealing (RTA) was conducted at 550 ℃ for 5 min, to oxidize the Ni layer into NiO seeds, and form low resistive ohmic contact with the p-GaN [86], while the continuous gold film will spread out the current horizontally across the whole device region. The metal deposition and annealing conditions are listed in Table 3.1.

Table 3.1 Deposition and annealing conditions of Ni/Au current spreading layers.

	Film thickness	Annealing ambient	V_f @ 20 mA	Transmittance*
I	2.5 nm/2.5 nm	O_2/N_2 mixture	4.94 V	82.13%
II	2.5 nm/2.5 nm	O_2	4.46 V	84.21%
III	5 nm/5 nm	O_2/N_2 mixture	3.65 V	65.07%
IV	5 nm/5 nm	O_2	3.18 V	74.81%
* Optical transmittance measured at 450 nm.				

It can be seen that with a thinner Ni/Au metal layer, the current spreading layer leads to higher transmittance, allowing more light to be transmitted. However, the contact condition for this thin layer combination is not optimized, as indicated by the high forward voltage measured after completing the whole fabrication process. On the other hand, the thicker Ni/Au with a thickness of 5 nm/5 nm exhibits better electrical performance, but a lower level of light transmission through the current spreading layer. It is also found that the annealing in pure oxygen ambient leads to better results for both electrical and optical performances. Therefore, a Ni/Au layer of thickness 5 nm/5 nm, annealed at 550 ℃ in pure O_2 for 5 min, is adopted as the transparent current spreading layer in the device fabrication presented here.

For high power and high brightness lighting applications, the devices are injected with higher current. Hence, the LED chips are also fabricated with a larger chip size, for example, 1 mm × 1 mm for 350 mA operating current. However, as the mesa area increases, the issue of lighting uniformity becomes critical, as the current spreading capability of the n-GaN and current spreading layer is limited. To overcome this problem, n- and p-electrodes with multi-finger patterns are applied to assist the current spreading, as shown in Figure 3.13. With the multi-finger configuration, the device is able to emit uniformly.

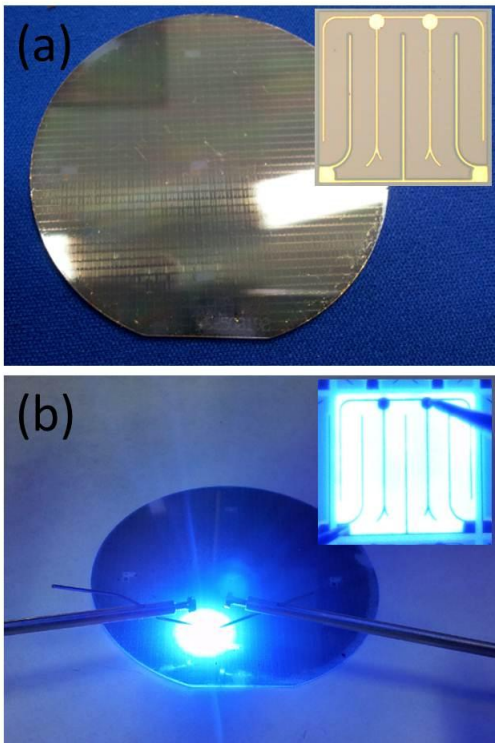

Figure 3.13 High power LED chips with a device area of 1 mm × 1mm: (a) chip-on-wafer without driving current (inset: optical microscopy image of a single LED die); and (b) fabricated chip lit-up with driving current (inset: a lit-up chip in microscope view).

3.4. Chip-level Characterization

The fabricated devices are characterized at the chip-level to test the electrical and optical performance. Figure 3.14 presents the measured I-V characteristics of the fabricated chip with a 350 μm × 350 μm mesa area. The device has a forward voltage of 3.2 V at 20 mA current level, and the light emission is very uniform with the Ni/Au used as the current spreading layer.

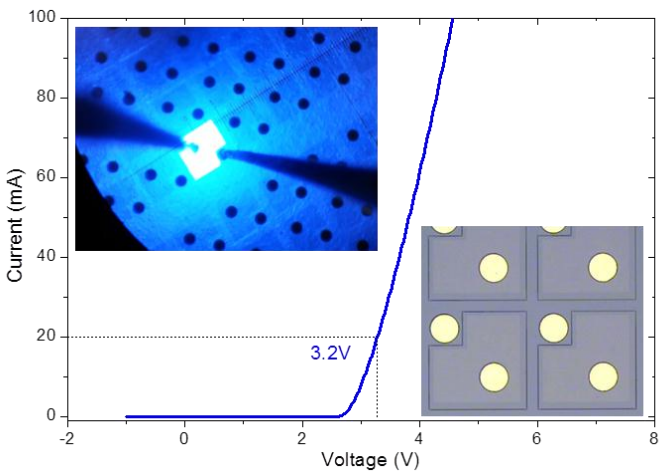

Figure 3.14 Measured I-V characteristics of a fabricated LED chip-on-wafer (Inset-up: LED chip driven at 20 mA; inset-down: optical microscopy image of the fabricated LED devices).

The optical output power of the chip is measured using an integrating sphere and the external quantum efficiency (EQE) is extracted. Figure 3.15 shows the current-dependent EQE and optical power measured for a fabricated device. An efficiency droop of 20.78% is observed at 150 mA injection current.

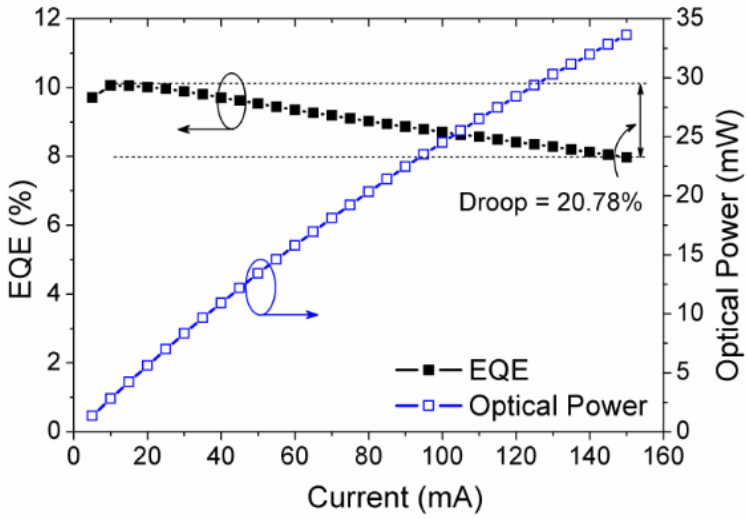

Figure 3.15 Current-dependent optical output power and external quantum efficiency (EQE) of a fabricated LED chip-on-wafer (device area = 350 μm × 350 μm).

The measured values of the optical output power, and thus the extracted external quantum efficiency, presented here are not optimized in this device, as the back end processes has not been involved. The parameters can be improved through dicing the wafer into single LED chips; depositing reflective mirrors at the backside of non-conductive substrate; adopting light extraction structures by surface roughening or photonic crystals; and replacing the Ni/Au with transparent current spreading layer to further reduce light absorption.

3.5. Conclusion

Here, the epitaxial growth mechanism and process of InGaN/GaN multiple quantum well LED structure using metal-organic chemical vapor deposition technique is explained in detail. A typical blue-emitting GaN based LED epitaxial wafer with high thickness and emission uniformity is demonstrated. The fabrication process of typical top-up structure LED chips is also illustrated. Electrical and optical characterization of LED structures at wafer-level and chip-level is performed. The growth, fabrication and characterization process will be used as the starting procedure in all the proposed structure designs in the following chapters.

Chapter 4. p-Type Doped Quantum Barriers for Enhanced Hole Transport

In this chapter, the hole transporting behavior within the multiple quantum wells active region is studied through dual wavelength emission method. The quantum wells were purposely grown at two different temperatures, so that the LED samples emit light with two spectral peaks, due to different indium incorporation. Through investigating emission intensities at different peaks, we are able to identify the hole penetration depth within the multiple quantum wells region. The experimental results show that for conventional LEDs with undoped quantum barriers, light emission is mainly from shallow quantum wells near p-GaN layer. The deep well emission only occurs under a high current level. However, with the proposed p-type doped quantum barrier structure, the holes are able to penetrate deeper even under low current injection, increasing the radiative recombination within the active region. Moreover, the enhanced hole transport leads to improved electrical performance. The conclusion is further verified by numerical analysis on the hole distribution within the multiple quantum well region. This chapter is partially based on “Enhanced hole transport in InGaN/GaN multiple quantum well light-emitting diodes with a p-type doped quantum barrier” published in *Optics Letters*, Vol. 38, No. 2.

4.1. Introduction

Hole transport, including spreading in horizontal direction and penetration in vertical direction, has always been a challenging issue that limits the performance of LED devices. Zhang *et al.* illustrated the enhanced hole spreading performance by applying a p/n/p/n/p-GaN multilayer structure in the p-GaN region [87]. In this part, we are going to address the hole transport into the depth of multiple quantum wells (MQW) region. Due to the difficulty of hole penetration [88], excessive electron injection is commonly adopted to maximize chances of radiative recombination of carriers, resulting in electron overflow. Hence, an electron blocking layer is necessary to prevent electrons from leaking into the p-GaN region. Different approaches to enhance hole transport have been reported, including replacing GaN quantum barriers (QBs) with AlGaN layer [89], varying quantum well thickness [90], applying graded-composition QBs [91], and p-type doped last QBs [92]. Also, Liu *et al.* and Han *et al.* numerically examined the effect of a p-type doped barrier on hole transport and hole distribution [93, 94]. However, the hole transport behavior under different current injection levels has not be reported to date. Here, the hole transport behavior under different current levels is reported with a dual-wavelength emission method. By doping the last three barriers with magnesium, the light emission from deeper MQWs is found to be enhanced, indicating that the holes are able to travel deeper and the recombination volume has been increased.

4.2. Growth and Fabrication of LED Samples

The LED epitaxial wafers were grown on (0001) *c*-plane sapphire substrates using the MOCVD system. The epi-layers consist of a 30 nm thick low-temperature GaN

nucleation layer, a 150 nm thick interlayer [95], a 4 μm thick unintentionally doped GaN (u-GaN) layer, a 2 μm thick Si-doped n-GaN layer (doping concentration is 5×10^{18} cm^{-3}), eight pairs of InGaN/GaN multiple quantum wells, and 150 nm thick Mg doped p-GaN layer (with a doping concentration of 3×10^{17} cm^{-3}). The first five quantum wells (close to n-GaN layer, to be referred as "deep QWs") were grown at 730 ℃, followed by three quantum wells (close to p-GaN layer, to be referred as "shallow QWs") grown at 750°C. All the QBs have equal thickness of 12 nm, and were not doped in Sample I. For Sample II, a 2 nm p-doped GaN, with a doping concentration the same as that in p-GaN layer, was inserted in the last three QBs, as shown in Figure. 4.1.

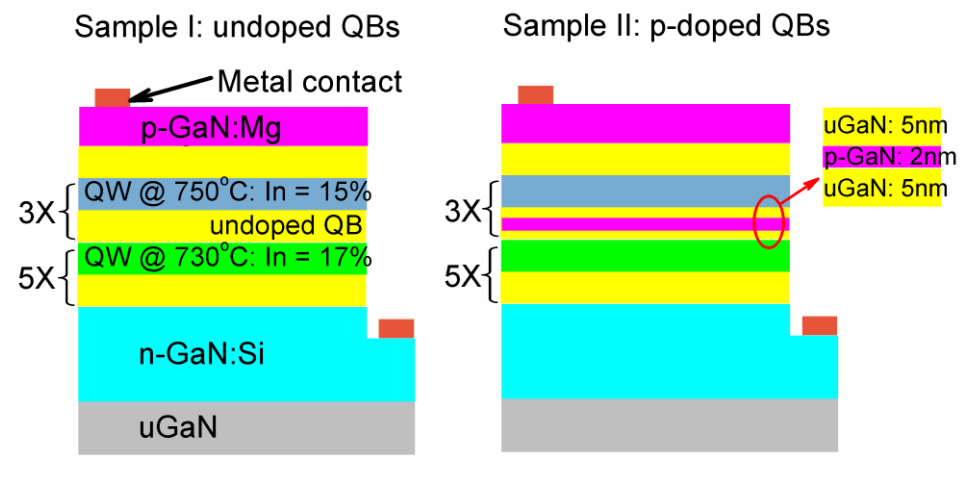

Figure 4.1 Structure diagram of LED samples: (a) Sample I with undoped QBs; and (b) Sample II with three QBs close to p-GaN doped with Mg.

The sample wafers were further fabricated into device chips using a standard LED device fabrication process. Nickel/gold bilayer, with a film thickness of 5 nm/5 nm, was deposited on top of p-GaN layer and was annealed in oxygen ambient to form ohmic contact with p-GaN. The mesa region, with a emitting device area of 350 ×350

μm^2 and depth of 1μm, was defined using reactive ion etching (RIE). Finally, a Ti/Au layer with a thickness of 30 nm/150 nm was deposited for the contact pad metal.

4.3. Dual-wavelength Emission from Quantum Wells

The photoluminescence (PL) spectra display two distinguishing peaks for both samples, due to different indium incorporation at different QW growth temperatures. The shorter wavelength peak, centered at 423 nm for Sample I and 420 nm for Sample II, originates from the three shallow QWs grown at 750 ℃, which has an estimated indium composition of 15%, while the longer wavelength peak, centered at 460 nm for Sample I and 458 nm for Sample II, is from the deep QWs grown at 730 ℃, and the indium composition is estimated to be 17%. Judging from the narrow full width half maximum (FWHM) of the emission peaks, which is between 12 and 16 nm, the MQW structure was not degraded by the p-doping in the QBs.

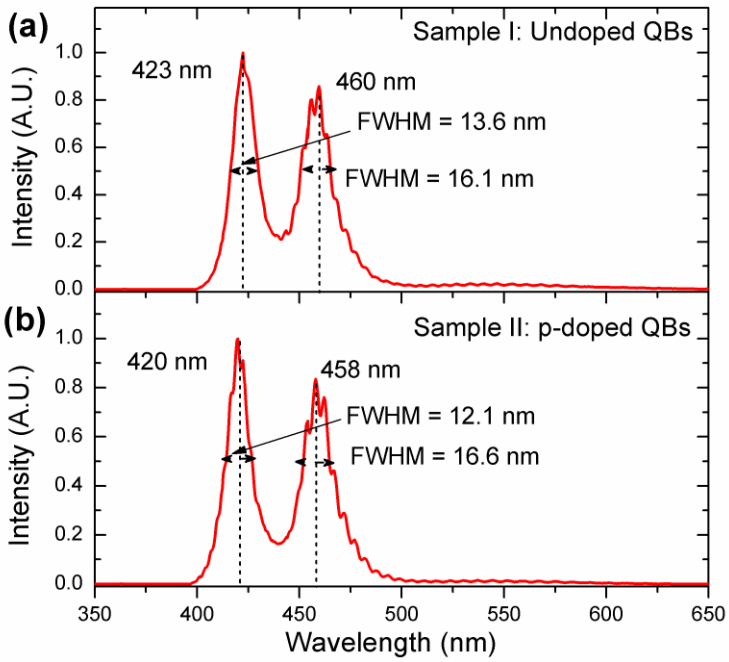

Figure 4.2 Photoluminescence (PL) spectra of LED samples emitting at two wavelength peaks: (a) Sample I with undoped QBs and (b) Sample II with three QBs doped with Mg.

The electroluminescence (EL) spectra for the two samples were captured at different current levels, as shown in Figure. 4.3. For Sample I with undoped QBs, at lower current injection level, the emission at the shorter wavelength of 425 nm is dominated, together with a weak emission peak at 460 nm. This suggests that the radiative recombination of electrons and holes mainly occurs at the QWs near the p-GaN. Only a small portion of holes were able to move into the deep QWs near the n-GaN, which is far from the hole injection source. Hence, there are very limited chances for the electron and hole recombination there, even though the electron concentration is quite high in these quantum wells.

With an injection current above 300 mA, the emission at 425 nm is saturated, whereas the emission peak at 460 nm is substantially increased, and finally exceeds the peak intensity at 425 nm. This indicates that at high injection levels, the hole

concentration in QWs near the p-GaN is close to the saturation limit. With a further increased bias, the radiative recombination of electrons and holes there is saturated. The excessive holes tend to transport into deeper QWs, leading to the rapid increase of light emission at 460 nm.

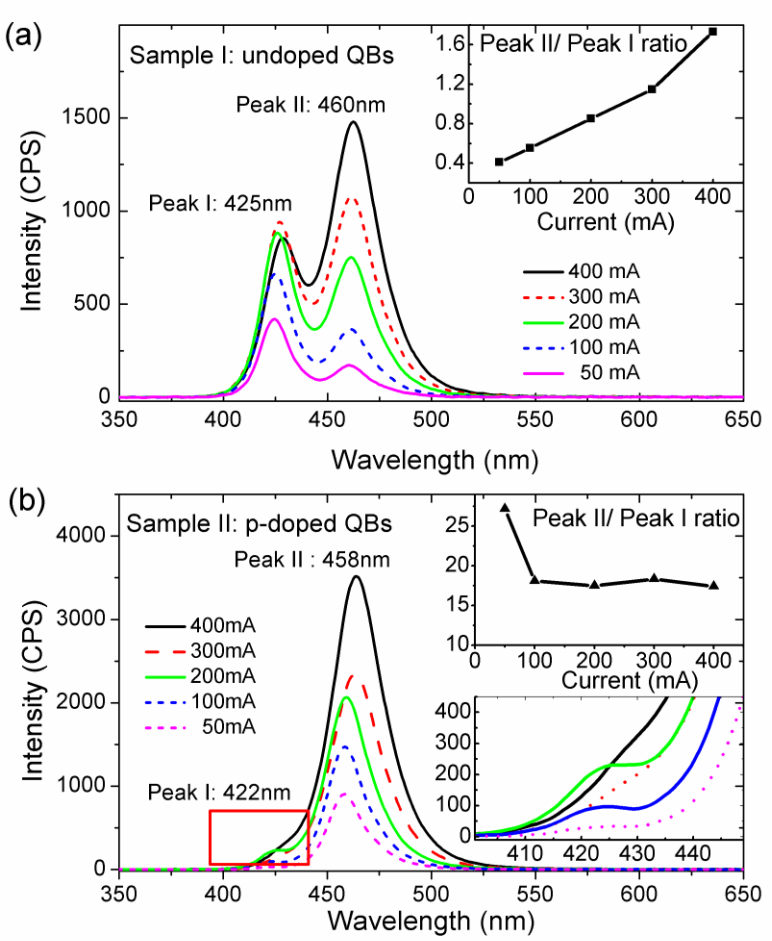

Figure 4.3 Electroluminescence (EL) spectra of LED samples emitting at two wavelength peaks: (a) Sample I with undoped QBs (Inset: Intensity ratio of Peak II/Peak I with increasing current injection) and (b) Sample II with three QBs doped with Mg (Inset: Intensity ratio of Peak II/Peak I with increasing current injection and zoomed-in view of the emission peak at 422 nm).

For the sample with p-type doped QBs, the emission peak at 422 nm, originated from the three shallow quantum wells, is minor compared to the longer wavelength

emission peak from the deeper QWs, as shown in Figure 4.3(b). As the last three QBs are doped with p-type dopant, the hole conductivity is enhanced and makes it easier for holes to penetrate further into the MQW region, even at low injection levels.

4.4. Simulated Carrier Distributions

The devices with the same structure except for the QB doping profile were simulated using APSYS® software. The indium compositions in the five QWs near n-GaN and three QWs near p-GaN were set to 17% and 15%, respectively, corresponding to the different peak emission wavelengths. The Auger recombination coefficient is taken to be 1×10^{42} m^6/s, and 40% of polarization charge was assumed for crystal relaxation. Other parameters used in the simulation can be found in literature [96].

The calculated carrier concentration at 120 A/cm^2 (corresponding to a high current injection level) shows that the structure with the last three QBs doped with Mg has a more uniform hole distribution, while not causing electron concentration decreasing, as illustrated in Figure. 4.4(a). For Sample I with undoped barriers, the hole concentration reduces substantially as holes travel deeper into the QWs. After doping the last three barriers with Mg, the hole concentrations in the deeper QWs are at least one order of magnitude higher, resulting in more chances for the electron-hole recombination to take place in these QWs. Meanwhile, a small amount of decrease in hole concentration in the last two QWs is observed. However, in view of the relatively high hole population in these quantum wells, this small reduction is helpful for avoiding hole crowding.

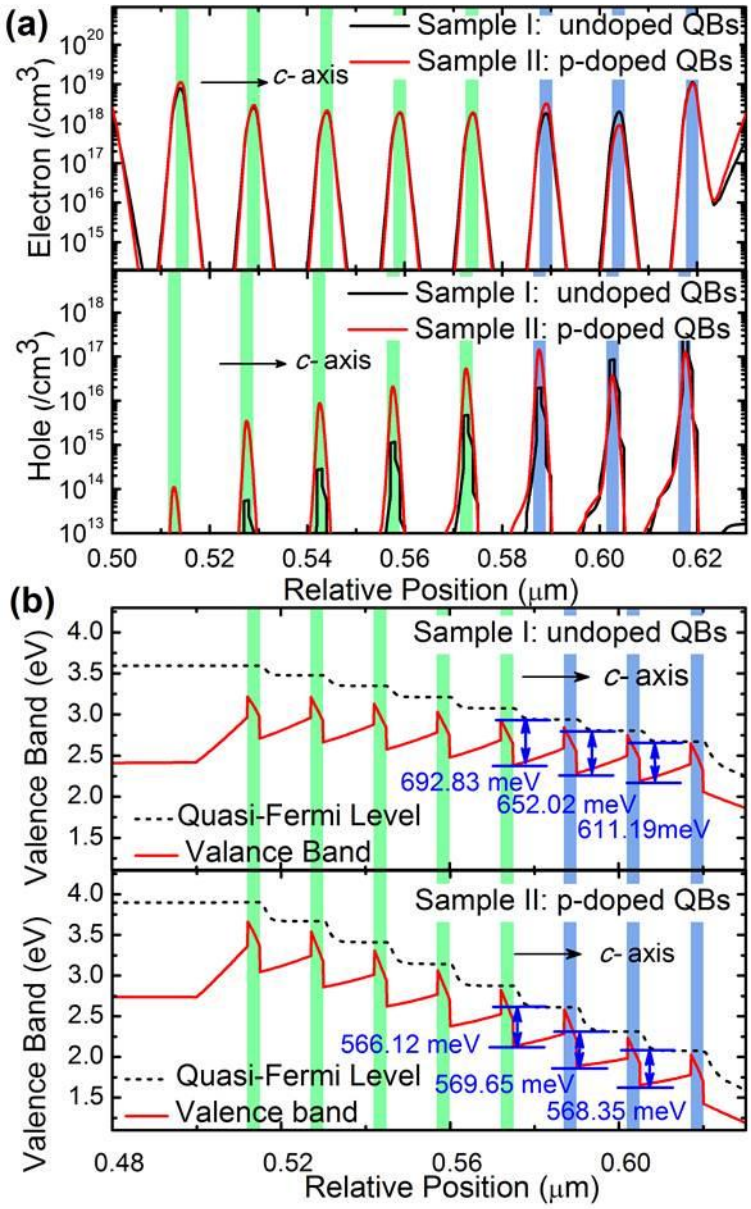

Figure 4.4 (a) Simulated electron and hole distributions within the MQW active region and (b) simulated energy band diagram of LED Sample I and II within the MQW active region.

By analyzing the energy band structure in Figure 4.4(b), it is found that the energy barriers between the quasi-Fermi level and the valance band for the doped barrier are lower (568.35, 569.60 and 566.12 meV), compared to those of the undoped QBs (611.19, 652.02 and 692.83 meV, respectively). This is because the p-type doping

shifts the quasi-Fermi level towards the valance band, bringing down the potential barrier for the holes. Hence the hole conductivity is improved.

Also for the sample with last three QBs p-type doped, the energy barrier for the five undoped barriers are also reduced subsequently. According to the formula $p = n_i \cdot \exp[\frac{E_i - E_{Fpq}}{k_B T}]$ (where p is the hole concentration, n_i is the intrinsic carrier concentration, E_i and E_{Fpq} are the intrinsic Fermi energy level and quasi-Fermi level for holes, respectively, k_B is Boltzmann's constant, and T is the temperature), increased hole concentration will cause the quasi-Fermi level to shift away from the intrinsic Fermi level, or in other words, being closer to the valence band. Therefore, the energy barrier between the Fermi level and valance band for the undoped QBs are also reduced, as shown in the simulation results.

4.5. Comparison of Electrical and Optical Performance

The enhanced hole conductivity is also evidenced by the measured I-V characteristic improvement, as shown in Figure 4.5(a). The forward voltage is reduced for Sample II, thanks to a better hole conductivity by the Mg doping, and hence the increased recombination current within the quantum wells.

Also, the number of the emitted photons, as well as the external quantum efficiency, is observed to be enhanced, as illustrated in Figure 4.5(b). The maximum EQE is increased by 30.9% with the p-doped QBs, while the efficiency droop measured at 350 mA is reduced from 36.71% to 31.62%. The improved optical performance is attributed to better hole transport.

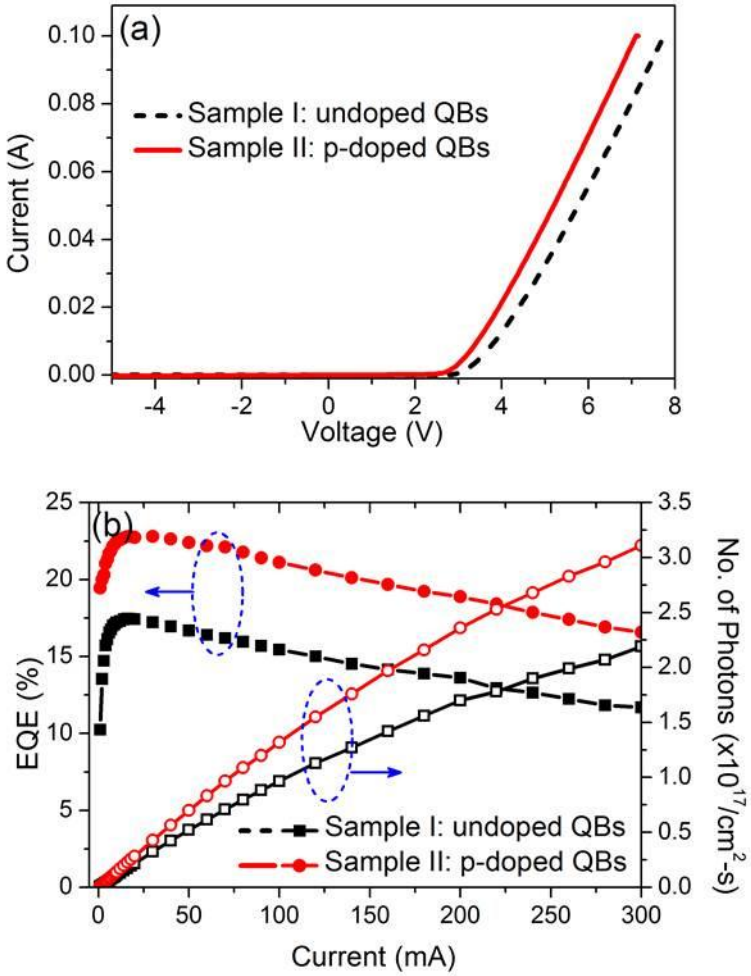

Figure 4.5 Experimentally measured (a) I-V characteristics and (b) external quantum efficiency (EQE) and number of emitted photons for LED Sample I and II.

4.6. Conclusion

In conclusion, the hole transporting behavior of a partially p-doped QB LED structure was studied through dual-peak emission technique. Hole conductivity was enhanced by the Mg dopant in the QB, leading to a more uniform distribution of holes. Meanwhile, the hole crowding in the QWs close to the p-GaN is avoided. The improved hole conductivity is attributed to the reduced energy barrier by the p-dopant. The additional p-doping in the barriers results in improved electrical and optical

performance of the LED device. Such p-type doping of QBs holds great promise for LED performance enhancement.

Chapter 5. Influence of n-Type and p-Type Electron Blocking Layers

The effect of p-AlGaN and n-AlGaN electron blocking layers on the performance of GaN based blue light emitting diodes is studied in this chapter. Experimental results suggest that the n-type electron blocking layer leads to higher optical output power and external quantum efficiency, compared to devices with p-type AlGaN blocking layer. Theoretical simulations of the carrier distribution and energy band diagram reveal that the n-AlGaN electron blocking layer is more efficient in preventing electron overflow, while not blocking hole injection into the multiple quantum well active region. Hence it enables a higher radiative recombination rate within the quantum wells and results in higher photon generation. This chapter is partially based on "Influence of n-type versus p-type AlGaN electron-blocking layer on InGaN-GaN multiple quantum wells light-emitting diodes" published on *Applied Physics Letters*.

5.1. Introduction

Tremendous work has been devoted to improving the performance of InGaN/GaN LEDs through addressing various technical challenges [20, 81]. Optical output power and external quantum efficiency (EQE) are the most critical parameters that need to be further improved for high power LEDs to penetrate into the mass market of general lighting [97, 98]. The limiting factors for the improvement of EQE include electron

overflow into p-GaN region and insufficient hole supply into the active region. p-Type electron blocking layer (EBL) is widely adopted to prevent the electron overflow. By inserting a p-type doped AlGaN EBL between the multiple quantum wells (MQWs) and the p-GaN layer, the electrons are confined within the MQWs because of the potential barrier created by large bandgap AlGaN, resulting in less electron overflow. Various p-type EBL structures have been proposed, including p-InGaN/AlGaN EBL [99], AlGaN/GaN/AlGaN EBL [100], and staircase AlGaN EBL [43]. Although the p-type AlGaN EBL is able to reduce the electron overflow, its large potential barrier height also hinders the transport of holes into the MQWs region, which causes insufficient supply of holes taking part in the radiative recombination with electrons [36, 44]. Therefore, a novel EBL structure superior to the p-type AlGaN EBL is needed, which should be effective in both preventing the electron overflow and avoiding generating difficulty for the hole transport into the MQWs region. An n-type doped EBL structure has been theoretically proposed to achieve better carrier transport and enhanced optical performance [101]. However, no experimental demonstration on the improvement of device performance realized by the n-EBL has been reported to date.

In this part, an n-type doped AlGaN EBL is designed and demonstrated in blue InGaN/GaN LEDs. The optical power performance of InGaN/GaN LEDs with the n-type doped AlGaN EBL, p-type doped AlGaN EBL, and n-AlGaN & p-AlGaN EBLs structures is comparatively studied. Theoretical simulation is also conducted to reveal the effects of various types of EBLs on the electron blocking, hole distribution, energy band diagram, and radiative recombination rates in each individual QW. The simulations results provide an insightful understanding on the role of n-AlGaN EBL and the performance enhancement of high power InGaN/GaN LEDs.

5.2. Epitaxial Growth and Device Fabrication

Four InGaN/GaN LED samples were grown on *c*-plane sapphire substrate using metal-organic chemical vapor deposition (MOCVD) system, with the device structures shown in the insets of Figure 5.1. Sample I consists of 5 μm thick unintentionally doped GaN, 3 μm thick n-doped GaN (doping concentration ≈ $5\times10^{18}/cm^3$), five pairs of QWs, and 200 nm thick p-doped GaN (doping concentration ≈ $3\times10^{17}/cm^3$). For Sample II, a 12 nm thick p-type doped AlGaN EBL was inserted between the MQWs and p-GaN. And for Sample III, a 12 nm thick n-type doped AlGaN EBL was inserted between the n-GaN and MQWs. Sample IV involved both n-type and p-type AlGaN EBLs. The aluminum content in the EBLs was 15%, and the doping concentrations were the same as that in the n-GaN and p-GaN layers.

After the epitaxial growth, the four samples were further fabricated into device chips with mesa areas of 350 × 350 μm^2. Annealed Ni/Au with thickness of 5 nm / 5 nm was used as a transparent current spreading layer. And Ti/Au (30 nm / 150 nm) metal bilayer was deposited for both p-contact and n-contact pads. The electroluminescence (EL) spectra and the optical power of all fabricated devices were measured using an integrating sphere.

5.3. Comparison of Optical and Electrical Performance of LED Devices

All the LED devices emit blue light with an emission peak at 435 nm, as shown in Figure 5.1. From the EL spectra, it can be found that Sample III with the n-AlGaN EBL has the highest emission intensity under all current injection levels. The

emission intensity of Sample IV with both the n-AlGaN EBL and p-AlGaN EBL is lower than Sample III, but higher than that of Sample II. Sample I with no EBL structure exhibits the lowest emission intensity.

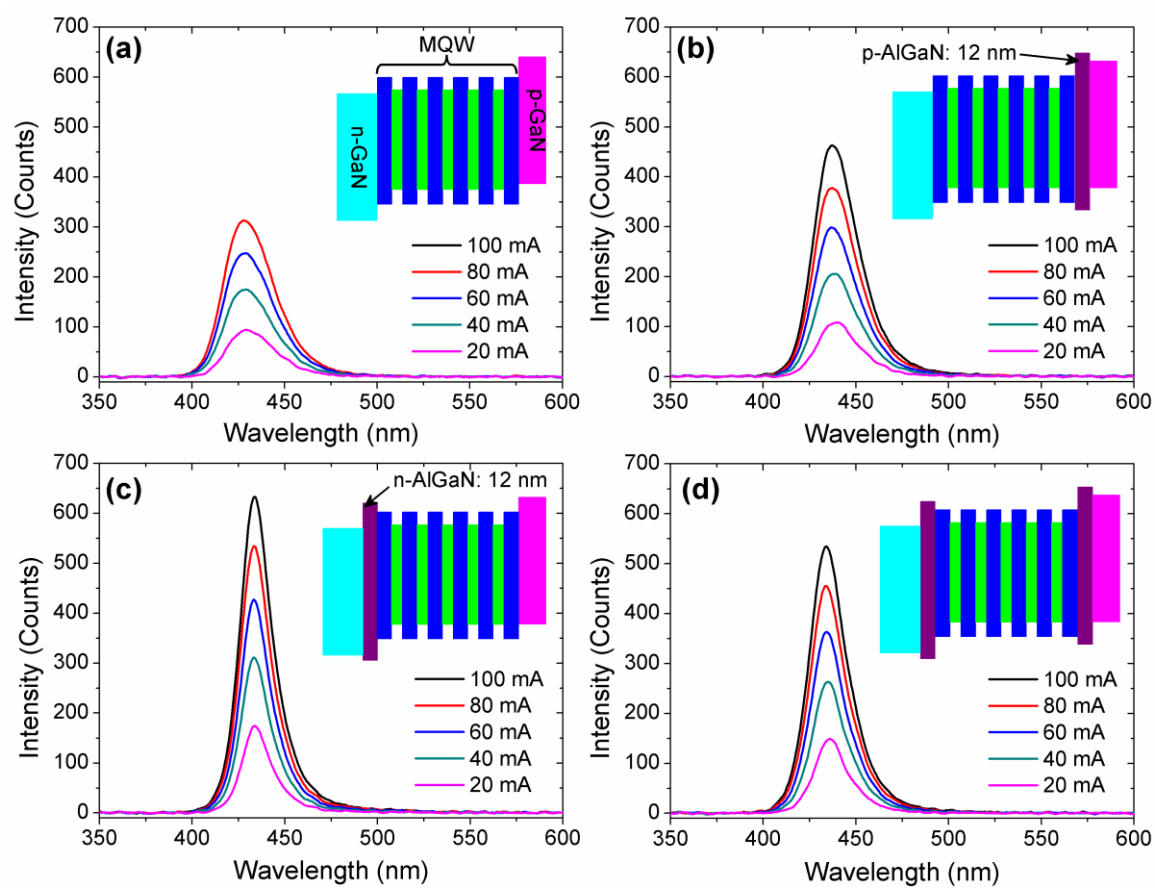

Figure 5.1 Schematic diagram and electroluminescence (EL) spectra of GaN LED devices with (a) no AlGaN EBL; (b) p-AlGaN EBL; (c) n-AlGaN EBL; and (d) both n-AlGaN and p-AlGaN EBLs.

Figure 5.2 shows the current dependence of the optical output power, and the EQE extracted accordingly, for the four LED samples. It can be clearly seen that devices with electron blocking layers (Sample II, III and IV) demonstrates superior optical power emission and EQE throughout the whole current range measured, compared to Sample I without any EBL structure. At 150 mA, the optical power of Sample I is

23.1 mW, while those of Sample II, Sample III, and Sample IV are 29.9, 33.9, and 31.7 mW, respectively. This implies that the EBL structures function and suppress the electron overflow into the p-GaN region, improving the optical performance of LED devices.

Among the three samples with EBLs, Sample III exhibits the strongest optical power, in agreement with the EL spectra intensity. At 150 mA, the optical power of Sample III, as well as the EQE, is 13.7% and 6.9% higher than those of Sample II and Sample IV, respectively. The further improvement of the optical output power and EQE of Sample III, in comparison with Sample II and Sample IV, could be due to the different electron blocking layers used in these device structures.

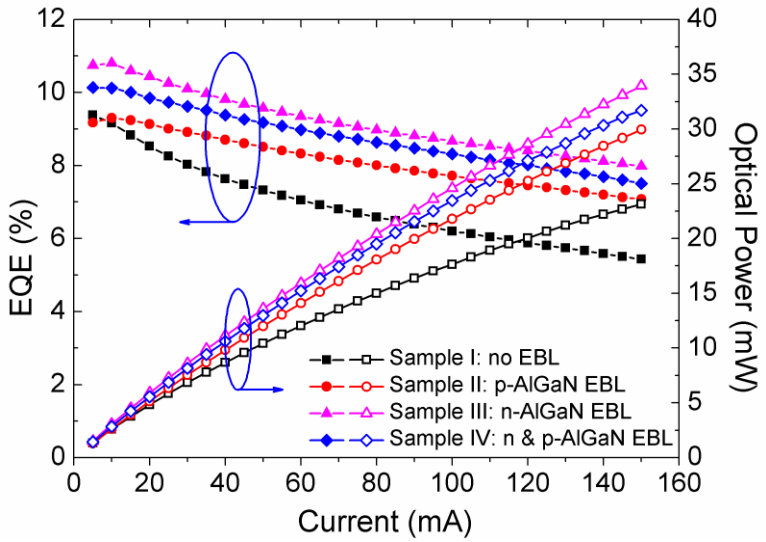

Figure 5.2 Optical power and external quantum efficiency (EQE) measured for LED samples with different electron blocking layer structures.

The I-V characteristics of Sample I - IV are measured and shown in Figure 5.3. All the samples with an electron blocking structure (Sample II, Sample III and Sample IV) present lower forward voltage than Sample I without EBL. The reduction of

forward voltage is attributed to the enhanced lateral current spreading effect, due to the potential barrier created by the large bandgap AlGaN layer(s). However, no obvious difference is observed between the devices with different EBL structures, indicating that with proper thickness and doping profile, the electron blocking layer will not degrade the device's electrical performance.

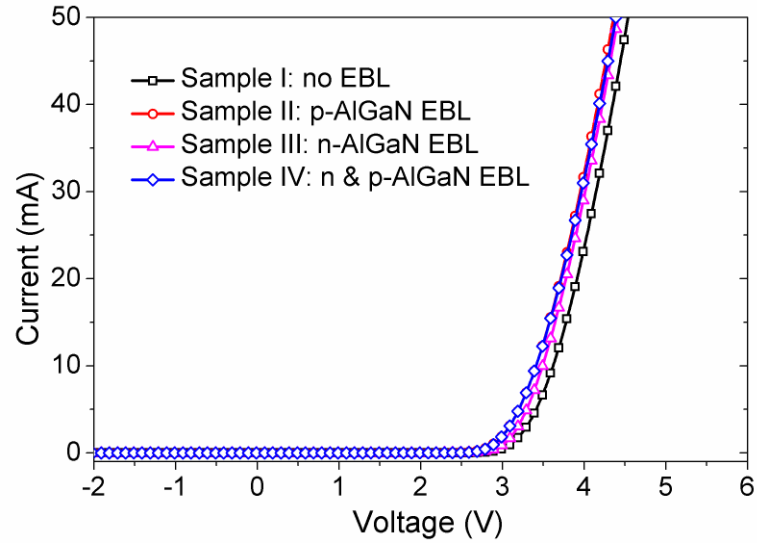

Figure 5.3 Experimentally measured I-V characteristics for LED devices with different EBL structures.

5.4. Numerical Analyses of Devices with Different Electron Blocking Layer Structures

In order to understand the underlying physics behind the optical performance improvement, theoretical simulations have been performed to reveal the influences of different EBLs on the carrier transport, energy band, and radiative recombination rate in the MQWs. In the numerical simulations, the Poisson equation, continuity equation and Schrödinger equation with proper boundary conditions are self-consistently solved using the APSYS software. The self-consistent six-band $k\,p$ theory is used to

take into account the carrier screening effect in the InGaN QWs [102]. The Auger recombination coefficient is taken to be 1x 10^{-30} cm^6s^{-1} [103]. The Shockley-Read-Hall (SRH) lifetime for electron and hole is set to be 43 ns [103]. Meanwhile, a 40% of the theoretical polarization induced sheet charge density is assumed due to the crystal relaxation through dislocation generation during the growth. The energy band offset ratio of $\Delta E_C/\Delta E_V$ = 70/30 is set in the InGaN/GaN QW regions. The other parameters used in the simulation can be found in literature [96, 104].

The electron concentration distribution profiles within the MQWs active region, under a current density of 120 A/cm^2 (equivalent to 150 mA for a 350 × 350 μm^2 device area) are shown in Figure 5.4(a). For the device with p-AlGaN EBL, the electron concentration is not uniformly distributed and much higher in the first and last QWs. While for the device with n-AlGaN EBL, the electron concentration is much more uniform and less electron crowding is observed in the first and last QWs. However, when both n-EBL and p-EBL are involved, the device exhibits better electron concentration uniformity in the first four QWs near the n-GaN region, but a severe electron accumulation in the last QW near the p-GaN. Figure 5.4(b) shows the hole distributions in the device structures with different EBLs. It can be clearly seen that for the device with n-EBL, the hole concentration in each individual QW is the highest and most uniform, compared to the devices with p-EBL or both p-EBL & n-EBL. Figure 5.4(c) illustrates the electron concentration in the p-GaN region for the three devices with EBL structures. The n-EBL device has the lowest electron concentration, meaning the electron overflow into the p-GaN layer. Hence the electron blocking effect of the n-AlGaN EBL is more efficient than the other EBL structures.

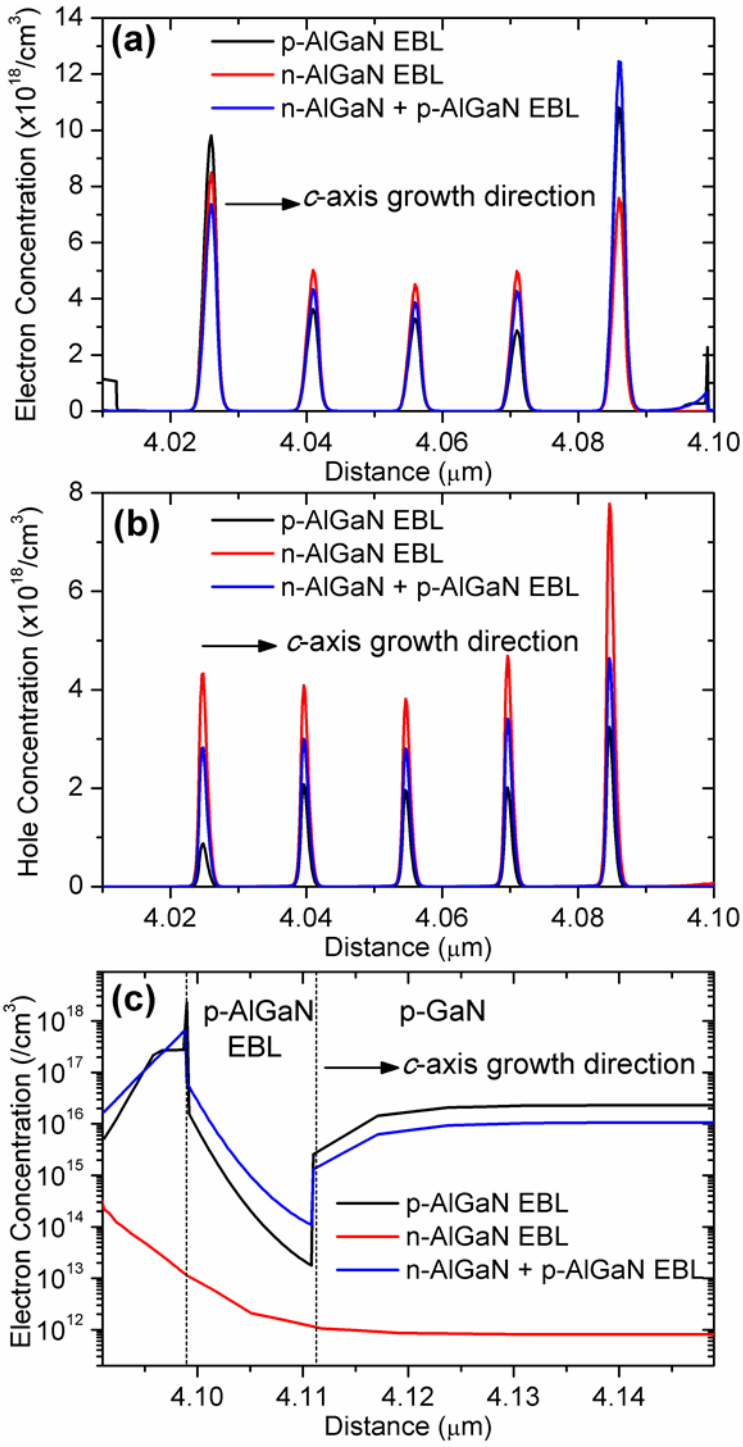

Figure 5.4 Simulated (a) electron concentration; (b) hole concentration; and (c) electron overflow into p-GaN region for the LED devices with different EBL structures under 120 A/cm^2 current injection.

The simulated energy band diagrams for the LED devices with different EBLs are shown in Figures 5.5(a)-(c). The energy band shows that the carriers are confined within the MQWs active region by the energy barriers created by the AlGaN layers, which have a larger band gap. The p-type EBL, as shown in Figure 5.5(a), creates a potential energy barrier for electrons, and hence is able to confine the electrons within the last QW. However, it also generates an energy barrier height of 169.4 meV for holes. In contrast, in the n-EBL LED, as shown in Figure 5.5(b), the n-AlGaN layer builds up an energy barrier of 90 meV height for electrons before they enter the MQWs active region. Meanwhile, there is no energy barrier for hole transport into the QWs, since no AlGaN EBL is present on the hole transport path. When both n-AlGaN and p-AlGaN EBLs are involved, we see barriers for both electrons and holes, with barrier heights of 77.5 and 168.6 meV, respectively, sandwiching the MQWs region, as illustrated in Figure 5.5(c).

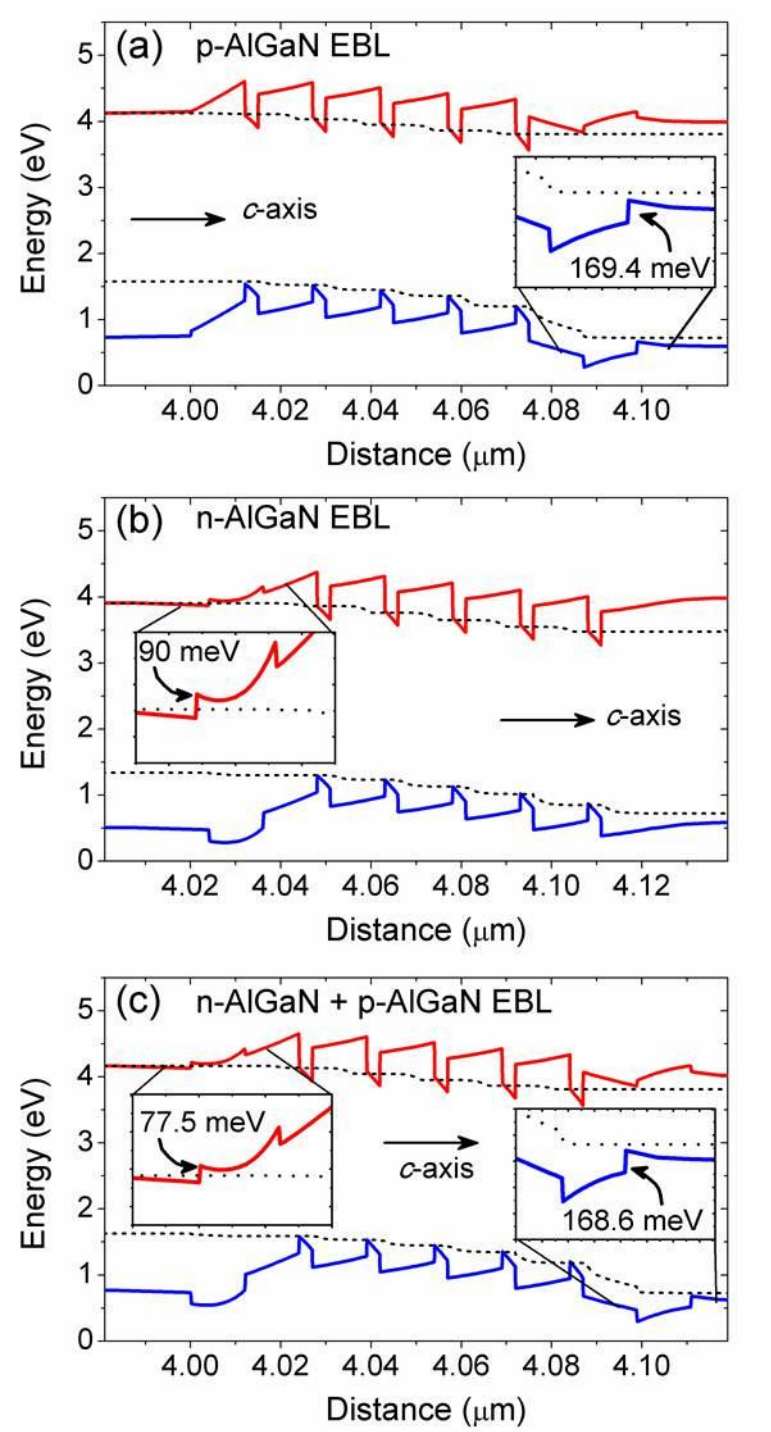

Figure 5.5 Simulated energy band diagram for the LED devices with (a) p-AlGaN EBL; (b) n-AlGaN EBL; and (c) both n-AlGaN and p-AlGaN EBLs under 120 A/cm^2 current injection.

The simulated radiative recombination rates within the MQWs for the LED devices are shown in Figure 5.6. The radiative recombination rate within each individual QW of the n-EBL device is much higher and more uniform than the other two devices. The highest radiative recombination rate occurs in the QW closest to the p-GaN layer, owning to the high hole concentration in this QW. This property of radiative recombination rate of the device with n-EBL, in comparison with the p-EBL device and p&n-EBL device, is a consequence of the higher and more uniform electron and hole concentrations within the MQW region.

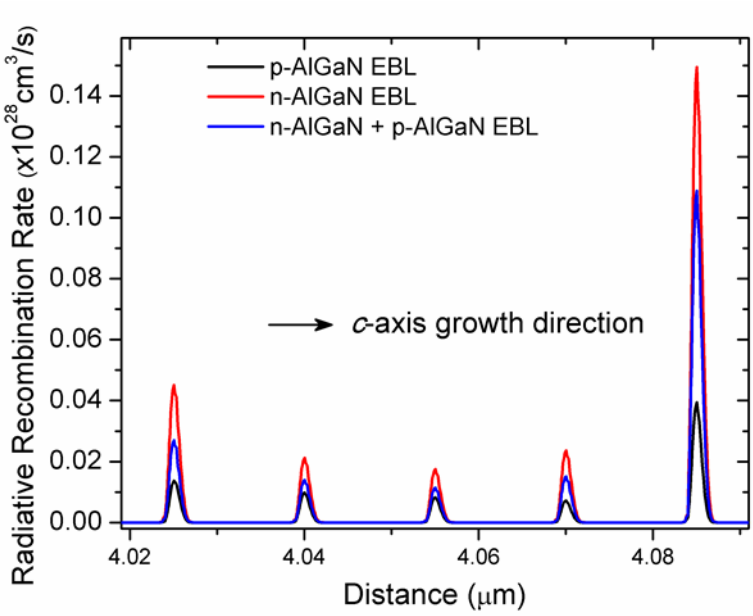

Figure 5.6 Simulated radiative recombination rate within MQWs active region for the LED devices with different EBL structures.

Based on the experimental and simulation results above, it is understandable that the n-type EBL is more effective in reducing electron overflow and homogenizing both electron and hole distribution and thus leads to higher radiative recombination rate in the MQWs than the p-type EBL and the p&n-type EBLs. For Sample II with the typical p-EBL, the electron concentration in the first QW is higher due to the

proximity to the electron injection layer, while the electron concentration in the last QW close to p-AlGaN EBL is also higher as a result of the blocking effect of the high potential barrier of p-AlGaN EBL. The electron crowding in the first and the last QWs could enhance the non-radiative Auger recombination. Meanwhile, the p-AlGaN EBL creates a large potential barrier for holes, making holes transporting into MQW region more difficult and leading to very severe decay in hole concentration in the region deeper into the active layer. The combination of the non-uniform distribution of electrons and holes and the enhanced Auger recombination due to the electron crowding leads to the smaller and non-uniform distribution of radiative recombination rate in the MQWs for Sample II with p-EBL. On the contrary, for Sample III with n-EBL, the large potential barrier of n-AlGaN mitigates the electron concentration in the first QW, and also there is no large potential barrier blocking the electrons in the last QW near the p-GaN region unlike the case of Sample II with p-AlGaN EBL. Thus the electron crowding is insignificant and Auger recombination is largely suppressed. The electron distribution is more uniform across the whole MQWs region. Moreover, the absence of p-EBL allows holes to transport deeper into the active region, resulting in a more uniform hole distribution in each individual QW. The concentrations of electrons and holes in each individual QW are well balanced and matched in Sample III. Therefore, the radiative recombination rate in Sample III is much stronger and more uniform than that in Sample II. This explains the superior optical performance of Sample III compared to that of Sample II. However, after adding p-EBL structure into the device with n-EBL as the case of Sample IV, although the electron concentration in the first QW is further reduced, the electron concentration in the last QW becomes much larger due to the large potential barrier of p-AlGaN. At the same time, the hole transport is difficult because of the added p-AlGaN EBL, and the hole

concentration in MQWs is smaller than that of Sample III. Therefore, the radiative recombination rate of Sample IV is reduced compared to that of Sample III. That is why when both the n-EBL and p-EBL are adopted in Sample IV, the device performance is degraded instead of being improved.

5.5. Conclusion

In conclusion, the influence of n-type and p-type AlGaN electron blocking layers is comparatively studied. Both experimental and simulation results reveal that the n-AlGaN EBL is more efficient in blocking excess electrons, while not blocking hole injection into the active region. The enhanced hole concentration and the uniform carrier distribution within MQW region result in higher radiative recombination rate and improved light conversion efficiency. Hence, the n-AlGaN EBL is more suitable to improve the device performance of high power InGaN/GaN light-emitting diodes.

Chapter 6. Emission Kinetics in Polar vs. Semipolar GaN Light-Emitting Diodes

In this chapter, the carrier dynamics within multiple quantum well structures grown on (0001) polar plane and (11-22) semipolar plane are comparatively investigated using electroluminescence and photoluminescence spectroscopy. The study aims to reveal the influence of polarization field of different growth planes on the performance of multiple quantum well LEDs.

6.1. Introduction

So far, most of the research work on GaN LEDs focuses on the epitaxial structures grown on (0001) *c*-plane sapphire substrate, where the polarization axis is perpendicular to the growth plane. Therefore, the multiple quantum wells (MQW) structure grown on this orientation suffers from spontaneous and piezoelectric polarization fields. The combinational polarization field tilts the energy bands of the QWs, and hence spatially separates the electron and hole wave functions, which is known as quantum-confined Stark effect (QCSE). As a result, the radiative recombination rate within the MQWs is reduced, leading to limited efficiency of the LED device. Also, the electroluminescence emission experiences peak wavelength shift under high current injection. To eliminate the negative influence by the polarization fields, staggered $In_xGa_{1-x}N/In_yGa_{1-y}N$ QW structures have been proposed to increase the overlapping of the electron and hole wave functions [105]. Another

approach is to growth of LED epitaxial structure on the nonpolar and semipolar planes has been proposed to release the QCSE [106-110]. Those devices exhibit a more stable EL emission and higher efficiency over those grown on *c*-plane substrates. However, the mechanism of carrier movement and recombination under different strength and direction of the polarization fields has not been systematically reported yet.

In this study, LED samples were grown on polar and semipolar plane substrates and fabricated into standard device chips. The peak emission wavelength and full-width at half maximum (FWHM) were extracted from electroluminescence measurement, showing that the semipolar LED has a more stable EL emission performance. The polar LED has an obviously longer carrier lifetime as compared to that of the semipolar LED device. Under positive external voltage bias, the PL emission peak of the polar LED is red-shifted, and the carrier lifetime is prolonged. In contrast, the semipolar LED device displays a blue shift trend of PL emission peak under positive voltage bias, and the lifetime variation is less sensitive to the bias condition. The performance differences are attributed to the different polarization field corresponding to the growth planes.

6.2. Growth and Fabrication of Polar/Semipolar GaN LEDs

The InGaN/GaN multiple quantum wells LED samples were grown using MOCVD system. The polar GaN LED sample was grown on (0001) *c*-plane sapphire substrate, while the semipolar LED sample was grown on (11-22) *r*-plane GaN substrate. Both structures consists of a 30 nm thick low temperature buffer layer, a 4 μm thick unintentionally doped bulk GaN layer, a 2 μm thick Si-doped n-GaN layer, five pairs of InGaN/GaN QWs, with QW and QB thickness of 3 nm and 12 nm,

respectively, and finally a 200 nm thick Mg-doped p-GaN layer. The doping concentrations of the n-GaN and p-GaN layers were $5\times10^{18}/cm^3$ and $3\times10^{17}/cm^3$, respectively.

After the growth, the epi-wafers were further fabricated into chips using standard fabrication process. Ni/Au layer with 5 nm/5 nm thickness was deposited and annealed in oxygen ambient to serve as transparent current spreading layer and to form ohmic contact with the p-GaN layer. Mesa areas of $350 \times 350\ \mu m^2$ were defined using reactive ion etching (RIE) to expose the n-GaN layer. Finally, Ti/Au bilayer with a thickness of 30/150 nm was deposited as metal contact pad to both n-GaN and p-GaN.

The EL measurement was performed using a LED tester (Quatek M2442S-9A). To exclude the thermal effect, a pulsed current source with pulse duration of 5 ms and repetition frequency of 20 Hz (duty-cycle 10%) was used. The micro photoluminescence (μ-PL) measurements were performed at room temperature and a He-Cd laser operates at 325 nm was used as the excitation source. The emission was collected by an objective and focused into an optical fiber and directed into a 750 mm monochromator combined with a photomultiplier tube (Hamamatsu R928) for spectral recording. For the time-resolved PL (TRPL), the excitation source was replaced by a pulsed Nd:YAG 4th harmonic (266 nm) laser with pulse width and repetition rate of 1 ns and 60 Hz, respectively. The detector output was stored on a digital phosphor oscilloscope (Tektronix DPO 7254) and averaged over 500 periods to improve the signal-to-noise ratio. The optical absorption spectra were recorded by employing our photocurrent setup accompanying a xenon lamp, a monochromator, a chopper, a lock-in amplifier, a power meter, and a DC power supply [111, 112].

6.3. Comparison of Device Performance

The current-dependent emission peak wavelength and full width at half maximum (FWHM) of both polar and semipolar samples are shown in Figure 6.1. As the current increases, the emission peak wavelength of the polar LED device is blue-shifted from 438.9 to 433.8 nm. The blue shift is attributed to the carrier-induced screening of the QCSE by the injected electrons and holes [113, 114]. For the semipolar LED sample, the emission peak wavelength exhibits a smaller blue-shift, from 434.6 to 433 nm, with increasing current from 5 to 50 mA. However, as the driving current is higher than 50 mA, no obvious shifting can be observed. Compared the polar LED device, the semipolar LED device demonstrates a more stable EL emission. Meanwhile, the semipolar LED sample presents smaller broadening of FWHM than the polar LED sample with increasing current injection.

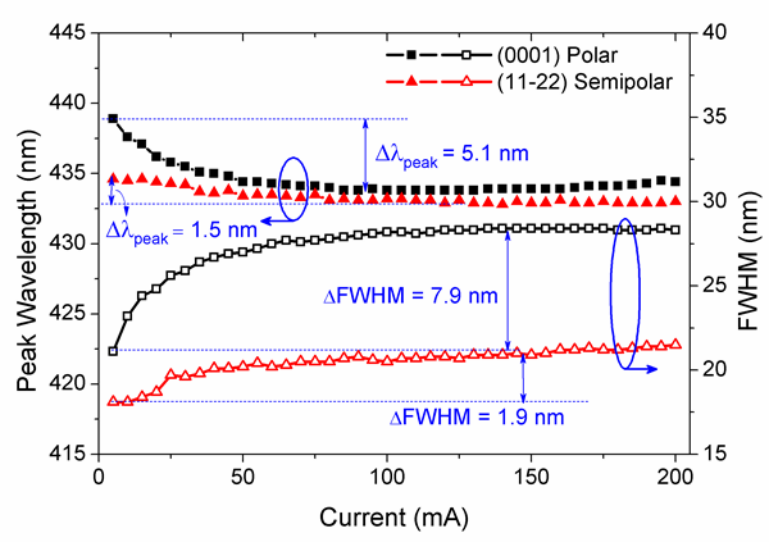

Figure 6.1 Current dependence of electroluminescence emission peak wavelength and full width half maximum (FWHM) for the polar and semipolar GaN LED devices.

The PL spectra of the polar and semipolar LED samples were captured with external voltage bias applied to the devices, as demonstrated in Figures 6.2(a) and 6.2(b). It is noted that the two samples display opposite shift trends under external bias. In Figure 6.2(a), the PL spectra of the polar LED sample show an obvious blue-shift when negative biases from 0 V to -2 V are applied to the device. And when positive voltage bias is applied, increasing from 0 V to +2 V, the PL spectra is red-shifted correspondingly. In contrast, for the semipolar LED device, the PL spectra displays a small red-shift with increasing external bias from 0 to -2 V, and blue-shift when the bias varies from 0 to +2 V.

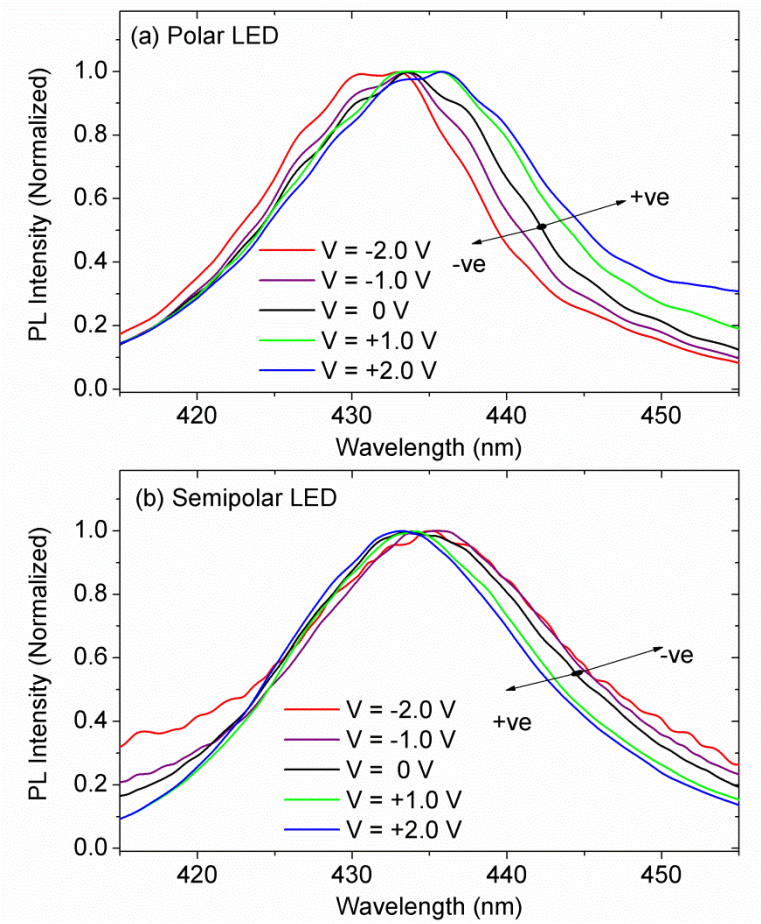

Figure 6.2 Filed-dependent photoluminescence spectra of (a) polar LED device and (b) semipolar LED device under external bias from -2 to +2 V.

The time-resolved photoluminescence (TRPL) spectra for both the polar and the semipolar LED devices are shown in Figures 6.3(a) and 6.3(b). The bias-dependent carrier lifetimes of both devices are extracted from the TRPL spectra and plotted in the insets. It is obvious that the polar LED device exhibits longer carrier lifetime than the semipolar LED device. When there is no bias applied to the device, the polar LED has a lifetime of 14.9 ns, about three times of that of the semipolar LED device, which is 5.5 ns. The polar LED device shows a prolonged decay process under positive external bias (0 to +2 V), and an accelerated decay when the bias is changed to negative voltages (0 to -2 V). The observed variation trend of the carrier lifetime is consistent with earlier studies reported [115, 116]. The carrier lifetime reaches to the minimum value of 10.0 ns under a negative bias of -15 V, indicating the fastest carrier decay process under this bias condition. As the negative external bias is further increased, the decay is slowed down, as reflected by the increasing of the carrier lifetime. The TRPL spectra of the semipolar LED device show a similar shifting trend under varying external bias condition, as presented in Figure 6.3(b). The shorter carrier lifetime at all bias voltage levels suggests higher recombination rates and consequently higher internal quantum efficiency. Besides, the semipolar LED device reaches the fastest decay time at smaller negative bias voltage value of -1.5 V.

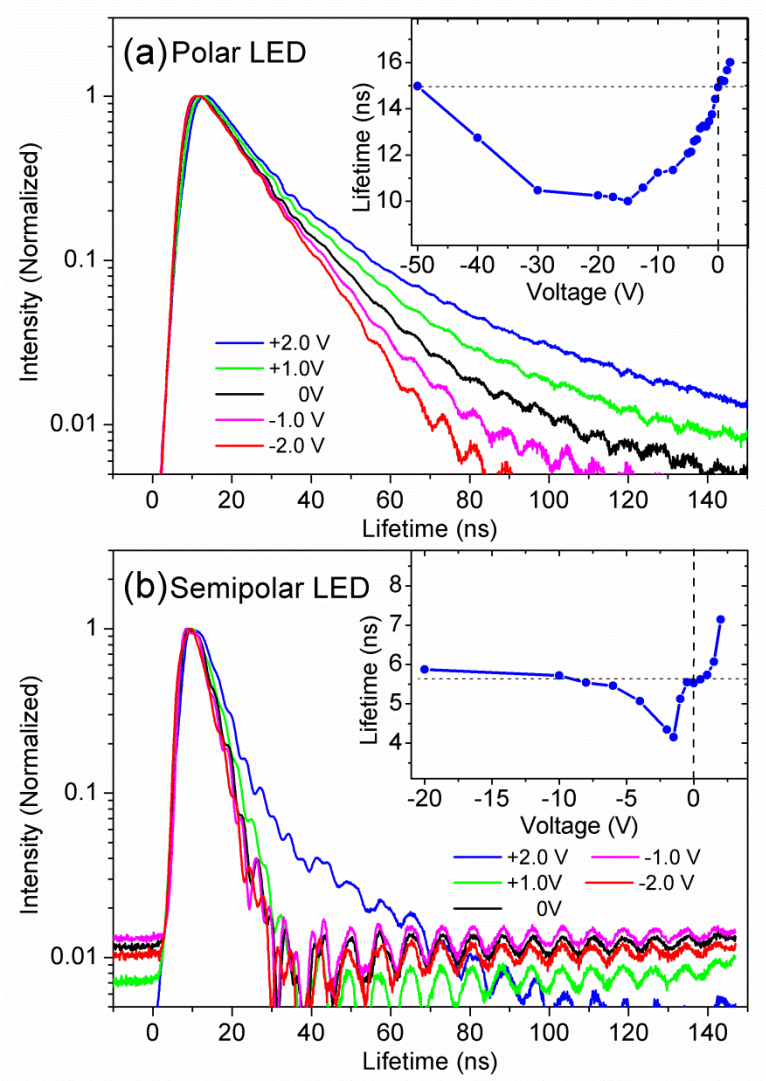

Figure 6.3 Time-resolved photoluminescence (TRPL) spectra of (a) polar LED device and (b) semipolar LED device under external bias from -2 to +2 V. Inset shows the carrier lifetime (extracted using exponential fitting) for (a) polar LED device under external bias from -50 to +2 V and (b) semipolar LED device under external bias from -20 to +2 V.

The setup for the electroabsorption involves a xenon lamp, a monochromator, a chopper, a lock-in amplifier, a power meter, and a DC power supply. The DC power supply is connected to the LED device chip to provide various voltage biases from -2 to +2 V. The white light generated by the xenon lamp is filtered by the

monochrometer and incident to the chip. The power of the incident light beam is read as $P_{indicent.}$ Photocurrent corresponding to wavelength, from 400 to 470 nm, is recorded by the power meter and hence the absorbed power $P_{absorbed}$ can be calculated:

$$P_{absorbed} = \frac{I}{e} \cdot \frac{hc}{\lambda} \tag{6.1}$$

where I is the photocurrent corresponding to the wavelength λ of the incident light. h, c, and e are the Planck's Constant, speed of light in vacuum, and element electron charge, respectively.

The portion of absorbed power and incident power can be represented as follow:

$$\frac{P_{absorbed}}{P_{incident}} = (1 - e^{-\alpha d}) \frac{(1-n)^2}{(1+n)^2} \tag{6.2}$$

where α is the absorption coefficient, d is the quantum well thickness and n is the refractive coefficient of the GaN material. Hence, the absorption coefficient can be calculated as:

$$\alpha = -\frac{1}{d} \ln\left[1 - \frac{Ihc}{e\lambda P_{incident}} \cdot \frac{(1+n)^2}{(1-n)^2}\right] \tag{6.3}$$

The electroabsorption coefficient spectra for both the polar and the semipolar LED devices are illustrated in Figures 6.4(a) and 6.4(b). And the absorption coefficient changes, compared with zero-bias condition, are shown in the insets of the figures. The polar LED device presents a reduced absorption at shorter wavelengths (λ < 425 nm) and slightly enhanced absorption at longer wavelength region (λ > 425 nm) when biased with positive voltages, as shown in Figure 6.4(a). And under negative bias voltages of -1 and -2 V, the absorption coefficient at short wavelengths is increased and at longer wavelengths is decreased. While for the semipolar LED device under negative bias, the absorption at shorter wavelengths is decreased and at

longer wavelengths is increased, opposite to the trend observed for the polar LED device.

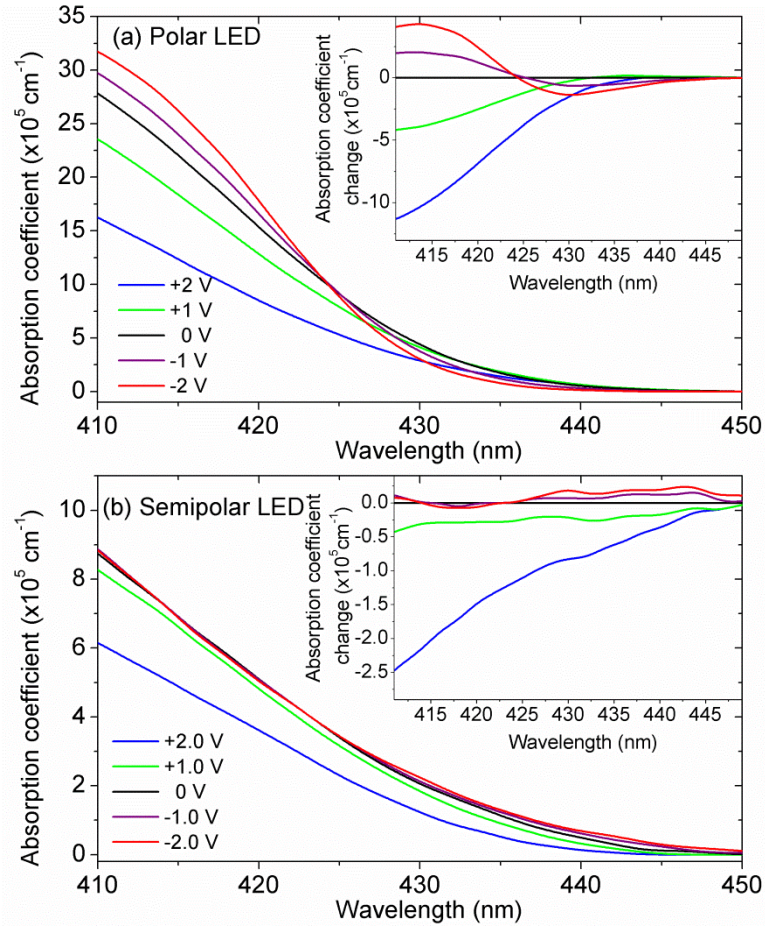

Figure 6.4 Electroabsorption spectra of (a) the polar LED device and (b) the semipolar LED device under external voltage bias from -2.0 to +2.0 V. Inset: the absorption coefficient change compared to the zero bias condition.

The schematic energy band diagram in the InGaN/GaN quantum well is presented in Figure 6.5 for both the polar and the semipolar LED devices. When there is no external bias connected to the device (V = 0), the QW of the polar LED device experiences polarization induced electrical filed, which is in the same direction of the [0001] growth orientation. Hence, the energy band within the QW is tilted by the

internal electric field. Under positive voltage bias (V>0), the external electric field is in the same direction with the internal electric field, leading to further tilting of the energy band of within the QW. As a result, the effective band gap is reduced, as reflected in the red-shift of the PL spectra in Figure 6.2(a). Meanwhile, the tilting of the energy band causes further separation of the electron and hole wave functions, resulting less chances for the electrons and holes recombination. Therefore, the carrier lifetime is longer as compared to the zero bias condition. Moreover, the external electrical field introduces carriers into the QW and hence is able to screen the QCSE, so that the reduced absorption coefficient at short wavelengths and enhanced absorption at longer wavelengths is expected. In contrast, when the polar LED is biased with negative voltages (V<0), the external electric field is in opposite direction with the internal electric field, making the energy band to be less tilted. Consequently, the effective energy band gap is larger, and the overlapping between the electron and hole wavefunction is higher (more chances for carrier recombination), as reflected in the blue-shift of the PL spectra and the reduced carrier lifetime. At certain value of bias voltage, e.g., -15 V in this case, the external electric field is strong is enough to fully offset the influence of the polarization field, leading to a flat energy band in the QW. Hence, the overlapping between the carrier wave functions reaches the maximum and the minimum carrier lifetime is obtained. Consequently, the strength of the internal polarization electric field ($\xi_{internal}$) can be estimated through

$$\xi_{internal} = \frac{V_{bias}}{d} \ ,$$

Where V_{bias} is the voltage applied to the device, and d is the thickness of the QW. As the negative bias is increased more, the energy band is tilted in opposite direction, separating the electron and hole wave function again. Correspondingly, the carrier lifetime is increased.

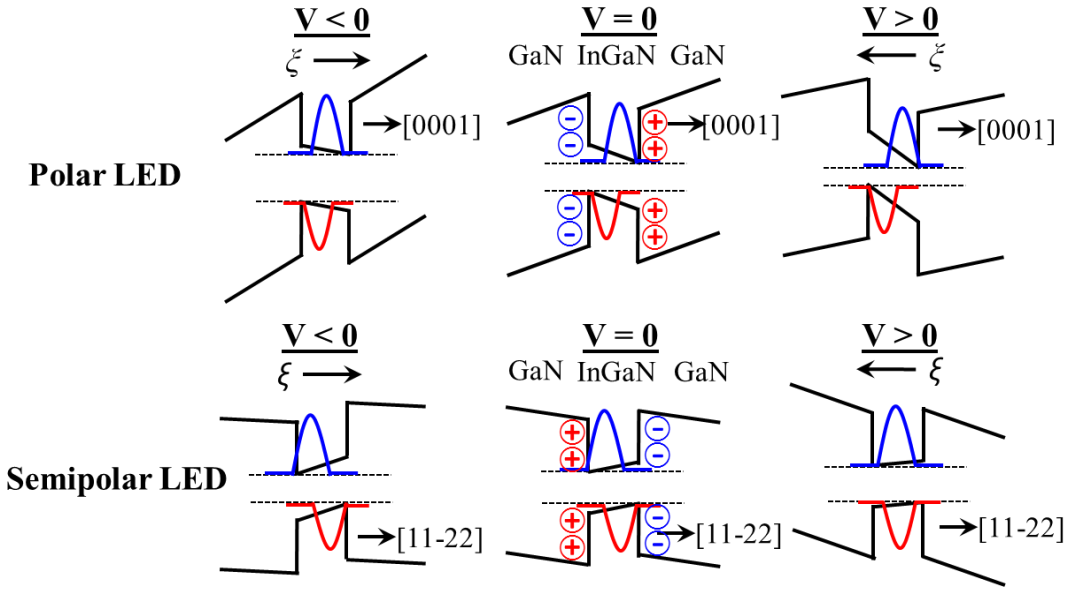

Figure 6.5 Schematic energy band diagrams for polar and semipolar GaN LEDs with negative (V<0), zero and positive (V>0) external voltage bias.

On the other hand, for the semipolar LED device, since the [11-22] growth orientation is 58.4 °away from the [0001] axis [117, 118], the quantum well structure grown along this orientation experiences weaker strain-induced polarization, and the polarization direction is opposite to the c-axis [119]. Therefore, the energy band tilts with smaller amplitude and opposite direction under zero-bias condition. With positive bias voltage, the external electric field is in opposite direction with the internal field, making the energy band more flat. While the negative bias condition provides an external electric field in the same direction with the internal field and causes the energy band to be further tilted. This agrees with the shifting of the PL spectra observed in Figure 6.2(b). Based on the energy band analysis on the polar quantum well structure, the semipolar LED should display a shorter carrier lifetime under the positive bias, and longer lifetime under reverse bias. However, the opposite trend has been observed here. This phenomenon is believed to be caused by the

weakly delocalized excitons in the semipolar oriented QWs. Since the excitons have higher binding energy in the polar QWs, they are more localized and have less influence on the carrier recombination process. On the other hand, the binding energy of the excitons in the semipolar QWs is smaller [120]. Hence, more excitons are able to participate the recombination process are cause fluctuations to the carrier lifetime. The details about the influence of exciton recombination are still under study progress.

6.4. Conclusion

In summary, InGaN/GaN multiple quantum well LEDs grown on the polar and semipolar planes have been studied to understand the carrier dynamics and emission kinetics. The semipolar LED shows a more stable EL emission, opposite PL emission peak shift trend, and a shorter carrier lifetime, as compared to the polar LED. The performance differences of the LED devices are attributed to the different internal polarization field originated from the growth orientation.

Chapter 7. Application of GaN LEDs - Tunable White Light Emission

A tunable white light source based on GaN LED chip utilizing colloidal quantum dot (QD) color convertors is demonstrated in this chapter. The GaN LED chip is designed to have current-dependent dual-wavelength emission, serving as the excitation source for the QD phosphors. With spectral content of blue, green and red colors, a combinational white light is generated with tunable and high quality of color rendering index and correlated color temperature.

7.1. Introduction

GaN based white light emitting diodes show promising potential in replacing the conventional incandescent light bulbs and fluorescent light tubes, thanks to their high energy conversion efficiency, long life span, and low maintenance cost. Besides, the GaN LED white light sources also play important role in the display applications, owning to their compact size and rich color content. Conventional white light LEDs utilize InGaN/GaN based blue LED chip, integrated with rear-earth-doped yttrium aluminum garnet (YAG) phosphor materials, to generate white light consisting of blue and green/yellow color components [11, 121].

Besides the brightness and power efficiency, the quality of a light source is also of great concern for real applications in lighting and display. Two major criteria are commonly adopted to describe the photometric quality of a specific white light source,

namely, the color rendering index (CRI) and the correlated color temperature (CCT). The CRI is defined as the capability of a white light source to reproduce the original colors of an illuminated object as seen under an ideal white light source. The CCT, in units of Kelvin (K), is used to describe the hue characteristics causing visual feeling of “warm” or “cool”. Currently, the color characteristics of the GaN based white LEDs still needs to be improved for applications requiring high color quality, like indoor lighting. The inorganic phosphor materials, used to convert blue light to green, yellow and even red lights, usually have longer tail emission in the green/yellow region. The conversion efficiency into red is still not high enough, when compared to that of the green and yellow color.

Meanwhile, the colloidal quantum dots, with particle size in nanometer scale, offer promising performance in converting the shorter wavelength photons to longer wavelength photons. These phosphor particles display unique merits of high external quantum efficiency, narrow full width half maximum of emission, full coverage of visible color spectrum, and freedom of color adjustability through size-tuning [122]. A display panel based on high efficiency QDs has been demonstrated with reasonably good performance [123]. GaN based white LEDs employing QDs as color converters have also been reported for potential applications [85, 124-126]. However, for all those white light sources, they hold stationary color performance, meaning that once the white light emitting device is fabricated, the CRI and CCT are fixed permanently.

In this part, a tunable white light source with current dependent color rendering index and correlated color temperature is demonstrated by combining InGaN/GaN blue LED chips with dual wavelength emission peaks together with green/red quantum dots phosphor color converters. The white light source presents a current-dependent CRI from 72 to 83, and CCT from 3988 to 5264 K, when the operating

current changes from 70 to 120 mA. The light property variation is attributed to the combinational effects of the change in the excitation source intensity in the GaN blue LED chip and the corresponding change in the down-converted green/red emission from the QDs.

7.2. Fabrication of Tunable LEDs

The dual-wavelength emitting GaN LED wafer was grown on c-plane sapphire using metal-organic chemical vapor deposition (MOCVD). The epitaxial structure consists of 30 nm thick low temperature grown GaN nucleation layer, 4 μm thick undoped GaN, 3 μm thick Si-doped n-GaN, 8 pairs of InGaN/GaN (3 nm/12 nm) MQWs, and 150 nm thick Mg-doped p-GaN. Among the 8 pairs of QWs, the first five InGaN QWs close to n-GaN layer were grown at 730 ℃ and have an indium content of about 17%. While the last three QWs close to p-GaN were grown at 750 ℃ and possess indium content of 15%. Mesa etching was performed to expose the n-GaN layer and metal contacts to the n-GaN and p-GaN were deposited for current injection through probes.

The synthesis of green and red emitting CdSe/ZnS core/shell structure quantum dots with a composition gradient have been carried out under fume hood environment, using controlled temperature, pressure and Argon flow via a Shlenk line based on a modified recipe of Bae *et al.* [127]. The synthesized green and red QDs were dispersed in toluene and mixed with poly(methyl methacrylate) (PMMA) (ca. 1:10 toluene:PMMA ratio using Microchem PPMA A15) and coated on the GaN LED chip. Hence, a solid film containing high density QDs was made to cover the whole chip area as color converters.

The electroluminescence (EL) spectra of the LED chip were measured using an integrating sphere, and the CRI, CCT and chromaticity coordinate were calculated accordingly. Figure 7.1 shows the EL spectra of the GaN LED chip under varying current from 70 to 120 mA. Two separated emission peaks, centered at 425 and 462 nm could be observed from the spectra, due to different indium incorporation into the QWs grown at different temperatures. The 425 nm emission peak originates from the QWs grown at 750 ℃, while the 462 nm peak is originated from the QWs grown at 730 ℃. At lower current injection levels, the emission is dominated by the shorter wavelength peak, due to the limited hole penetration depth within the MQWs active region. When the operating current is increased, the intensity of the 425 nm peak is saturated, and a drastic increase of emission intensity at the 462 nm peak is observed. This is because under high driving current, a large amount of holes are injected into the MQWs active region, leading to hole accumulation within the QWs close to the p-GaN layer. The saturation of recombination rate in the last QWs (grown at 750 ℃) is reflected in the saturation of the emission peak at 425 nm. The excess holes tend to penetrate further into the deeper quantum wells, and have high radiative recombination there with electrons. Hence, the light emission at 462 nm, corresponding to deeper QWs, is higher at higher current levels. The hole transport depth difference under different current levels makes the blue emission tunable.

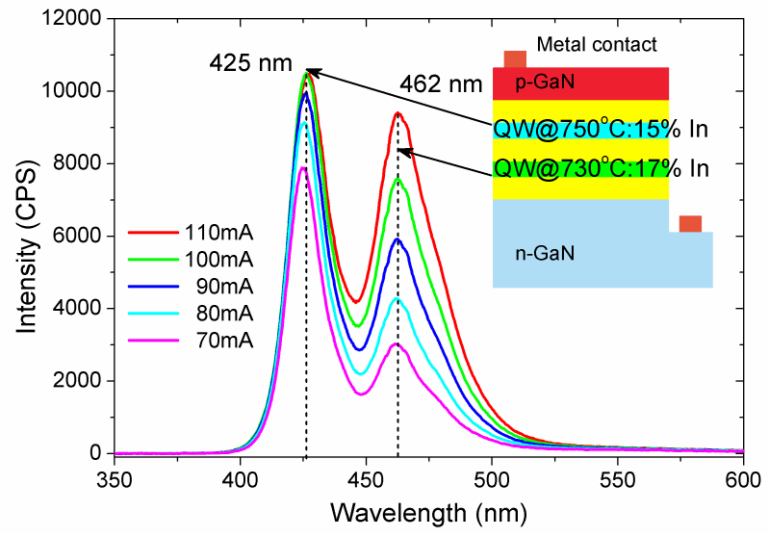

Figure 7.1 Electroluminescence spectra of GaN LED chip emitting at 425 and 462 nm under current level from 70 to 120 mA. Inset shows the epitaxial structure of the dual-wavelength emitting InGaN/GaN LED chip.

The photoluminescence (PL) spectra and UV-Vis absorbance of the green and red quantum dot films are shown in Figures 7.2(a) and 7.2(b), respectively. The green QD film has a PL emission peak at 569 nm, with a FWHM of 25 nm. For the red quantum dots film, a PL emission peak centered at 630 nm, with a FWHM of 29 nm, was detected. The green QD film shows a higher absorbance at 425 nm excitation wavelength, but a lower absorbance at 460 nm wavelength, as compared to the red QD film.

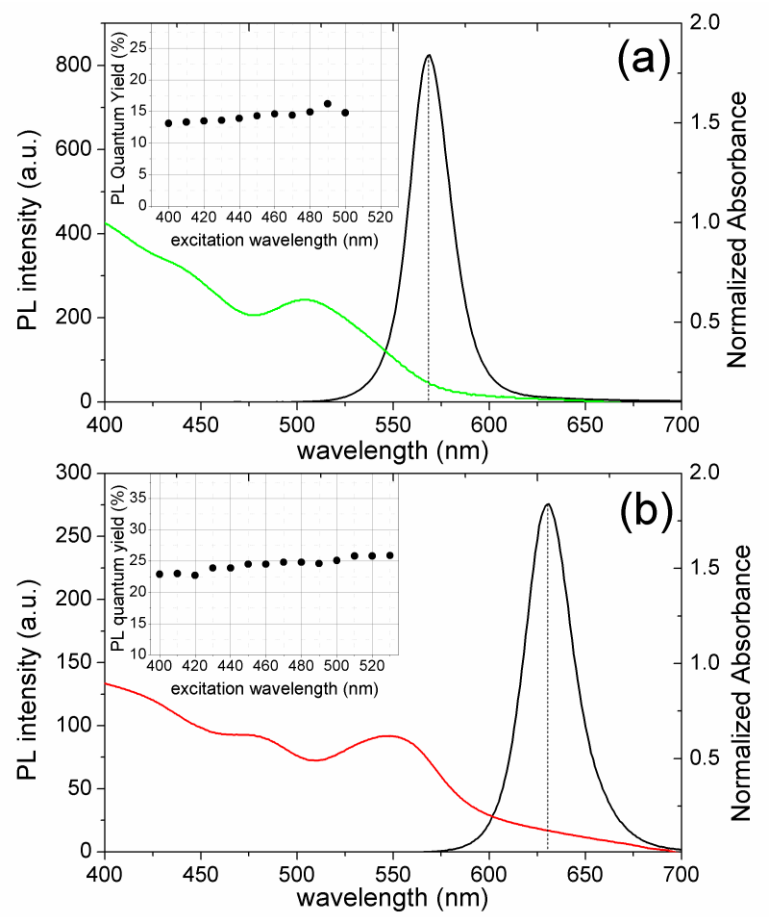

Figure 7.2 Photoluminescence spectra and absorption spectra of (a) green and (b) red quantum dots films. Inset shows the corresponding quantum yields in solid film.

The in-film quantum yields were characterized using Hamamatsu quantum yield measurement setup, for both green and red QD films, as shown in the inset of Figures 7.2(a) and 7.2(b). It can be read from the figure that the green QD film has a 15% yield and the red QD film has a 25% yield under blue region excitation wavelength in this implementation.

7.3. Tunable White Light Emission

After coating the green and red QD films on top of the GaN chip, the EL spectra of the white light emitting device were captured under different current levels, as

shown in Figure 7.3. Four emission peaks falling in blue (centered at 425 and 462 nm), green (centered at 560 nm) and red (centered at 625 nm) color region can be clearly identified from the spectra, making up the white spectrum. With increasing current from 70 to 120 mA, the intensity of the emission peak at 462 nm increases faster than that at the 425 nm, as analyzed in the earlier part. Correspondingly, the red emission peak at 625 nm increases faster than the 560 nm peak, since the excitation source for the red QDs is increased more.

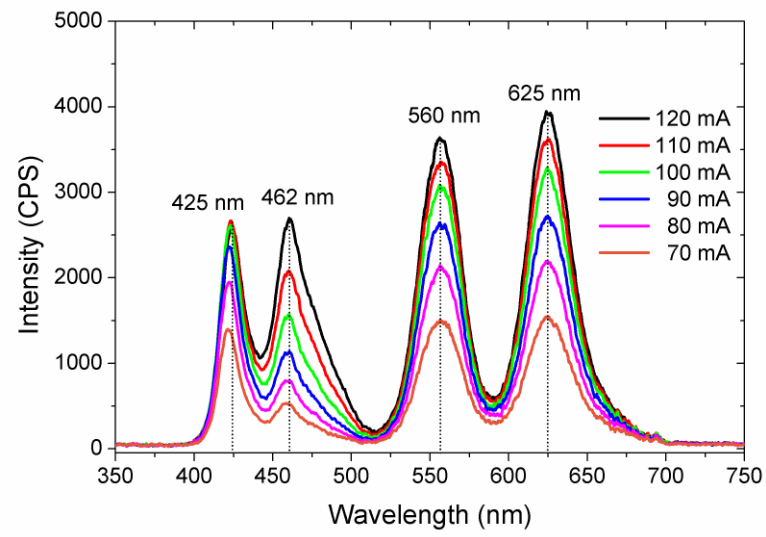

Figure 7.3 Electroluminescence spectra of dual-wavelength emitting GaN LED chip coated with green/red quantum dots film, under operating current from 70 to 120 mA.

The current-dependent color rendering index and correlated color temperature of the white light source are extracted and shown in Figure 7.4(a). When the driving current is increased from 70 to 120 mA, the CRI changes accordingly from 72 to 83, and the CCT increases from 3988 to 5264 K. Figure 7.4(b) illustrates the chromaticity coordinates (CIE-1931) extracted from the spectra under different operating currents. It can be found that the color coordinates are all close to the optimal white light source coordinate at (0.333, 0.333). As the driving current is increased from 70 to 120

mA, the color coordinates shift from (0.371, 0.339) to (0.336, 0.299), indicating a transfer from yellowish/orange region to blue/purple region.

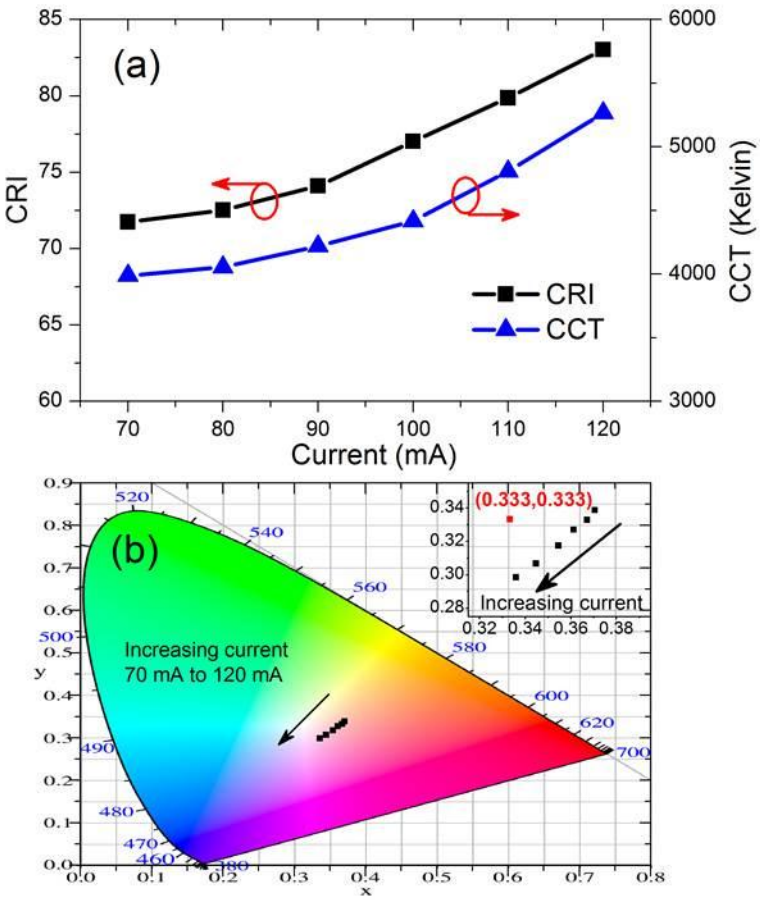

Figure 7.4 (a) Current-dependent CRI and CCT and (b) chromaticity coordinate of the GaN/QD white LED.

The overall efficacy can be further improved through the following approaches: 1) add light extraction features into the blue light emission LED chip. The light extraction efficiency can be enhanced through surface roughening, transparent current spreading layer (to replace the semi-transparent Ni/Au layer), nano-pattering, or graded-refractive-index (GRIN) anti-reflective, and can increase the total brightness of the whole LED chip; and 2) dicing the chip-on-wafer into individual dies. This will reduce the light trapping effect by the large area substrate material.

The CRI is relatively low at this stage, due to the limitation of the packaging capability. However, the optical performance can be improved by optimizing the coating of the colloidal quantum dots. The amount and ratio of the green and red quantum dots can be fine adjusted to reach the best CRI values. Also, with more portions of green and red spectrum components, the resultant light will be more "warm", indicating a CCT close to 3000 K. Meanwhile, the quantum dots can be filled in semi-sphere lens, instead of dispersed on planer glass slides, to fully cover the blue excitation chip. With this configuration, the blue light emitted from the GaN LED chip will be utilized more efficiently.

The current dependence of the CRI and CCT is designed for indoor lighting and display applications, where the light quality can be adjusted according to the different scenes and demands on light (e.g. bedroom, TV display). The tenability of optical performance sacrifices certain brightness performance when the current is tuned to smaller current levels, which is the limitation of the device chip. However, the issue can be solved by designing the epitaxial structure of the blue LED chip, such that the intensity of the dual-peak emission spectrum can vary obviously within a smaller current range. Thus the brightness will not be affected much.

7.4. Conclusion

In conclusion, a GaN based tunable white light source is realized. By combining the emission peaks from the dual-wavelength emission GaN LED chips in conjugation with green/red emission QD phosphor color converting layers, the LED device is able to generate variable CRI above 70 and adjustable color temperature covering both cool and warm white light. The proposed device structure offers tunable operation for GaN based LED light sources. However, the epitaxial LED

design needs to be revised to further increase the color quality and provide color tenability while sustaining the same level of output power.

Chapter 8. Conclusions and Recommendations

8.1. Conclusions

GaN based light-emitting diodes provide unique advantages as highly efficient, low energy cost, and reliable lighting sources, and hold promising potential to be the next generation lighting sources. The technical barriers for the development of high efficiency white LEDs have been reviewed. Epitaxial wafers with high crystal quality and uniformity are grown using metal-organic chemical vapor deposition method. A simple, but stable and reliable micro-fabrication process is demonstrated for the fabrication of lateral LED chips, serving as a standard procedure for quality check of the grown wafers. Based on the standard growth, fabrication and characterization techniques, novel structure designs have been proposed to address the issues that limit the performance of LED chips.

The difficulty of hole transport into the multiple quantum wells region is addressed by partially doping the QBs with p-type dopants. A dual-wavelength emission method is employed as an effective tool to examine the carrier transport and recombination behavior within the active region. By inserting a thin layer of Mg-doped GaN into the QBs close to the p-GaN region, the potential energy barriers for holes are reduced, allowing holes to penetrate deeper into the QWs. Therefore, the hole distribution within the MQWs is more uniform, and carrier crowding is avoided. As a result, enhanced optical and electrical performance is observed from the p-doped QB structure.

Compared to the conventional way of preventing electron overflow, which relies on inserting a p-typed doped AlGaN layer between the MQWs and the p-GaN layer, the n-type EBL is more efficient in suppressing the electron overflow, while not hindering hole injection. While the large band gap p-AlGaN layer creates a potential energy barrier for electrons to confine them within the MQWs, it also creates a barrier for the hole injection form p-GaN to the QWs. In contrast, the n-AlGaN EBL is able to block the excess electrons before they enter the QWs. Hence, there is less chance for excess electron overflow, and the electron accumulation in the last QW (close to the p-GaN layer) is avoided. On the other hand, the suppression of hole injection is eliminated, since the n-EBL is not on the hole injection path to the QWs. Additionally, it helps to confine the holes within the QWs and prevents any possible leakage into the n-GaN. Consequently, the radiative recombination rates are more uniform and higher within each individual QW, in agreement with the measured optical power results.

The influence of polarity difference on the carrier recombination dynamics and emission kinetics has also been comparatively studied. Multiple quantum well structures grown on polar and semipolar planes experience opposite polarity fields, which cause the different electroluminescence and photoluminescence response when the devices are under external electrical field bias. The measured absorption spectra also provide an evidence for the effective band gap shifting under external bias. The semipolar LED structure also exhibits a much faster decay time, indicating a deeper overlapping between electron and hole wave functions, and hence a higher radiative recombination rate within the QWs.

Through tuning the red, green and blue color components, a current-dependent tunable white light source has been achieved. The chromaticity parameters of CRI and

CCT are adjustable by varying the operating current of the device. The white light emitting device consists of a dual-wavelength emission blue LED chip and red/green phosphor particles in nanometer scale. When adjusting the working current, the intensity of emission peaks at different wavelengths is changed, which further causes the photoluminescence emission intensity change of the red and green lights. The design gives a closer look into the optimization of high quality light sources.

In summary, the thesis covers the knowledge of physical modeling, structure design, epitaxial growth, device fabrication and characterization, as well as an extended application of InGaN/GaN LED. Both experimental results and theoretical analyses are presented to support the proposed ideas and the inferred conclusions. The work provides an insightful understanding of the GaN LED device and a clear guide for the design and development of high performance GaN LED for solid state lighting and displays.

8.2. Recommendations for Future Work

The carrier distribution could be further optimized through quantum barrier engineering, including doping, thickness and growth condition adjustments. The QBs will be carefully designed to reduce the energy barrier for hole transport, and assists to form a more uniformly distributed carrier concentration as well as radiative recombination, such that the MQWs will be fully utilized for photon generation. Ultimately, the internal quantum efficiency will be substantially enhanced.

So far, the fabricated devices consist of the basic structure with mesa and electrodes only, and no light extraction structures are included here. As a result, most of the light generated are trapped within the device by internal reflections. More study on the light extraction efficiency enhancement will be carried out, including replacing

the Ni/Au current spreading layer with transparent and conductive ITO layer, performing surface texturing to increase device/air interface roughness, depositing reflective mirror at back side of the non-conductive substrate. This additional process steps will lead to substantial increase of the brightness of the device, and hence the measured optical output power and external quantum efficiency.

For high brightness lighting application, the LED devices have to operate under high current levels to generate high lumen flux. With the existing lateral device configuration, the current spreading by the n-GaN would be difficult, leading to current crowding near the metal electrode. The vertical LED structure, however, is able to eliminate the current crowding, allowing for high current operation of the device. The GaN epitaxial layer is transferred to a metal (for example, copper or nickel) supporting carrier, and lifted-off from the sapphire substrate. The metal carrier provides high electrical and thermal conductivity, and could be processed for high reflectance.

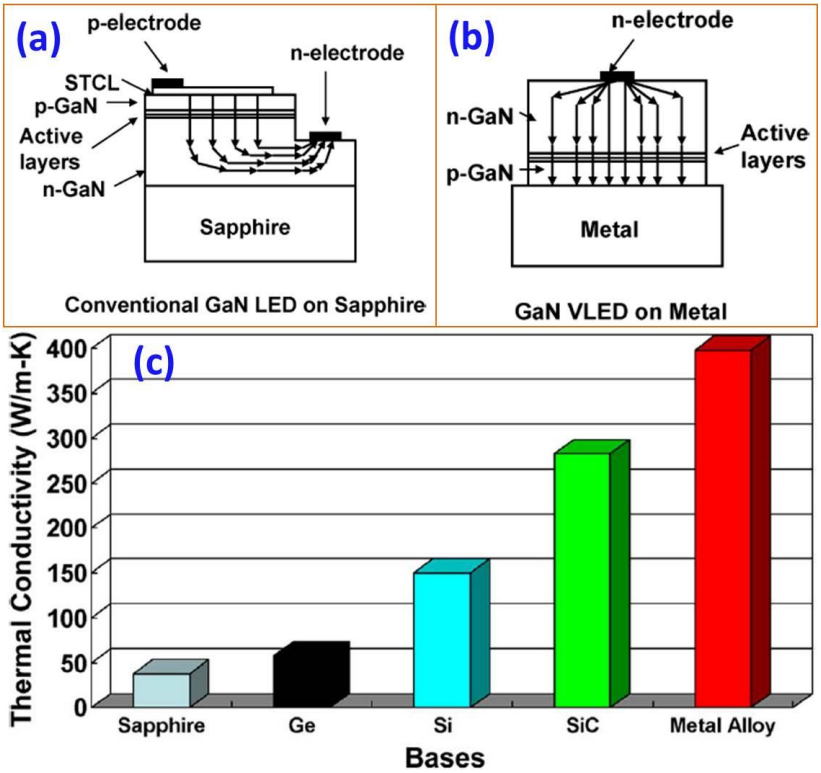

Figure 8.1 Current flow path of (a) a conventional GaN LED on sapphire; (b) a GaN vertical LED on a metal substrate; and (c) comparison of thermal conductivity of different GaN LED substrates [128].

Moreover, after the laser lift-off, the p-n layers are inverted, meaning that the n-GaN layer, together with the u-GaN buffer, is facing up. Since the n-GaN and u-GaN (normally > 5μm) is much thicker than the p-GaN layer (~ 200 nm), there is more space for surface texturing and periodic pattering. Hence, more effective light extraction structures could be employed to further optimize the device performance.

Publication List

Journal Publications

1. **Y. Ji**, W. Liu, T. Erdem, R. Chen, S. T. Tan, Z.-H. Zhang, Z. Ju, X. Zhang, H. Sun, X. W. Sun, Y. Zhao, S. P. DenBaars, S. Nakamura, and H. V. Demir, "Comparative study of field-dependent carrier dynamics and emission kinetics of InGaN/GaN light-emitting diodes grown on $(11\bar{2}2)$ semipolar versus (0001) polar planes," Applied Physics Letters **104**, 143506 (2014).
2. **Y. Ji**, Z.-H. Zhang, Z. Kyaw, S. T. Tan, Z. G. Ju, X. L. Zhang, W. Liu, X. W. Sun, and H. V. Demir, "Influence of n-type versus p-type AlGaN electron-blocking layer on InGaN/GaN multiple quantum wells light-emitting diodes," Applied Physics Letters **103**, 053512 (2013).
3. **Y. Ji**, Z.-H. Zhang, S. T. Tan, Z. G. Ju, Z. Kyaw, N. Hasanov, W. Liu, X. W. Sun, and H. V. Demir, "Enhanced hole transport in InGaN/GaN multiple quantum well light-emitting diodes with a p-type doped quantum barrier," Opt. Lett. **38**, 202-204 (2013).
4. **Y. Ji**, E. Mutlugun, S. T. Tan, W. Liu, T. Erdem, X. W. Sun, and H. V. Demir, "Dual-wavelength emitting GaN LED chip integrated with quantum dot color converters for tunable white light source," in preparation.
5. Z. Kyaw, Z.-H. Zhang, W. Liu, S. T. Tan, Z. G. Ju, X. L. Zhang, **Y. Ji**, N. Hasanov, B. Zhu, S. Lu, Y. Zhang, J. H. Teng, X. W. Sun, and H. V. Demir, "Simultaneous enhancement of electron overflow reduction and hole injection promotion by tailoring the last quantum barrier in InGaN/GaN light-emitting diodes," Applied Physics Letters **104**, 161113 (2014).

6. Z.-H. Zhang, Z. Ju, W. Liu, S. T. Tan, **Y. Ji**, Z. Kyaw, X. Zhang, N. Hasanov, X. W. Sun, and H. V. Demir, "Improving hole injection efficiency by manipulating the hole transport mechanism through p-type electron blocking layer engineering," Optics Letters **39**, 2483-2486 (2014).
7. Z.-H. Zhang, W. Liu, S. T. Tan, Z. Ju, **Y. Ji**, Z. Kyaw, X. Zhang, N. Hasanov, B. Zhu, S. Lu, Y. Zhang, X. W. Sun, and H. V. Demir, "On the mechanisms of InGaN electron cooler in InGaN/GaN light-emitting diodes," Optics Express **22**, A779-A789 (2014).
8. Z. G. Ju, W. Liu, Z.-H. Zhang, S. T. Tan, **Y. Ji**, Z. Kyaw, X. L. Zhang, S. P. Lu, Y. P. Zhang, B. B. Zhu, N. Hasanov, X. W. Sun, and H. V. Demir, "Advantages of the Blue InGaN/GaN Light-Emitting Diodes with an AlGaN/GaN/AlGaN Quantum Well Structured Electron Blocking Layer," ACS Photonics **1**, 377-381 (2014).
9. Z.-H. Zhang, **Y. Ji**, W. Liu, S. Tiam Tan, Z. Kyaw, Z. Ju, X. Zhang, N. Hasanov, S. Lu, Y. Zhang, B. Zhu, X. Wei Sun, and H. Volkan Demir, "On the origin of the electron blocking effect by an n-type AlGaN electron blocking layer," Applied Physics Letters **104**, 073511 (2014).
10. Z. Kyaw, Z.-H. Zhang, W. Liu, S. T. Tan, Z. G. Ju, X. L. Zhang, **Y. Ji**, N. Hasanov, B. Zhu, S. Lu, Y. Zhang, X. W. Sun, and H. V. Demir, "On the effect of N-GaN/P-GaN/N-GaN/P-GaN/N-GaN built-in junctions in the n-GaN layer for InGaN/GaN light-emitting diodes," Optics Express **22**, 809-816 (2014).
11. Z.-H. Zhang, S. Tiam Tan, Z. Kyaw, W. Liu, **Y. Ji**, Z. Ju, X. Zhang, X. Wei Sun, and H. Volkan Demir, "p-doping-free InGaN/GaN light-emitting diode driven by three-dimensional hole gas," Applied Physics Letters **103**, 263501 (2013).

12. Z.-H. Zhang, S. T. Tan, W. Liu, Z. Ju, K. Zheng, Z. Kyaw, **Y. Ji**, N. Hasanov, X. W. Sun, and H. V. Demir, "Improved InGaN/GaN light-emitting diodes with a p-GaN/n-GaN/p-GaN/n-GaN/p-GaN current-spreading layer," Opt. Express **21**, 4958-4969 (2013).
13. Z.-H. Zhang, S. T. Tan, Z. Kyaw, **Y. Ji**, W. Liu, Z. Ju, N. Hasanov, X. W. Sun, and H. V. Demir, "InGaN/GaN light-emitting diode with a polarization tunnel junction," Applied Physics Letters **102**, 193508 (2013).
14. Z. G. Ju, W. Liu, Z. H. Zhang, S. T. Tan, **Y. Ji**, Z. B. Kyaw, X. L. Zhang, S. P. Lu, Y. P. Zhang, B. B. Zhu, N. Hasanov, X. W. Sun, and H. V. Demir, "Improved hole distribution in InGaN/GaN light-emitting diodes with graded thickness quantum barriers," Applied Physics Letters **102**, 243504 (2013).
15. Z.-H. Zhang, S. T. Tan, Z. Ju, W. Liu, **Y. Ji**, K. Zabu, D. Yilmaz, X. W. Sun, and H. V. Demir, "On the effect of step-doped quantum barriers in InGaN/GaN light emitting diodes," Display Technology, Journal of **9**, 226-233 (2013).
16. Z. Kyaw, W. Jianxiong, K. Dev, S. T. Tan, Z. Ju, Z.-H. Zhang, **Y. Ji**, N. Hasanov, W. Liu, X. W. Sun, and H. V. Demir, "Room-temperature larger-scale highly ordered nanorod imprints of ZnO film," Optics Express **21**, 26846-26853 (2013).
17. X. Yang, Y. Tang, S. T. Tan, M. Bosman, Z. Dong, K. S. Leck, **Y. Ji**, H. V. Demir, and X. W. Sun, "Facile Synthesis of Luminescent AgInS2–ZnS Solid Solution Nanorods," Small **9**, 2689-2695 (2013).
18. Z.-H. Zhang, S. T. Tan, **Y. Ji**, W. Liu, Z. Ju, Z. Kyaw, X. W. Sun, and H. V. Demir, "A PN-type quantum barrier for InGaN/GaN light emitting diodes," Opt. Express **21**, 15676-15685 (2013).
19. B. Peng, Q. Zhang, X. Liu, **Y. Ji**, H. V. Demir, C. H. A. Huan, T. C. Sum, and Q. Xiong, "Fluorophore-doped core–multishell spherical plasmonic nanocavities:

resonant energy transfer toward a loss compensation," ACS Nano **6**, 6250-6259 (2012).

20. Z. G. Ju, S. T. Tan, Z. H. Zhang, **Y. Ji**, Z. Kyaw, Y. Dikme, X. W. Sun, and H. V. Demir, "On the origin of the redshift in the emission wavelength of InGaN/GaN blue light emitting diodes grown with a higher temperature interlayer," Applied Physics Letters **100**, 123503 (2012).
21. J. Dai, **Y. Ji**, C. X. Xu, X. W. Sun, K. S. Leck, and Z. G. Ju, "White light emission from CdTe quantum dots decorated n-ZnO nanorods/p-GaN light-emitting diodes," Applied Physics Letters **99**, 063112 (2011).

Conference Presentations

1. **Y. Ji**, S. T. Tan, Z. G. Ju, Z.-H. Zhang, K. Zabu, N. Hasanov, W. Liu, X. W. Sun, and H. V. Demir, "Dual wavelength study on hole transport behaviour with p-type doped quantum barriers," presented at the The 5th IEEE International Nanoelectronics Conference (INEC) 2013, Resorts World Sentosa, Singapore, 2 - 4 January 2013.
2. Z. G. Ju, S. T. Tan, Z.-H. Zhang, **Y. Ji**, K. Zabu, X. W. Sun, and H. V. Demir, "Growth optimization of the low temperature uGaN interlayer for high power InGaN/GaN blue light emitting diodes " presented at the ICMAT 2013 - 7th International Conference on Materials for Advanced Technologies, Suntec, Singapore, 30 June - 5 July 2013.
3. Z.-H. Zhang, S. T. Tan, W. Liu, Z. G. Ju, K. Zabu, **Y. Ji**, X. W. Sun, and H. V. Demir, "Enhanced optical power for InGaN/GaN light-emitting diodes through

the step-doped quantum barriers," presented at the ICMAT 2013 - 7th International Conference on Materials for Advanced Technologies, Suntec, Singapore, 30 June - 5 July 2013.

4. K. Zabu, S. T. Tan, W. Liu, Z. G. Ju, Z.-H. Zhang, **Y. Ji**, X. W. Sun, and H. V. Demir, "Influence of the Interval Growth Temperature Between the Nucleation Layer Growth and the High Crystalline GaN Growth on Quality of GaN Films Grown by MOCVD," presented at the ICMAT 2013 - 7th International Conference on Materials for Advanced Technologies, Suntec, Singapore, 30 June - 5 July 2013.
5. Z. G. Ju, S. T. Tan, Z.-H. Zhang, **Y. Ji**, K. Zabu, Y. Dikme, X. W. Sun, and H. V. Demir, "The study on the uGaN interlayer to the performance of InGaN/GaN blue light emitting diodes " presented at the 9th International Symposium on Semiconductor Light Emitting Devices 2012, Berlin, Germany, 22 - 27 July 2012.

Bibliography

1. U.S. Energy Information Administration, "How much electricity is used for lighting in the United States?," http://www.eia.gov/tools/faqs/faq.cfm?id=99&t=3 (Retrived 2014).
2. J. I.Pankove, E. A. Miller, D. Richman, and J. E. Berkeyheiser, "Electroluminescence in GaN," J. Luminescence **4**, 63 (1971).
3. J. I.Pankove, E. A. Miller, and J. E. Berkeyheiser, "GaN blue light-emitting diodes," J. Luminescence **5**, 84 (1972).
4. H. P. Maruska, D. A. Stevenson, and J. I. Pankove, "Violet luminescence of Mg-doped GaN (light-emitting diode properties)," Appl. Phys. Lett. **22**, 303 (1973).
5. H. Amano, M. Kito, K. Hiramatsu, and I. Akasaki, "P-Type Conduction in Mg-Doped GaN Treated with Low-Energy Electron Beam Irradiation (LEEBI)," Jpn. J. Appl. Phys. **28**, L2112-L2114 (1989).
6. S. Nakamura, N. Iwasa, and M. Senoh, "Method of manufacturing p-type compound semiconductor," US Patent **5,306,662** (1994).
7. I. Akasaki, H. Amano, Itoh K., N. Koide, and K. Manabe, "GaN based UV/blue light-emitting devices," GaAs and Related Compounds conference, Inst. Phys. Conf. Ser. **129**, 851 (1992).
8. E. F. Schubert, "History of light-emitting diodes," in *Light-Emitting Diodes*(Cambridge University Press, 2006), pp. 1-26.
9. T. Whitaker, "Cree reports R&D result of 231 lm/W efficacy for white LED," LEDs Magazine http://ledsmagazine.com/news/8/5/8, 2011 (Retrived in April 2013).

10. M. Wright, "Cree announces a new laboratory LED efficacy milestone at SIL," LEDs Magazine http://ledsmagazine.com/news/10/2/16, 2013 (Retrived in April 2013).

11. S. Pimputkar, J. S. Speck, S. P. DenBaars, and S. Nakamura, "Prospects for LED lighting," Nat Photon **3**, 180-182 (2009).

12. P. Flesch, *Light and Light Sources* (Springer Berlin Heidelberg, 2006).

13. M. R. Krames, O. B. Shchekin, R. Mueller-Mach, G. O. Mueller, Z. Ling, G. Harbers, and M. G. Craford, "Status and Future of High-Power Light-Emitting Diodes for Solid-State Lighting," Display Technology, Journal of **3**, 160 (2007).

14. EnergyStar, "Lighting Technologies: A Guide to Energy-Efficienct Illumination," http://www.energystar.gov/ia/partners/promotions/change_light/downloads/Fact%20Sheet_Lighting%20Technologies.pdf (Retrived in April 2013).

15. ElectronicGadgtes, "Where are LED Lights Used For," http://electronicgadgtes.wordpress.com/ (2013).

16. All-Accesspries-for-Your-Vehicle, "LED Automotive," http://accessories-for-a-car.info/led-automotive/ (2013).

17. Inhabitat, "World's Largest LED Project Completed in Abu Dhabi," http://pressroom.gelighting.com/news/glittering-lighting-makeover-for-234525 (2009).

18. G. E. Lighting, "Glittering Lighting Makeover for Tower Bridge Readies London's World-Famous Icon for Historic Year 2012," http://pressroom.gelighting.com/news/glittering-lighting-makeover-for-234525 (2012).

19. U.S. Department of Energy, "Energy Savings Potential of Solid-State Lighting in General Illumination Applications,"

http://apps1.eere.energy.gov/buildings/publications/pdfs/ssl/ssl_energy-savings-report_jan-2012.pdf (2012).

20. S. T. Tan, X.W. Sun, H. V. Demir, and S. P. DenBaars, "Advances in the LED Materials and Architectures for Energy-Saving Solid-State Lighting Toward "Lighting Revolution"," IEEE Photon. J. **4**, 561 (2012).
21. I. Vurgaftman, J. R. Meyer, and L. R. Ram-Mohan, "Band parameters for III--V compound semiconductors and their alloys," Journal of Applied Physics **89**, 5815-5875 (2001).
22. H. Harima, "Properties of GaN and related compounds studied by means of Raman scattering," Journal of Physics: Condensed Matter **14**, R967 (2002).
23. B. Monemar, "III-V nitrides—important future electronic materials," Journal of Materials Science: Materials in Electronics **10**, 227-254 (1999).
24. D. K. Gaskill, L. B. Rowland, and K. Doverspike, in *Properties of group III nitrides*, J. H. Edgar, ed. (INSPEC, Institution of Electrical Engineers, 1994), pp. 101-116.
25. S. Strite, and H. Morkoc, "GaN, AlN, and InN: A review," Journal of Vacuum Science & Technology B: Microelectronics and Nanometer Structures **10**, 1237-1266 (1992).
26. T. L. Tansley, in *Properties of group III nitrides*, J. H. Edgar, ed. (INSPEC, Institution of Electrical Engineers, 1994), pp. 35-40.
27. J. Holst, L. Eckey, A. Hoffmann, I. Broser, B. Schottker, D. J. As, D. Schikora, and K. Lischka, "Mechanisms of optical gain in cubic gallium nitrite," Applied Physics Letters **72**, 1439-1441 (1998).

28. J. Wu, W. Walukiewicz, W. Shan, K. M. Yu, J.W.Ager, E. E. Haller, H. Lu, and W. J. Schaff, "Effects of the narrow band gap on the properties of InN," Phys. Rev. B **66**, 201403 (2002).
29. S. Krukowski, A. Witek, J. Adamczyk, J. Jun, M. Bockowski, I. Grzegory, B. Lucznik, G. Nowak, M. Wróblewski, A. Presz, S. Gierlotka, S. Stelmach, B. Palosz, S. Porowski, and P. Zinn, "Thermal properties of indium nitride," Journal of Physics and Chemistry of Solids **59**, 289-295 (1998).
30. E. F. Schubert, "The AlGaInN material system and ultraviolet emitters," in *Light-Emitting Diodes*(Cambridge University Press, 2006), pp. 222-238.
31. F. Bernardini, V. Fiorentini, and D. Vanderbilt, "Spontaneous polarization and piezoelectric constants of III-V nitrides," Physical Review B **56**, R10024-R10027 (1997).
32. O. Ambacher, J. Smart, J. R. Shealy, N. G. Weimann, K. Chu, M. Murphy, W. J. Schaff, L. F. Eastman, R. Dimitrov, L. Wittmer, M. Stutzmann, W. Rieger, and J. Hilsenbeck, "Two-dimensional electron gases induced by spontaneous and piezoelectric polarization charges in N- and Ga-face AlGaN/GaN heterostructures," Journal of Applied Physics **85**, 3222-3233 (1999).
33. O. Ambacher, B. Foutz, J. Smart, J. R. Shealy, N. G. Weimann, K. Chu, M. Murphy, A. J. Sierakowski, W. J. Schaff, L. F. Eastman, R. Dimitrov, A. Mitchell, and M. Stutzmann, "Two dimensional electron gases induced by spontaneous and piezoelectric polarization in undoped and doped AlGaN/GaN heterostructures," Journal of Applied Physics **87**, 334-344 (2000).
34. H. Zhao, L. Guangyu, A. A. Ronald, and T. Nelson, "Current injection efficiency induced efficiency-droop in InGaN quantum well light-emitting diodes," Solid-State Electronics **54**, 1119–1124 (2010).

35. M.-H. Kim, M. F. Schubert, Q. Dai, J. K. Kim, E. F. Schubert, J. Piprek, and Y. Park, "Origin of efficiency droop in GaN-based light-emitting diodes," Applied Physics Letters **91**, 183507 (2007).

36. D.-S. Shin, D.-P. Han, J.-Y. Oh, and J.-I. Shim, "Study of droop phenomena in InGaN-based blue and green light-emitting diodes by temperature-dependent electroluminescence," Applied Physics Letters **100**, 153506 (2012).

37. Y. C. Shen, G. O. Mueller, S. Watanabe, N. F. Gardner, A. Munkholm, and M. R. Krames, "Auger recombination in InGaN measured by photoluminescence," Applied Physics Letters **91**, 141101 (2007).

38. E. Kioupakis, P. Rinke, K. T. Delaney, and C. G. Van de Walle, "Indirect Auger recombination as a cause of efficiency droop in nitride light-emitting diodes," Applied Physics Letters **98**, 161107 (2011).

39. J. Iveland, L. Martinelli, J. Peretti, J. S. Speck, and C. Weisbuch, "Direct Measurement of Auger Electrons Emitted from a Semiconductor Light-Emitting Diode under Electrical Injection: Identification of the Dominant Mechanism for Efficiency Droop," Physical Review Letters **110**, 177406 (2013).

40. A. A. Efremov, N. I. Bochkareva, R. I. Gorbunov, D. A. Lavrinovich, Y. T. Rebane, D. V. Tarkhin, and Y. G. Shreter, "Effect of the joule heating on the quantum efficiency and choice of thermal conditions for high-power blue InGaN/GaN LEDs," Semiconductors **40**, 605-610 (2006).

41. D. S. Meyaard, Q. Shan, J. Cho, E. F. Schubert, S.-H. Han, M.-H. Kim, C. Sone, S. J. Oh, and J. K. Kim, "Temperature dependent efficiency droop in GaInN light-emitting diodes with different current densities," Applied Physics Letters **100**, 081106 (2012).

42. W. W. Chow, M. H. Crawford, J. Y. Tsao, and M. Kneissl, "Internal efficiency of InGaN light-emitting diodes: Beyond a quasiequilibrium model," Applied Physics Letters **97**, 121105 (2010).

43. S.-J. Chang, S.-F. Yu, R.-M. Lin, S. Li, T.-H. Chiang, S.-P. Chang, and C.-H. Chen, "InGaN-Based Light-Emitting Diodes With an AlGaN Staircase Electron Blocking Layer," IEEE Photonics Technology Letters **24**, 1737 (2012).

44. S.-H. Han, D.-Y. Lee, S.-J. Lee, C.-Y. Cho, M.-K. Kwon, S. P. Lee, D. Y. Noh, D.-J. Kim, Y. C. Kim, and S.-J. Park, "Effect of electron blocking layer on efficiency droop in InGaN/GaN multiple quantum well light-emitting diodes," Applied Physics Letters **94**, 231123 (2009).

45. K. S. Kim, J. H. Kim, S. J. Jung, Y. J. Park, and S. N. Cho, "Stable temperature characteristics of InGaN blue light emitting diodes using AlGaN/GaN/InGaN superlattices as electron blocking layer," Applied Physics Letters **96**, 091104 (2010).

46. S. Choi, H.-J. Kim, S.-S. Kim, J. Liu, J. Kim, J.-H. Ryou, R. D. Dupuis, A. M. Fischer, and F. A. Ponce, "Improvement of peak quantum efficiency and efficiency droop in III-nitride visible light-emitting diodes with an InAlN electron-blocking layer," Applied Physics Letters **96**, 221105 (2010).

47. R. B. Chung, C. Han, C.-C. Pan, N. Pfaff, J. S. Speck, S. P. DenBaars, and S. Nakamura, "The reduction of efficiency droop by Al0.82In0.18N/GaN superlattice electron blocking layer in (0001) oriented GaN-based light emitting diodes," Applied Physics Letters **101**, 131113 (2012).

48. Y. L. Li, Y. R. Huang, and Y. H. Lai, "Efficiency droop behaviors of InGaN/GaN multiple-quantum-well light-emitting diodes with varying quantum well thickness," Applied Physics Letters **91**, 181113 (2007).

49. C. H. Wang, S. P. Chang, P. H. Ku, J. C. Li, Y. P. Lan, C. C. Lin, H. C. Yang, H. C. Kuo, T. C. Lu, S. C. Wang, and C. Y. Chang, "Hole transport improvement in InGaN/GaN light-emitting diodes by graded-composition multiple quantum barriers," Applied Physics Letters **99**, 171106 (2011).

50. Z. G. Ju, W. Liu, Z. H. Zhang, S. T. Tan, Y. Ji, Z. B. Kyaw, X. L. Zhang, S. P. Lu, Y. P. Zhang, B. B. Zhu, N. Hasanov, X. W. Sun, and H. V. Demir, "Improved hole distribution in InGaN/GaN light-emitting diodes with graded thickness quantum barriers," Applied Physics Letters **102**, 243504 (2013).

51. G. Liu, J. Zhang, H. Zhao, and N. Tansu, "Device characteristics of InGaN quantum well light-emitting diodes with AlInN thin barrier insertion," in *Gallium Nitride Materials and Devices VII*, J.-I. Chyi, Y. Nanishi, H. Morkoç, J. Piprek, and E. Yoon, eds. (2012), p. 82621F.

52. G. Liu, Z. Hongping, J. Zhang, and N. Tansu, "Growths of InGaN-based light-emitting diodes with AlInN thin barrier for efficiency droop suppression," in *2011 Conference on Lasers and Electro-Optics (CLEO)*(IEEE, NEW YORK, Baltimore, MD, 2011), pp. 1-2.

53. A. Hangleiter, D. Fuhrmann, M. Grewe, F. Hitzel, G. Klewer, S. Lahmann, C. Netzel, N. Riedel, and U. Rossow, "Towards understanding the emission efficiency of nitride quantum wells," physica status solidi (a) **201**, 2808-2813 (2004).

54. D. Fuhrmann, C. Netzel, U. Rossow, A. Hangleiter, G. Ade, and P. Hinze, "Optimization scheme for the quantum efficiency of GaInN-based green-light-emitting diodes," Applied Physics Letters **88**, 071105-071103 (2006).

55. J. H. Son, J. U. Kim, Y. H. Song, B. J. Kim, C. J. Ryu, and J.-L. Lee, "Design Rule of Nanostructures in Light-Emitting Diodes for Complete Elimination of Total Internal Reflection," Advanced Materials **24**, 2259-2262 (2012).

56. H. Benisty, H. de Neve, and C. Weisbuch, "Impact of planar microcavity effects on light extraction-Part II: selected exact simulations and role of photon recycling," Quantum Electronics, IEEE Journal of **34**, 1632-1643 (1998).

57. J. J. Wierer, A. David, and M. M. Megens, "III-nitride photonic-crystal light-emitting diodes with high extraction efficiency," Nat Photon **3**, 163-169 (2009).

58. H. Jia, L. Guo, W. Wang, and H. Chen, "Recent Progress in GaN-Based Light-Emitting Diodes," Advanced Materials **21**, 4641-4646 (2009).

59. L. Bo-Wen, C. Chung-Cheng, H. Cheng-Yu, W. Bau-Ming, Y. Sermon Wu, and H. Wen-Ching, "Enhanced Performance of LEDs Using Periodic Tent-Like Post Patterns on A-plane Sapphire Substrates," Photonics Technology Letters, IEEE **23**, 1772-1774 (2011).

60. J. K. Kim, S. Chhajed, M. F. Schubert, E. F. Schubert, A. J. Fischer, M. H. Crawford, J. Cho, H. Kim, and C. Sone, "Light-Extraction Enhancement of GaInN Light-Emitting Diodes by Graded-Refractive-Index Indium Tin Oxide Anti-Reflection Contact," Advanced Materials **20**, 801-804 (2008).

61. J. K. Kim, A. N. Noemaun, F. W. Mont, D. Meyaard, E. F. Schubert, D. J. Poxson, H. Kim, C. Sone, and Y. Park, "Elimination of total internal reflection in GaInN light-emitting diodes by graded-refractive-index micropillars," Applied Physics Letters **93**, 221111 (2008).

62. J. Ho Won, R. Seong Wook, Y. Hak Ki, L. Sanghan, and L. Jong-Lam, "The role of reflective p-contacts in the enhancement of light extraction in nanotextured vertical InGaN light-emitting diodes," Nanotechnology **21**, 025203 (2010).

63. T. Fujii, Y. Gao, R. Sharma, E. L. Hu, S. P. DenBaars, and S. Nakamura, "Increase in the extraction efficiency of GaN-based light-emitting diodes via surface roughening," Applied Physics Letters **84**, 855-857 (2004).

64. S.-J. Wang, K.-M. Uang, S.-L. Chen, Y.-C. Yang, S.-C. Chang, T.-M. Chen, C.-H. Chen, and B.-W. Liou, "Use of patterned laser liftoff process and electroplating nickel layer for the fabrication of vertical-structured GaN-based light-emitting diodes," Applied Physics Letters **87**, 011111 (2005).

65. D. W. Kim, H. Y. Lee, M. C. Yoo, and G. Y. Yeom, "Highly efficient vertical laser-liftoff GaN-based light-emitting diodes formed by optimization of the cathode structure," Applied Physics Letters **86**, 052108 (2005).

66. M. Fujita, S. Takahashi, Y. Tanaka, T. Asano, and S. Noda, "Simultaneous Inhibition and Redistribution of Spontaneous Light Emission in Photonic Crystals," Science **308**, 1296-1298 (2005).

67. H. K. Cho, J. Jang, J.-H. Choi, J. Choi, J. Kim, J. S. Lee, B. Lee, Y. H. Choe, K.-D. Lee, S. H. Kim, K. Lee, S.-K. Kim, and Y.-H. Lee, "Light extraction enhancement from nano-imprintedphotonic crystal GaN-based blue light-emitting diodes," Opt. Express **14**, 8654-8660 (2006).

68. W. Guo, M. Zhang, P. Bhattacharya, and J. Heo, "Auger Recombination in III-Nitride Nanowires and Its Effect on Nanowire Light-Emitting Diode Characteristics," Nano Letters **11**, 1434-1438 (2011).

69. X.-M. Zhang, M.-Y. Lu, Y. Zhang, L.-J. Chen, and Z. L. Wang, "Fabrication of a High-Brightness Blue-Light-Emitting Diode Using a ZnO-Nanowire Array Grown on p-GaN Thin Film," Advanced Materials **21**, 2767-2770 (2009).

70. K. Okamoto, I. Niki, A. Shvartser, Y. Narukawa, T. Mukai, and A. Scherer, "Surface-plasmon-enhanced light emitters based on InGaN quantum wells," Nat Mater **3**, 601-605 (2004).

71. K.-J. Byeon, S.-Y. Hwang, and L. Heon, "Fabrication of two-dimensional photonic crystal patterns on GaN-based light-emitting diodes using thermally curable monomer-based nanoimprint lithography," Applied Physics Letters **91**, 091106 (2007).

72. X. Fu, B. Zhang, X. Kang, J. Deng, C. Xiong, T. Dai, X. Jiang, T. Yu, Z. Chen, and G. Y. Zhang, "GaN-based light-emitting diodes with photonic crystals structures fabricated by porous anodic alumina template," Opt. Express **19**, A1104-A1108 (2011).

73. K. H. Li, and H. W. Choi, "InGaN light-emitting diodes with indium-tin-oxide photonic crystal current-spreading layer," Journal of Applied Physics **110**, 053104 (2011).

74. J. Shakya, K. H. Kim, J. Y. Lin, and H. X. Jiang, "Enhanced light extraction in III-nitride ultraviolet photonic crystal light-emitting diodes," Applied Physics Letters **85**, 142 (2004).

75. D.-H. Kim, C.-O. Cho, Y.-G. Roh, J. Heonsu, Y.-S. Park, J. Cho, J. S. Im, C. Sone, Y. Park, W. J. Choi, and Q. H. Park, "Enhanced light extraction from GaN-based light-emitting diodes with holographically generated two-dimensional photonic crystal patterns," Applied Physics Letters **87**, 203508 (2005).

76. G. Yan, T. Fujii, S. Rajat, F. Kenji, P. D. Steven, N. Shuji, and L. H. Evelyn, "Roughening Hexagonal Surface Morphology on Laser Lift-Off (LLO) N-Face GaN with Simple Photo-Enhanced Chemical Wet tching," Jpn. J. Appl. Phys **43**, L637-L639 (2004).

77. PolyphasicSociety, "Night Lighting - Protecting Your Hormones," http://www.polyphasicsociety.com/polyphasic-sleep/adaptation/night-lighting/ (Retrived in April 2013).

78. T. Erdem, and H. V. Demir, "Semiconductor nanocrystals as rare-earth alternatives," Nat Photon **5**, 126-126 (2011).

79. Lightology, "LED Lighting Basics and The Lighting Facts Label," http://blog.lightology.com/2011/10/14/led-lighting-basics-and-the-lighting-facts-label/ ((2011) Retrived in April 2013).

80. Fosilum, "Why LED Lights," http://www.fosilum.si/en/why-led-lights/correlated-color-temperature--cct/ (2013).

81. S. Pimputkar, J. S. Speck, S. P. DenBaars, and S. Nakamura, "Prospects for LED lighting," Nat. Photonics **3**, 180 (2009).

82. S. Fujita, A. Sakamoto, and S. Tanabe, "Luminescence Characteristics of YAG Glass–Ceramic Phosphor for White LED," Selected Topics in Quantum Electronics, IEEE Journal of **14**, 1387-1391 (2008).

83. H.-S. Chen, K.-W. Wang, S.-S. Chen, and S.-R. Chung, "ZnxCd1−xS quantum dots–based white light-emitting diodes," Opt. Lett. **38**, 2080-2082 (2013).

84. S. Nizamoglu, G. Zengin, and H. V. Demir, "Color-converting combinations of nanocrystal emitters for warm-white light generation with high color rendering index," Applied Physics Letters **92**, 031102-031103 (2008).

85. S. Nizamoglu, T. Erdem, X. W. Sun, and H. V. Demir, "Warm-white light-emitting diodes integrated with colloidal quantum dots for high luminous efficacy and color rendering," Opt. Lett. **35**, 3372-3374 (2010).

86. L.-C. Chen, F.-R. Chen, J.-J. Kai, L. Chang, J.-K. Ho, C.-S. Jong, C. C. Chiu, C.-N. Huang, C.-Y. Chen, and K.-K. Shih, "Microstructural investigation of oxidized Ni/Au ohmic contact to p-type GaN," Journal of Applied Physics **86**, 3826-3832 (1999).

87. Z.-H. Zhang, S. T. Tan, W. Liu, Z. Ju, K. Zheng, Z. Kyaw, Y. Ji, N. Hasanov, X. W. Sun, and H. V. Demir, "Improved InGaN/GaN light-emitting diodes with a p-GaN/n-GaN/p-GaN/n-GaN/p-GaN current-spreading layer," Opt. Express **21**, 4958 (2013).

88. R. Charash, P. P. Maaskant, L. Lewis, C. McAleese, M. J. Kappers, C. J. Humphreys, and B. Corbett, "Carrier distribution in InGaN/GaN tricolor multiple quantum well light emitting diodes," Appl. Phys. Lett. **95**, 151103 (2009).

89. J.-Y. Chang, M.-C. Tsai, and Y.-K. Kuo, "Advantages of blue InGaN light-emitting diodes with AlGaN barriers," Opt. Lett. **35**, 1368 (2010).

90. Y. L. Li, Y. R. Huang, and Y. H. Lai, "Efficiency droop behaviors of InGaN/GaN multiple-quantum-well light-emitting diodes with varying quantum well thickness," Appl. Phys. Lett. **91**, 181113 (2007).

91. C. H. Wang, S. P. Chang, P. H. Ku, J. C. Li, Y. P. Lan, C. C. Lin, H. C. Yang, H. C. Kuo, T. C. Lu, S. C. Wang, and C. Y. Chang, "Hole transport improvement in InGaN/GaN light-emitting diodes by graded-composition multiple quantum barriers," Appl. Phys. Lett. **99**, 171106 (2011).

92. Y.-K. Kuo, M.-C. Tsai, S.-H. Yen, T.-C. Hsu, and Y.-J. Shen, "Effect of P-Type Last Barrier on Efficiency Droop of Blue InGaN Light-Emitting Diodes," IEEE J. Quantum Electron. **46**, 1214 (2010).

93. J. P. Liu, J. H. Ryou, R. D. Dupuis, J. Han, G. D. Shen, and H. B. Wang, "Barrier effect on hole transport and carrier distribution in InGaN/GaN multiple quantum well visible light-emitting diodes," Appl. Phys. Lett. **93**, 021102 (2008).

94. S.-H. Han, C.-Y. Cho, S.-J. Lee, T.-Y. Park, T.-H. Kim, S. H. Park, S. W. Kang, J. W. Kim, Y. C. Kim, and S.-J. Park, "Effect of Mg doping in the barrier of InGaN/GaN multiple quantum well on optical power of light-emitting diodes," Appl. Phys. Lett. **96**, 051113 (2010).

95. Z. G. Ju, S. T. Tan, Z. H. Zhang, Y. Ji, Z. Kyaw, Y. Dikme, X. W. Sun, and H. V. Demir, "On the origin of the redshift in the emission wavelength of InGaN/GaN blue light emitting diodes grown with a higher temperature interlayer," Appl. Phys. Lett. **100**, 123503 (2012).

96. I. Vurgaftman, and J. R. Meyer, "Band parameters for nitrogen-containing semiconductors," J. Appl. Phys. **94**, 3675 (2003).

97. M. H. Crawford, "LEDs for Solid-State Lighting: Performance Challenges and Recent Advances," IEEE J. Sel. Top. Quantum Electron. **15**, 1028 (2009).

98. N. Tansu, H. Zhao, G. Liu, X. H. Li, J. Zhang, H. Tong, and Y. K. Ee, "III-Nitride Photonics," Photonics Journal, IEEE **2**, 241 (2010).

99. Z. Liu, J. Ma, X. Yi, E. Guo, L. Wang, J. Wang, N. Lu, J. Li, I. Ferguson, and A. Melton, "p-InGaN/AlGaN electron blocking layer for InGaN/GaN blue light-emitting diodes," Applied Physics Letters **101**, 261106 (2012).

100. C. S. Xia, Z. M. S. Li, W. Lu, Z. H. Zhang, Y. Sheng, W. Da Hu, and L. W. Cheng, "Efficiency enhancement of blue InGaN/GaN light-emitting diodes with an AlGaN-GaN-AlGaN electron blocking layer," Journal of Applied Physics **111**, 094503 (2012).

101. S.-H. Yen, M.-C. Tsai, M.-L. Tsai, Shen Yu-Jiun, T.-C. Hsu, and Y.-K. Kuo, "Effect of N-Type AlGaN Layer on Carrier Transportation and Efficiency Droop of Blue InGaN Light-Emitting Diodes," Photonics Technology Letters, IEEE **21**, 975 (2009).

102. H. Zhao, R. A. Arif, Y.-K. Ee, and N. Tansu, "Self-Consistent Analysis of Strain-Compensated InGaN-AlGaN Quantum Wells for Lasers and Light-Emitting Diodes," Quantum Electronics, IEEE Journal of **45**, 66 (2009).

103. M. Meneghini, N. Trivellin, G. Meneghesso, E. Zanoni, U. Zehnder, and B. Hahn, "A combined electro-optical method for the determination of the recombination parameters in InGaN-based light-emitting diodes," Journal of Applied Physics **106**, 114508 (2009).

104. Z.-H. Zhang, S. T. Tan, Z. Ju, W. Liu, Y. Ji, Z. Kyaw, Y. Dikme, X. W. Sun, and H. V. Demir, "On the Effect of Step-Doped Quantum Barriers in InGaN/GaN Light Emitting Diodes," Journal of Display Technology **9**, 226 (2013).

105. H. Zhao, G. Liu, J. Zhang, J. D. Poplawsky, V. Dierolf, and N. Tansu, "Approaches for high internal quantum efficiency green InGaN light-emitting diodes with large overlap quantum wells," Optics Express **19**, A991-A1007 (2011).

106. S. F. Chichibu, H. Yamaguchi, L. Zhao, M. Kubota, K. Okamoto, and H. Ohta, "Optical properties of nearly stacking-fault-free m-plane GaN homoepitaxial films grown by metal organic vapor phase epitaxy on low defect density freestanding GaN substrates," Applied Physics Letters **92**, 091912 (2008).

107. B. Liu, R. Zhang, Z. L. Xie, C. X. Liu, J. Y. Kong, J. Yao, Q. J. Liu, Z. Zhang, D. Y. Fu, X. Q. Xiu, H. Lu, P. Chen, P. Han, S. L. Gu, Y. Shi, Y. D. Zheng, J. Zhou, and S. M. Zhou, "Nonpolar m-plane thin film GaN and InGaN/GaN light-

emitting diodes on LiAlO[sub 2](100) substrates," Applied Physics Letters **91**, 253506 (2007).

108. Y. Zhao, Q. Yan, C.-Y. Huang, S.-C. Huang, P. S. Hsu, S. Tanaka, C.-C. Pan, Y. Kawaguchi, K. Fujito, C. G. Van de Walle, J. S. Speck, S. P. DenBaars, S. Nakamura, and D. Feezell, "Indium incorporation and emission properties of nonpolar and semipolar InGaN quantum wells," Applied Physics Letters **100**, 201108 (2012).

109. H. Masui, S. Nakamura, S. P. DenBaars, and U. K. Mishra, "Nonpolar and Semipolar III-Nitride Light-Emitting Diodes: Achievements and Challenges," Electron Devices, IEEE Transactions on **57**, 88 (2010).

110. D. S. Kim, S. Lee, D. Y. Kim, S. K. Sharma, S.-M. Hwang, and Y. G. Seo, "Highly stable blue-emission in semipolar (11-22) InGaN/GaN multi-quantum well light-emitting diode," Applied Physics Letters **103**, 021111 (2013).

111. E. Sari, S. Nizamoglu, T. Ozel, and H. V. Demir, "Blue quantum electroabsorption modulators based on reversed quantum confined Stark effect with blueshift," Applied Physics Letters **90**, 011101 (2007).

112. E. Sari, T. Ozel, A. Koc, J.-W. Ju, H.-K. Ahn, I.-H. Lee, J.-H. Baek, and H. V. Demir, "Comparative study of electroabsorption in InGaN/GaN quantum zigzag heterostructures with polarization-induced electric fields," Applied Physics Letters **92**, 201105 (2008).

113. T. Takeuchi, C. Wetzel, S. Yamaguchi, H. Sakai, H. Amano, I. Akasaki, Y. Kaneko, S. Nakagawa, Y. Yamaoka, and N. Yamada, "Determination of piezoelectric fields in strained GaInN quantum wells using the quantum-confined Stark effect," Applied Physics Letters **73**, 1691 (1998).

114. C.-F. Huang, C.-Y. Chen, C.-F. Lu, and C. C. Yang, "Reduced injection current induced blueshift in an InGaN/GaN quantum-well light-emitting diode of prestrained growth," Applied Physics Letters **91**, 051121 (2007).

115. Y. D. Jho, J. S. Yahng, E. Oh, and D. S. Kim, "Field-dependent carrier decay dynamics in strained $In_xGa_{1-x}N$/GaN quantum wells," Physical Review B **66**, 035334 (2002).

116. E. Sari, S. Nizamoglu, I.-H. Lee, J.-H. Baek, and H. V. Demir, "Electric field dependent radiative decay kinetics of polar InGaN/GaN quantum heterostructures at low fields," Applied Physics Letters **94**, 211107 (2009).

117. P. d. Mierry, N. Kriouche, M. Nemoz, S. Chenot, and G. Nataf, "Semipolar GaN films on patterned r-plane sapphire obtained by wet chemical etching," Applied Physics Letters **96**, 231918 (2010).

118. N. Okada, A. Kurisu, K. Murakami, and K. Tadatomo, "Growth of Semipolar (11-22) GaN Layer by Controlling Anisotropic Growth Rates in r-Plane Patterned Sapphire Substrate," Appl. Phys. Express **2**, 091001 (2009).

119. A. E. Romanov, T. J. Baker, S. Nakamura, J. S. Speck, and E. J. U. Group, "Strain-induced polarization in wurtzite III-nitride semipolar layers," Journal of Applied Physics **100**, 023522 (2006).

120. M. Funato, and Y. Kawakami, "Excitonic properties of polar, semipolar, and nonpolar InGaN/GaN strained quantum wells with potential fluctuations," Journal of Applied Physics **103**, 093501 (2008).

121. M. R. Krames, O. B. Shchekin, R. Mueller-Mach, G. O. Mueller, Z. Ling, G. Harbers, and M. G. Craford, "Status and Future of High-Power Light-Emitting Diodes for Solid-State Lighting," Journal of Display Technology **3**, 160-175 (2007).

122. O. Chen, J. Zhao, V. P. Chauhan, J. Cui, C. Wong, D. K. Harris, H. Wei, H.-S. Han, D. Fukumura, R. K. Jain, and M. G. Bawendi, "Compact high-quality CdSe–CdS core–shell nanocrystals with narrow emission linewidths and suppressed blinking," Nat Mater **12**, 445-451 (2013).

123. E. Jang, S. Jun, H. Jang, J. Lim, B. Kim, and Y. Kim, "White-Light-Emitting Diodes with Quantum Dot Color Converters for Display Backlights," Adv. Mater. **22**, 3076-3080 (2010).

124. S. Nizamoglu, G. Zengin, and H. V. Demir, "Color-converting combinations of nanocrystal emitters for warm-white light generation with high color rendering index," Applied Physics Letters **92**, 031102 (2008).

125. C. Dang, J. Lee, Y. Zhang, J. Han, C. Breen, J. S. Steckel, S. Coe-Sullivan, and A. Nurmikko, "A Wafer-Level Integrated White-Light-Emitting Diode Incorporating Colloidal Quantum Dots as a Nanocomposite Luminescent Material," Advanced Materials **24**, 5915-5918 (2012).

126. C.-Y. Huang, S. Yan-Kuin, Y.-C. Chen, T. Ping-Chieh, W. Cheng-Tien, and W.-L. Li, "Hybrid CdSe-ZnS Quantum Dot-InGaN-GaN Quantum Well Red Light-Emitting Diodes," Electron Device Letters, IEEE **29**, 711-713 (2008).

127. W. K. Bae, J. Kwak, J. Lim, D. Lee, M. K. Nam, K. Char, C. Lee, and S. Lee, "Multicolored Light-Emitting Diodes Based on All-Quantum-Dot Multilayer Films Using Layer-by-Layer Assembly Method," Nano Letters **10**, 2368-2373 (2010).

128. C.-F. Chu, C.-C. Cheng, W.-H. Liu, J.-Y. Chu, F.-H. Fan, H.-C. Cheng, T. Doan, and C. A. Tran, "High Brightness GaN Vertical Light-Emitting Diodes on Metal Alloy for General Lighting Application," Proceedings of the IEEE **98**, 1197-1207 (2010).